Universita' degli Studi di Napoli Federico II
Scuola di Dottorato in Ingegneria Industriale
Dottorato di Ricerca in Ingegneria Chimica - XXVII ciclo

Microparticle manipulation in viscoelastic liquids: towards a modular microfluidics

Tesi di Dottorato di
Francesco Del Giudice

Comitato Scientifico

Prof. Pier Luca Maffettone
Universita' degli Studi di Napoli Federico II

Dr. Francesco Greco
Istituto di Ricerche sulla Combustione - CNR

Prof. Paolo Antonio Netti
Universita' degli Studi di Napoli Federico II

Dr. Ing. Gaetano D'Avino
Universita' degli Studi di Napoli Federico II

Ai miei genitori, sempre presenti e sempre grandi educatori lungo il mio percorso di lavoro e di vita...

Aknowledgements

Desidero ringraziare tutti coloro che mi hanno accompagnato durante questo percorso di vita e di studio.
In primis voglio ringraziare il caro Pier Luca. Hai creduto in me fin dall'inizio. Non sono stato io a cercare te ma sei stato tu a cercare me e mai mi sarei aspettato di vivere tre anni migliori sotto il profilo umano e della ricerca.
Ringrazio il caro Francesco Greco perché hai la grande abilitá nel trasformare ogni nostro incontro in un momento molto formativo. Guardando oltre l'apparente 'eccessiva' pignoleria, ho imparato tanto dai nostri incontri.
Ringrazio il carissimo Gaetano D'Avino. Hai saputo essere tanto paziente durante la fase iniziale del mio percorso e sempre presente nelle ore di lavoro (salvo alcuni casi dovuti a mancanza di sonno). Ti ringrazio, inoltre, per avermi reso sempre partecipe nei tuoi vari momenti importanti di questi ultimi tre anni.
Ringrazio il prof. Paolo Netti per avermi dato la possibilitá di fare ricerca all'interno di un polo di eccellenza che ha contribuito molto alla mia crescita scientifica.
Ringrazio voi cari miei amici e colleghi Gaetano, Massimiliano, Marco Trofa, Marco De Corato, Carmelina con cui ho condiviso tanti momenti (forse ne avremmo potuti condividere di piú ma questa é colpa mia), tante risa e tanti viaggi formativi e non, che mi hanno donato momenti di vita vissuta unici.
Ringrazio tutti voi, amici miei e colleghi dell'IIT; scrivere tutti i vostri nomi mi porterebbe a riempire piú fogli della tesi e inoltre non vorrei dimenticare nessuno di voi. Grazie perché abbiamo passato insieme intere giornate condividendoci le gioie e le ansie dei nostri progetti di Dottorato e non solo. A tutti coloro che mi hanno chiesto una mano per qualunque cosa, concernente il lavoro e non, spero di avervi saputo dare qualcosa di utile. Sappiate, inoltre, che questi momento sono stati formativi prima di tutto per me ed é per questo che vi ringrazio. Grazie, inoltre, per tutte le esperienze extralavorative vissute insieme, ognuna di esse mi ha fatto dono di una relazione

particolare con ciascuno di voi. Con il vostro aiuto spero di continuare a coltivare tali relazioni nel corso degli anni a venire.
Ringrazio Milena, Ida e Valeria perché siete riuscite sempre a sopportarmi durante il vostro periodo di tesi in cui ho avuto il piacere di potervi seguire. Al di lá di tutto, avete saputo farmi dono del vostro tempo e delle vostre energie e spero che in cambio abbiate ricevuto qualcosa di gratificante e stimolante per la vostra vita lavorativa e non.
Ringrazio i miei amici di sempre Mariana, Gennaro, Alessia, Stefano, Marianna. Rappresentiamo una piccola famiglia di persone unite da lunga data e da un sentimento piú profondo e forte dell'amicizia stessa. Vi ringrazio per aver condiviso con me le emozioni piú intime e forti di questo mio percorso di lavoro e di vita.
Ringrazio i miei genitori, ai quali dedico la mia tesi di dottorato. Avere avuto accesso al titolo piú alto che l'universitá puó conferire é merito vostro che mi avete sempre spinto e incoraggiato nello scegliere ció che a me piaceva.
Ringrazio te, Grazia, colei che é subentrata piú o meno a metá del mio percorso di studi. Con l'amore e l'affetto di ogni gesto hai saputo contribuire a farmi vivere con un approccio diverso le mie giornate, perché sei parte viva e sempre presente nei miei pensieri e nel mio cuore.
Ringrazio te, Giovanni, che mi hai accompagnato durante il mio primo anno di ricerca; mi hai insegnato il valore della ricerca e del cercare di fare al meglio gli esperimenti. Ora che sei al cospetto di Dio ti chiedo di continuare ad essere presente nella mia vita perché ho e avró sempre da imparare.
Infine voglio ringraziare nuovamente il Signore. Nei ringraziamenti della mia tesi di laurea ho scritto che nulla succede per caso ed in questi tre anni ho avuto modo di rendermene conto sempre di piú.
Ho iniziato con un salto nel buio, in qualcosa che non conoscevo, e Tu ti sei manifestato in tante persone e in tanti avvenimenti che mi hanno fatto comprendere come la felicitá si raggiunga quando la mia volontá incontra la Tua.
Questa per me é stata e continua ad essere la mia piú grande scoperta...

Contents

Abstract

Microfluidics have received great attention in the last decades due to its wide applicability in molecular analysis, biodefense, molecular biology and microelectronics. In the molecular analysis field, in particular, several applications such as particles/cells counting and separation are explored. For these applications, particles or cells are commonly suspended in Newtonian liquids. More recently, an increasing interest in using viscoelastic fluids in microfluidic devices is observed. Indeed, it has been recently proven that the non-Newtonian rheological properties of the fluid allow to perform several of the above mentioned operations by using simpler apparati as compared to the case with a Newtonian liquid. In most applications, microchannels with a square cross-section are used, due to the ease of fabrication.

In this thesis, we study the effect of fluid rheology on the suspended particle motion, in square-shaped microchannels. To this aim, several fluids are considered. Elastic, constant-viscosity fluids promote particle migration towards the channel centreline, achieving the so-called *3D focusing*. For shear-thinning fluid, in contrast, the migration phenomenon is more complex: at low flow rates, i.e. in the constant viscosity region, particles still migrate towards the channel centreline, while at high flow rates, i.e. in the shear-thinning region, the migration reverts direction, and the particles are driven towards the corners of the channel cross-section. In addition, our results highlight the weak effect of inertia on particle migration as compared to viscoelastic effects, even for low elasticity suspending liquids.

In the second part of this thesis, we exploit the viscoelasticity-induced particle migration to design a *microrheometer* capable of estimating the relaxation time of viscoelastic fluids, down to milliseconds. A remarkable improvement in the accuracy of the measure of the relaxation time is found, when comparing our results with experimental data obtained from shear or elongational

experiments available in literature. Good agreement of our results with available theoretical predictions is also found.

Finally, we design and fabricate a microfluidic device for deflection of magnetic particles from a contaminated streamflow into a clean one. This device is made of two modules: a first one (a straight channel), where magnetic particles are 3D focused on the channel centreline; a second one (a H-shaped channel), where a permanent magnet is used to displace the magnetic beads from the original to the buffer stream. When viscoelastic focusing and magnetophoresis are combined, by applying the two moduli in series, a deflection efficiency of $\sim 96\%$ can be achieved.

Introduction

The December 29^{th} 1959 was an important day for some scientists. While many people were coming out from Christmas holidays and were projected to the upcoming new year (so they were preparing meals and fireworks), at the California Institute of Technology a man was giving a speech while walking on the stage of the American Physical Society. He was a physicist, and probably many of the scientists in that room for the meeting would have wanted to think to something different from physics. Nevertheless, the speaker was actually really good, and the title of his speech caught the audience attention; in fact, still today, it sounds very strange. The heading, indeed, was *There is plenty of room at the bottom* [1], referring to the world at the *nano*-scales. The orator was talking about something completely avulsed from the world around him, which was focusing on *macro*-technologies instead. But the speaker was a physicist, physicists were looking for atoms(!), and in particular he was Richard Feynman (Nobel prize in 1965), and all the scientific community knew how good was that speaker. Richard Feynman was talking about something completely new at the time, something that was not related to the 'fundamental physics' of elementary particles, gravitation, etc. but to the strange phenomena that occur in complex situations at the nano-scales. Several technologies, in fact, have been required to explore the nano-scales and their development took approximately twenty years from Feynman speech. The first obtained devices, however, can be classified just as a 'proof of concept', because they were not useful for practical applications, but just to prove that it is really feasible to produce these technologies.

One very important example of a practical *micro*-device involving mechanical and electrical parts, the so-called Micro Electro Mechanical Systems (MEMS), was a chip for the airbag activation in the cars [2]. In particular, a few millimetres long chip had the mechanical system for the impact detection, and the electrical part to give the signal to the airbag. From that

moment on, several other technologies were developed, and more and more devices produced.

When microfabrication was almost standardised, the scientific community started to think to new applications, in particular for the healthcare. Some of those applications required fluid pumping through the device. At this purpose, the design of a *micro-pump* was necessary. One example is offered by the Debiotech company [2], that patented and produced the first micropump for diabetics people. This device could be applied directly on the body and released a fixed amount of insulin directed in the patient without passing through the conventional syringes.

During the 90's many research groups started to work in the microfluidic field [3, 4, 5], in particular in many applications such as cell stretching and flow cytometry. Flow cytometry is a biophysical method, involving laser, used for cell or particle counting: this method allows to count particles flowing in a microchannel ($\sim 10^{-4}$ meters wide). In particle counting, laser beam intercepts a particle flowing in the microchannel: as the laser beam size is quite smaller than the channel dimensions, it is required that most of the flowing particles follow the same path-line, where the beam is pointed. If particles in the the channel are randomly distributed, particle counting is not possible. In other words, particles should be *focused* at a certain position in order to match the laser beam. Positioning particles at a specific channel position (often, this is the centreline of the channel) is called *particle focusing*. Another important microfluidic application is particles separation [6]. Common separation processes include filtration and centrifugation and, most prominently, forms of chromatography and electrophoresis. All these procedures are done in a batch way. Microfluidic would then be an improvement, in terms of continuous operations.

All these operations are performed in single microfluidic devices. A *novel* challenge today is to design several microfluidic devices, each one performing a 'unit operation'. Several devices working together can be used in complex situations, thus replying what happens in chemical plants. In this way, each

microdevice in the 'plant' acts as a single *module* leading to what is called *modular microfluidics*. Two microfluidic modules are analysed in this thesis: the focusing and the deflection modulus. In the first one, it is possible to achieve a 3D particle focusing; in the deflection modulus, instead, particles are deflected from a streamflow to another one.

In microfluidic systems Newtonian fluids (e.g. water) are commonly used. To promote particle migration in Newtonain liquids, complex geometry, external fields or inertial effects are needed [7, 8, 9] . However, the use of non-Newtonian fluids has recently received great interest, due to the possibility to generate forces 'from the inside' of the flowing fluid [10]. There are experimental and numerical evidences of the strict relation between these forces and particle migration in cylindrical and rectangular geometries [10, 11, 12, 13]. Therefore, non-Newtonian liquids can be used as suspending fluids for many applications. From the analysis of the state of art regarding the use of viscoelastic fluids in microfluidic applications, it is however apparent that a comprehensive explanation of the effect of fluid rheology on particle migration is still missing. It is important to highlight that the correct knowledge of the migration phenomena is very important to design microfluidic devices. Motivated by these observations, in this thesis, we study the effect of the suspending viscoelastic fluid on the motion of suspended particles. In Chapter 1 we report the state of art on particle migration in microchannel first, and on the focusing and separation techniques later. In Chapter 2 we present a novel method to extract the exact particle positions in the square cross-section by combining experiments and numerical simulations. In the same chapter, we also present a novel method to measure the relative viscosity by using Optical Tweezers (OT), without passing through the Fourier transform. In Chapter 3 we report the rheological characterisation of the fluids used in this thesis. In particular we focus on a constant-viscosity fluid (Poly Vynil Pyrrolidone water solution), on several shear-thinning fluids (Poly Ehylene Oxide at several mass concentrations) and on HydroxyEthyl Cellulose solutions. In Chapter 4, we use the results of Chapter 3 to qualitatively and

quantitatively analyse particle migration phenomena in viscoelastic liquids. In Chapter 5 we present a novel method to measure fluid relaxation times down to milliseconds based on particle migration in viscoelastic liquids, and a device to deflect magnetic particles from a contaminated streamflow to a buffer one. The last device was designed as the combination of two separate apparati working in series, each one performing a unit operation. This device is therefore an example of a modular microfluidic system. Finally, conclusions are presented and possible future works are discussed.

Chapter 1

State of Art

In this section we will briefly report the state of art on the manipulation of micro-sized particles in microfluidic devices. First of all, we proceed to explain the particle migration phenomenon, i.e. the particle motion transversally to the flow direction, in Newtonian (constant viscosity and no elasticity) and non-Newtonian liquids. This background, in fact, represents the baseline fluid dynamic knowledge for what follows in the work. In addition particle migration is fundamental to understand some microfluidic designs for several applications such as particle focusing (see Section 1.2) and particle separation (see Section 1.3).

1.1 Particle migration in Poiseuille flow

Let us consider a single particle, with a certain diameter D_p, suspended in a Newtonian liquid subjected to the flow, for example, in a square-shaped channel with side $H >> D_p$, and faraway from the walls. In this case, the particle flows undisturbed [14], with no transversal motions, because it does not *feel* the walls. If, in contrast, the channel side is $H \sim 10D_p$ (say), some non-linear phenomena can occur in dependence on the flow conditions. In this section we will focus on situations where the confinement ratio (see Section 2.9 for more details) $\beta = D_p/H \sim 0.1$; it is properly the situation

where such non-linear phenomena can occur.

1.1.1 Particle migration in Newtonian liquids

Inertialess flow conditions

For a particle suspended in a Newtonian fluid (constant viscosity and no elasticity) flowing in a microchannel, the well know Navier-Stokes equations apply [15]:

$$\nabla \cdot \boldsymbol{v} = 0 \tag{1.1}$$

$$\rho \frac{\partial \boldsymbol{v}}{\partial t} + \rho \boldsymbol{v} \cdot \nabla \boldsymbol{v} = -\nabla \wp + \eta \triangle \boldsymbol{v} \tag{1.2}$$

where ρ is the fluid density, $\boldsymbol{v}$ is the fluid velocity, $\wp = p + \rho \boldsymbol{g}$, where p is the pressure and $\boldsymbol{g}$ is the constant gravitational acceleration, and η is the fluid viscosity. These equations are non-linear because of the presence of the term $\boldsymbol{v} \cdot \nabla \boldsymbol{v}$, negligible when inertial forces are negligible. In this case, NS equations assume the form:

$$-\nabla \wp + \eta \triangle \boldsymbol{v} = \boldsymbol{0} \tag{1.3}$$

these equations (namely Stokes equations) together with linear boundary conditions, are linear, and the *time-reversal theorem* [7] is valid. Such theorem, when applied to the case of a spherical particle suspended in a matrix subjected to a Poiseuille flow (i.e. the flow in pipes with a parabolic velocity profile), establishes that a particle suspended in the Newtonian fluid, starting from a certain position (flow line) within the channel, cannot migrate transversely to the flow direction. This result hold, of course, for a non-Brownian and non-buoyancy particle in the dilute regime (where particle-particle interactions are negligible) and for Newtonian fluids in inertialess conditions. It is possible to better understand the theorem in the conditions of interest here by using a *reductio ad absurdum* arguments as schematised in Figure 1.1.

Let us assume that the particle can migrate. When imposing a flow in the positive x-direction, a particle in position 1 can migrate, e.g., towards the position 2, i.e. in the positive y-direction (see Figure 1.1a) . When,

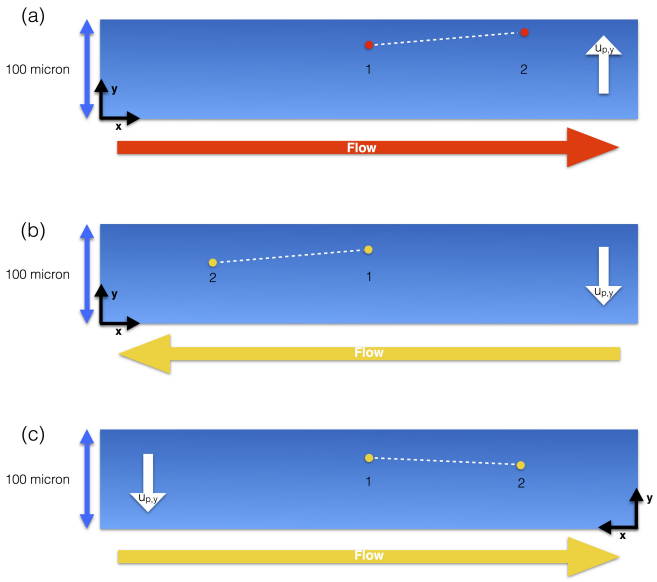

Figure 1.1: *Reductio ad absurdum* of the time-reversal theorem. (a) A particle migrate from position 1 to position 2 when imposing a flow in the positive x-direction. (b) Assuming the validity of the time-reversal theorem, when imposing the flow in the negative x-direction, the particle starting from position 1 should migrate to position 2. (c) Is the same situation as in (b) for an observer situated on the opposite side of the channel, i.e. is the 'mirror'of (b). Situation in (c) is the same of (a) but with a different arriving position 2. It is in contrast with the time-reversal theorem.

in contrast, imposing the flow in the negative x-direction, because of the time-reversal theorem, the particle must migrate in negative y-direction (see Figure 1.1b). For an observer situated on the opposite side of the channel, however, the situation showed in Figure 1.1b is actually that of Figure 1.1c. The scheme in Figure 1.1c, however, is the same as in Figure 1.1a with a different final point 2. This would imply that a particle starting from a certain position could attain different final positions 2, which is in contrast with the (assumed) uniqueness of solution of the NS equations. Basing on the simple argumentations here presented, we can then state that a particle

suspended in a matrix subjected to Poiseuille flow in inertialess conditions cannot migrate transversally to the flow direction.

Inertial flow conditions

In the previous section we have seen how particles suspended in a matrix subjected to Poiseuille flow cannot migrate in inertialess conditions, due to linearity of the Navier-Stokes equations. For the full Navier-Stokes equations (with a non-linear term also) the time-reversal theorem does not apply, and therefore particles could experience some force that push them transversally to the flow direction. Several theoretical and experimental works [8, 16, 17] studied particle migration in inertial flow conditions. In particular, Segré and Silberberg [16] found that particles suspended in a liquid subjected to Poiseuille flow when inertia is not negligible migrate towards several 'equilibrium' positions situated at $R_{ss} = 0.6R$ from the channel centreline, where R_{ss} is the so-called Segré-Silberberg radius and R is the channel radius. Therefore, all particles will eventually lie on a circle located at R_{ss}. These equilibrium positions are the result of a force balance between the *wall-lift* force F_w that pushes particles away from the wall and the *shear-gradient* force F_s that pushes particles towards the wall. Ho and Leal [8] theoretically studied the motion of a particle suspended in a Newtonian matrix subjected to Poiseuille flow when inertia is not negligible, in a planar geometry. They found the same results of Segré and Silberberg, but with $H_{ss} = 0.6H/2$ where H is the channel height.

In Summary, particles in inertial flow conditions experience migration forces that push them towards an equilibrium positions situated at $0.6R$ from the centreline for the cylindrical channel and at $0.6H/2$ for the rectangular geometry.

1.1.2 Particle migration in non-Newtonian liquids

We have previously seen that inertial effects promote particle migration orthogonal to the flow direction to a single surface. Particle migration is also

possible by introducing a non linearity in the NS equations, due to the 'complexity' of the fluid [10, 11, 13]. Such fluid should show some complex rheological properties when subjected to flow. In particular, non-Newtonian fluids in flow are able to store a certain amount of elastic energy. For that reason, they are also called viscoelastic liquids. We anticipated that when $Re \sim 0$ we neglect the non linear term in NS equation; however, we must include now a new nonlinear term, given by the fluid complexity. The NS equations, in fact, come from the more general Cauchy equations [15]:

$$\rho \frac{\partial \boldsymbol{v}}{\partial t} + \rho \boldsymbol{v} \cdot \nabla \boldsymbol{v} = \rho \boldsymbol{g} + \nabla \cdot \boldsymbol{T} \tag{1.4}$$

where $\boldsymbol{T}$ is the stress tensor. NS equation are obtained introducing a constitutive equation. For the Newtonian liquid $\boldsymbol{T}$ is expressed by:

$$\boldsymbol{T} = -p\boldsymbol{I} + \frac{1}{2}\eta(\nabla \boldsymbol{v} + \nabla \boldsymbol{v}^T) \tag{1.5}$$

Replacing this expression in Eq. (1.4), NS Equations are again obtained. In contrast, when the fluid is non-Newtonian, the stress tensor $\boldsymbol{T}$ is written as:

$$\boldsymbol{T} = -p\boldsymbol{I} + \frac{1}{2}\eta(\nabla \boldsymbol{v} + \nabla \boldsymbol{v}^T) + \boldsymbol{\tau} \tag{1.6}$$

The last term $\boldsymbol{\tau}$ can be modeled in several ways. Just to make an example, we report here the Giesekus model, where $\boldsymbol{\tau}$ is given by the following equation [18]:

$$\lambda \overset{\triangledown}{\boldsymbol{\tau}} + \frac{\alpha\lambda}{\eta}\boldsymbol{\tau} \cdot \boldsymbol{\tau} + \boldsymbol{\tau} = \eta_p(\nabla \boldsymbol{v} + \nabla \boldsymbol{v}^T) \tag{1.7}$$

where the symbol $^{\triangledown}$ on $\boldsymbol{\tau}$ is the upper convected Maxwell derivative [19], η_p is another viscosity, λ is the fluid characteristic time, and α is a 'shear-thinning' parameter. This equation is strongly non linear. It means that again, in principle, particles can move transversally to the flow direction, because the time-reversal theorem does not apply. Ho and Leal [9] theoretically studied the motion of a particle suspended in a viscoelastic fluid in a two-dimensional flow. They found that the particles experience a force that push them towards the channel centreline, regardless of their initial positions.

Therefore, particles suspended in a viscoelastic fluid, even in inertialess conditions, experience a net 'internal' force that pushes them towards the channel centreline. This force, obviously, strongly depends on the fluid properties [12, 20]. In conclusion, particles suspended in a non-Newtonian fluid and subjected to a Poiseuille flow can migrate transversally to the flow direction even in inertialess flow conditions, due to the complex flow properties of the suspending medium .

1.2 Particle focusing in microfluidic devices

Particle focusing is achieved when all the particles lie, i.e. are *focused*, on certain fixed positions within the channel. In particular, two different kinds of particle focusing exist: when the particles' equilibrium positions lie on a specific channel surface, we say that *2D particle focusing* is achieved [21]; when, in contrast, all the particles lie on a single-line, we say that *3D particle focusing* is achieved [11]. In order to focus 2D or 3D particles, several technologies can be used. In particular, we have seen that particles suspended in a Newtonian matrix in inertialess flow conditions cannot migrate transversally to the flow direction. Therefore, in order to focus particle suspended in Newtonian media several complex designs involving, for example, sheath flows are needed (passive focusing). For some 'special' particles, like electric or magnetic ones, several external fields can be used to push particles towards several equilibrium positions within the channel (active focusing). In contrast, particles suspended in a non-Newtonian matrix explore an internal force that push them towards several 'equilibrium' positions, thus simplifying the channel design and the experimental apparatus at the same time. In this section, we will report some methods to achieve particle focusing, involving different designs.

1.2.1 Sheath flow focusing

As explained in the previous section, particles suspended in Newtonian liquids and subjected to Poiseuille flow cannot migrate transversally to the flow direction in inertialess conditions [7]. Hence, in order to achieve particle focusing in Newtonian liquids and inertialess conditions, it is necessary to properly design the microlfuidic device. One of this *chip*-design involves sheath flows, as reported in Figure 1.2a. Lee *et al.* [22], in particular, designed a microfluidic device with two sheath flows as reported in Figure 1.2a. The streamflow containing particles suspended in a Newtonian matrix is injected with an imposed flowrate Q_i. At the channel inlet, of course, particles are randomly distributed within the cross-section. Therefore, two side channels carrying in the unloaded fluid with a flow rate Q_s, are used, in order to focus particles on a single stream-plane. In fact, particles from the inlet can move in the y-direction only due to the sheath flows. They cannot migrate towards the z-direction, i.e. along the channel depth H, because of the fluid dynamic conditions [7]. By changing the ratio Q_s/Q_i, it is possible to obtain a stream-plane with different 'thicknesses', up to achieving a 2D particle focusing.

In order to achieve a 3D particle focusing, in another work Lee *et al.* [23] proposed a different more complex design, which is reported in Figure 1.2b. In this device there are two inlets: in the first one a red blood cell solution is injected, while in the second one a dye solution is fed. The device is designed with a contraction-expansion array; when both the solution and the dye pass through this region, they experience the so-called Dean vortices [21] generated by the centrifugal force, that pushes the particles towards the centreline. As a matter of fact, this channel is designed with one sheath flow that first pushes the red blood cell solution towards the wall on a plane (2D focusing), and then with a contraction-expansion array (generating Dean vortices), that pushes these cells towards the channel centreline. The devices presented here, are designed for cell/particle focusing. Both of them, however, even if they actually do 2D or 3D focusing, are very difficult to fabricate and to control,

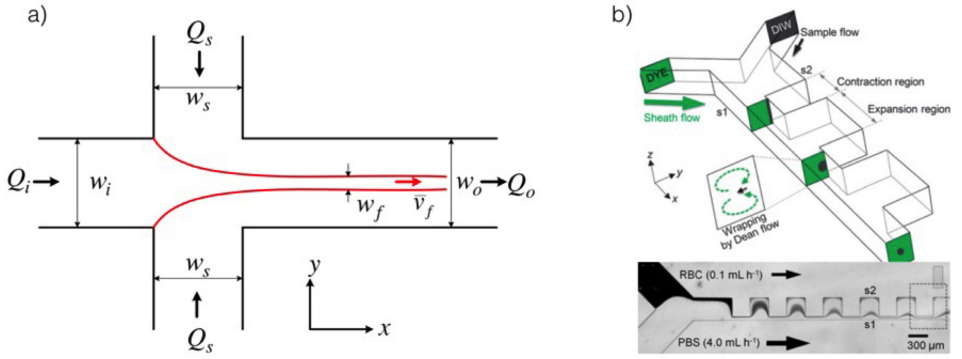

Figure 1.2: (a) Schematic illustration of symmetric hydrodynamic 2D flow focusing. Reprinted with permission from Lee *et al.* [22]. (b) Schematic of the contraction-expansion array microchannel for 3D hydrodynamic focusing; downside figure is the image of red blood cells focused by a phosphate buffered saline flow. Reprinted with permission from Lee *et al.* [23]

because of the multiple inlet design.

1.2.2 Dielectrophoresis-based focusing

To reduce the complexity of the channel design, it is possible to achieve particle focusing by involving an external field that act on the particles, thus pushing them towards some position within the channel [24]. As a first example, we report here a focusing device based on the dielectrophoresis (DEP). DEP is the migration of particles transversally to the flow direction, due to the behaviour of an electrical dipole in an electric field. Indeed, if there exists a field gradient normal to the applied flow, particles at different initial positions can be deflected on different streamlines. Chu *et al.* [25], for example, designed a microfluidic device (see Figure 1.3a) in which a dielectric structure, together with an electric field, promotes 3D particle focusing on a channel centreline. In fact, particles coming inside the channel inlet randomly distributed are deflected by an external electric field (normal to the

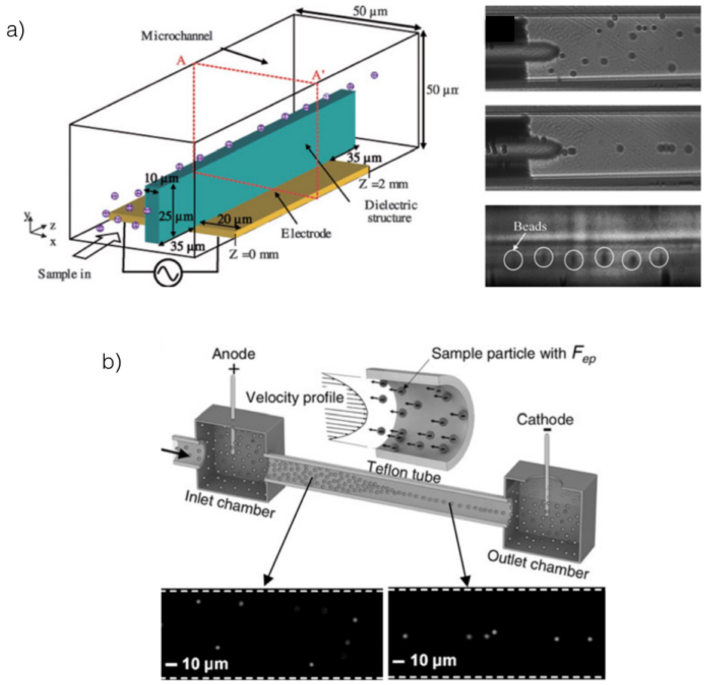

Figure 1.3: (a) Schematic view of the 3D particle focusing channel using positive DiElectroPhoresis (DEP) guided by a dielectric structure between two planar electrodes. Side figures are the images of 2 μm polystyrene beads near the end of the focusing channel when AC voltage is off (top and on (middle for top view, bottom for the side view). Reprinted with permission from Chu *et al.* [25]. (b) Schematisation of the axisymmetric focusing of particles in a single circular microcapillary. Reprinted with permission from Chu *et al.* [25] and Kim and Yoo [26].

flow direction) towards the channel centreline. Figure 1.3a reports also the experimental images when the electric field is OFF (top), where particles are randomly distributed within the cross section, and when the electric field is ON, from the top view (middle image) and side view (bottom image).

Another very clever way to achieve 3D particle focusing by using electric field was presented by Kim an Yoo [26], and is reported in Figure 1.3b. It is

well known that when particles are lagged in a Poiseuille flow, they migrate towards the channel axis due to a 'lift'force generated by the imbalance of the velocities [27, 28]. Kim and Yoo use this phenomenon to achieve 3D focusing; in particular, the lag force is generated by an electric field that lags the particles flowing in the microchannel (see Figure 1.3b). At the end, particles migrate towards the channel centreline achieving the 3D *axisymmetric* focusing. This method has the great advantage of a very simple geometry (a straight channel); on the other hand, an external electric field is necessary. Therefore, in all dielectrophoresis applications, the device complexity is replaced by the difficult in controlling an electric field.

1.2.3 Inertial focusing

As described in Section 1.1.1, in inertial fluid dynamic conditions, particles suspended in a flowing liquid can experience forces that push them towards some equilibrium positions [8, 16]. These equilibrium positions, in addition, are different for different channel geometries [21, 29]. Di Carlo [21] comprehensively studied the particle focusing in a square-shaped microchannel geometry and compared the results with that of Segré and Silberberg [16].

In Figure 1.4(a-b) the comparison between equilibrium position in cylindrical and square-shaped geometry is reported. The forces acting on the particles are reported in Figure 1.4(c-d). By assuming a random distribution at the channel inlet and, with relevant inertial effects, particles in a cylinder migrate towards a position situated at $0.6R$ from the centreline, where R is the channel radius. In cylindrical geometry, then, particles are 2D focused, because they lie on a cylindric surface within the channel and coaxial with it. In the square-shaped microchannel the focusing mechanism is the same, i.e. only wall lift and shear gradient force act on the particle, but the equilibrium positions are different (see Figure 1.4b). In fact, particles now occupy four symmetrical equilibrium positions, situated at $0.6H/2$ from the centreline and at the middle height of each channel face. Therefore, particles are not 2D focused, because they are not lying on a surface. In this case we can say

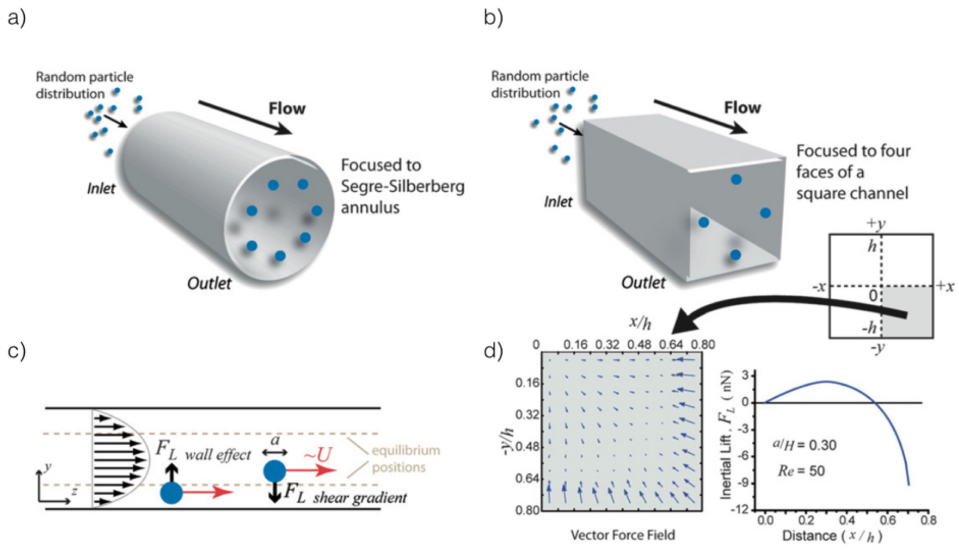

Figure 1.4: (a) Representation of inertial particle migration in cylindrical channel. (b) Representation of inertial particle migration in square shaped microchannel. (c) Force acting on a particle in inertial conditions. (d) Force field simulation on a particle over a quarter of channel cross section. Reprinted with permission from Di Carlo [21]

that particles are 3D focused on each channel face. Of course, this does not mean that particles are fully 3D focused, because they are divided among four single lines. Experimental results on focused particle positions, obtained by using holographic microscopy, are available in literature [30]. The presence of the four corners significantly alter the equilibrium positions with respect to the cylindrical geometry. Inertial focusing, in both these geometries, cannot be used, for example, for flow citometry or particle counting. In fact, cells or particles should lie on a single line (not on four lines) in order to be easily detectable by a laser spot. Several other works are available in literature on the combination of inertial migration and curved microchannel [31, 32]. In particular Gosset and Di Carlo [31], studied the effect of inertia and Dean vortices on particle focusing in a rectangular-shaped device with a curved mi-

crochannel. In the first part of the device, i.e. a simple rectangular straight channel, particles migrate towards only two equilibrium positions located on the long channel faces [29, 33]. These equilibrium positions are the initial positions for the second part of the device, i.e. a curved channel. Gosset and Di Carlo showed that particle focusing is affected by the combination of inertia and Dean flow, in particular particles migrate *inward* or *outward* depending on the initial positions. A more recent study of Martel and Toner [32], showed the decoupled effect of inertia and Dean flow in curved geometries with different radius of curvature. The main result was the existence of a set of conditions where a single equilibrium position is achieved for particles of different sizes. These results, however, are still difficult to explain (as remarked by the authors) due to the complexity of the fluid dynamic conditions in those devices.

1.2.4 Viscoelastic focusing

Even if particle migration in viscoelastic fluids was a well known phenomenon since the 1976 [9], only in 2007 the work of Leshansky *et al.* [10] reported the experimental evidence of particle focusing in viscoelastic liquids in a microfluidic channel. Leshansky *et al.* studied the focusing of particles suspended in a water solution of Poly Vynil Pirrolidone (PVP) at 8% w/w (viscoelastic fluid), in a rectangular slit-like channel. They showed that 2D particle focusing is achieved in this geometry, in the absence of inertial effects. In particular, particles are focused on the middle-plane of the channel. They also showed that the migration velocity is proportional to the gradient of the first normal stress difference ∇N_1. By using the same suspending fluid, D'Avino *et al.* [11] showed that all the particles migrate towards the channel centreline in a cylindrical microchannel, thus achieving for the first time a purely viscoelastic 3D focusing (see Figure 1.5b). They also reported a design criterion based on scaling arguments from which, known the channel geometries and the fluid properties, it is possible to derive the so-called *focusing length*, i.e. the distance from the inlet at which particles are 3D focused.

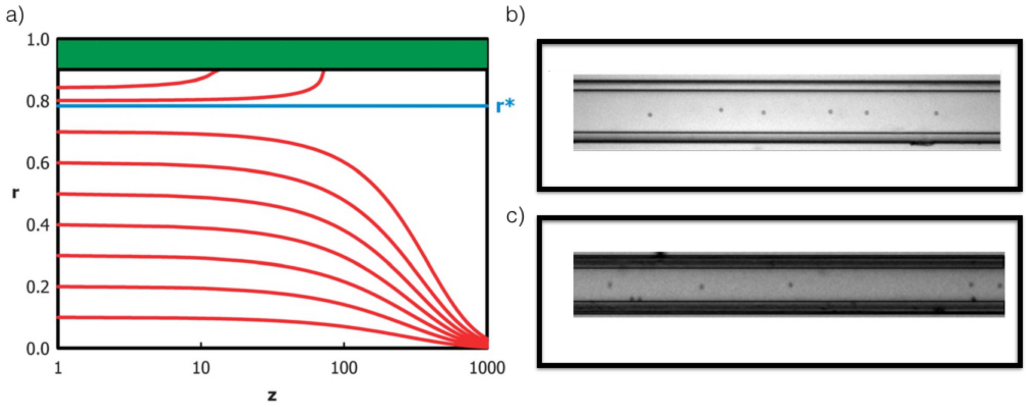

Figure 1.5: (a) Simulation of the particles trajectories starting from different initial positions. Particles which initial positions $r < r^*$ migrate towards the centrline. Particles which initial positions $r > r^*$ migrate towards the walls (b) Experimental image of 3D focused particles suspended in PVP 8%. (c) Experimental image of the bistability scenario in PEO 1% w/w. Some particles started at $r > r^*$ migrated towards the channel wall. Reprinted with permission from D'Avino *et al.* [11]

They further showed that a shear-thinning fluid, i.e. a fluid with a viscosity that is function of the shear rate $\dot{\gamma}$ (see Section 3.2 for more details), gives raise to a bistability scenario: in the constant viscosity region (low flowrate) particles migrate towards the centreline, while in the thinning region (high flow rate) particles migrate towards the wall (see Figure 1.5). More recently, Seo *et al.* [34] reported more experiments on the effect of the shear thinning on particle migration in cylindrical channel, by using the holographic microscopy. They found results substantially analogous to those by D'Avino *et al.* [11]. Very recently, Kang *et al.* [35] showed that even small ppm of λ-DNA, that is a semi-flexible polymer [36], can 3D focus particles of several dimensions around the channel centreline. In conclusion, viscoelastic 3D focusing was achieved in cylindrical geometry.
Nevertheless, square-shaped geometry are more common in microfluidics, because of their simpler fabrication. Yang *et al.* [13] studied the effect of fluid

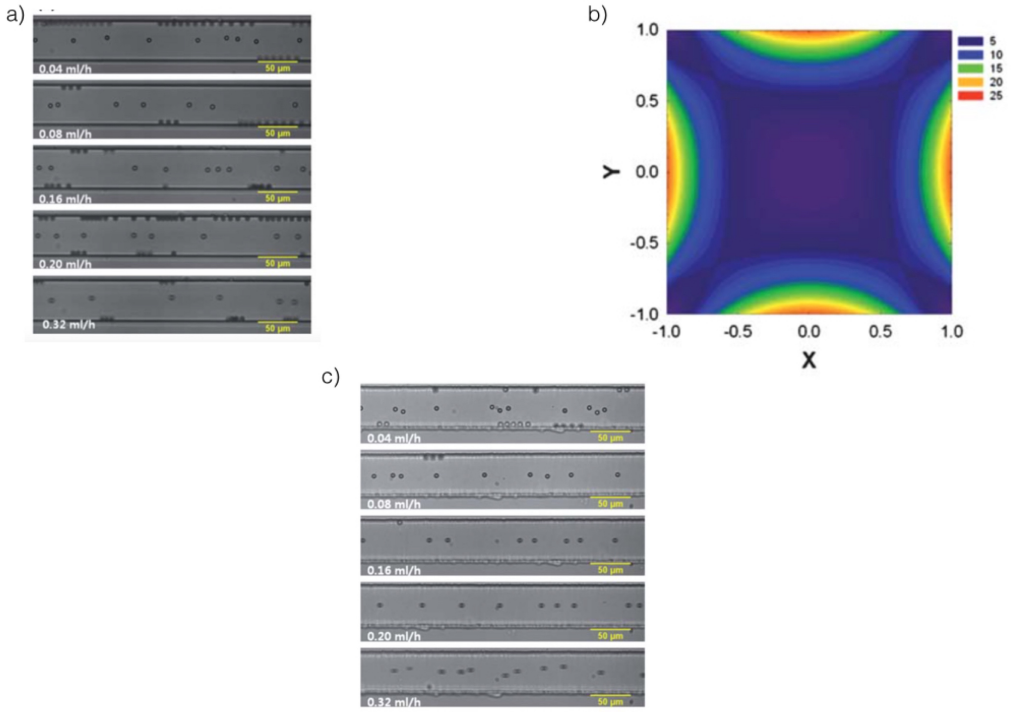

Figure 1.6: (a) Experimental snapshot of positions of particles suspended in PVP 8% , flowing in a square-shaped channel at different flow rates. (b) N_1 distribution in a square cross section of the channel: five minima are present at the center and at the four corners. (c) Experimental snapshot of particle positions in a square channel using PEO 0.05% wt at different flow rates. Reprinted with permission from Yang *et al.* [13]

properties on particle focusing in square-shaped microchannel. They found that by using a water solution of PVP 8% w/w, particles migrate towards five equilibrium positions, namely the centreline and the four corners, as reported in Figure 1.6(a-b), for every imposed flow rate Q. The explanation of this phenomenon is inside ∇N_1: the five equilibrium positions in the square channel correspond to the five minima of N_1 (figure 1.6b). The authors demonstrated that, by changing the fluid with a PEO 4MDa 0.05% wt (shear thinning fluid), particles can be aligned on the centreline combining

viscoelastic effects and inertial effects (Figure 1.6c). In fact, particles at the corners are pushed away because of inertial wall lift force and migrate towards the centreline because subjected to the elastic force. The main disadvantage of this kind of 3D focusing is in the rather narrow range of flow rate available for alignment: at low flow rates elastic effects are dominant; at high flows rate inertial effects dominate. This focusing mechanism then applies only when inertial and elastic forces are comparable. Recent simulations by Villone *et al.* [12] comprehensively explain the effect of fluid properties on particle migration in square-shaped geometries. Villone *et al.* predict that particles suspended in a viscoelastic constant-viscosity fluids (like the water solution PVP 8% wt), in inertialess conditions, always migrate towards the channel centreline, regardless of their initial positions, thus achieving a 3D particle focusing. These results are of course in contrast with those of Yang *et al.* [13] that showed five equilibrium positions in inertialess conditions. Villone *et al.* [12], in addition, showed that for shear-thinning fluids, a bistability scenario appears, in analogy to what occur in cylindrical microchannels. In this case however, there exists a well defined 'separatrix line' in the channel cross-section with a position strongly dependent on the flow: particles with initial positions 'below' the separatrix, i.e. included between the separatrix line and the centreline, migrate towards the channel centreline, while particles with initial positions 'above' the separatrix, migrate towards the channel walls. By increasing the flow rate and the nonlinear viscoelastic properties, the separatrix line approaches the centreline. It exists a condition for which all the particles migrate towards the channel walls, regardless of their initial position. The authors also showed that particles suspended in a viscoelastic fluid with a non negligible second normal stress difference N_2 migrate towards the channel centreline, the walls, and other positions dictated by the presence of secondary flows. This result about N_2 was recently experimentally confirmed by Lim *et al.* [20]. Very recently, Seo *et al.* [37] performed several experiments on the effect of the shear thinning on particle migration in square-shaped channel, by using the holographic microscopy. They found

that particles suspended in PVP 8% wt are always 3D focused on the channel centreline, in agreement with the simulation of Villone *et al.* [12]. They also reported experiments on shear-thinning fluids, finding that when exploring the fluid shear-thinning region, particles start to migrate away from the centreline. Nevertheless, they did not find the conditions predicted by Villone *et al.* [12] for which all the particles are focused at the channel corners. To the best of our knowledge, there are no experimental observations of this condition. We can therefore summirise by saying that particles suspended in a viscoelastic liquid can be 3D focused in a simple geometry, without any external field. Furthermore, many advantages in fabrication and controlling system can be obtained by simply using viscoelastic liquids.

1.3 Particle separation in microfluidic devices

In the previous sections we introduced the particle migration mechanism (Section 1.1.2) and presented several methods to achieve particle focusing (Section 1.2). In this section we proceed to report on several techniques for particle separation. Continuous particle separation in microfluidic device, in fact, is very common [5] and widely studied [6, 38]. In many cases, separation techniques use some of the previously described focusing methodologies.

1.3.1 Pinched flow fractionation

A first way to separate particle of different dimensions was presented by Yamada *et al.* [39], and is called *pinched flow fractionation*.

This technique is schematised in Figure 1.7. Liquid with particles is injected from the upper channel inlet while a second stream with the unloaded liquid come in from a side channel. The two currents 'meet'each other in the so-called pinched segment. In this segment, all the particles coming from the upper inlet are pushed towards the upper wall by the sheath flows (sheath flow focusing), in dependence on the imposed flow rate. Beyond the pinched segment, particles explore a sudden expansion; due to their differing fluid

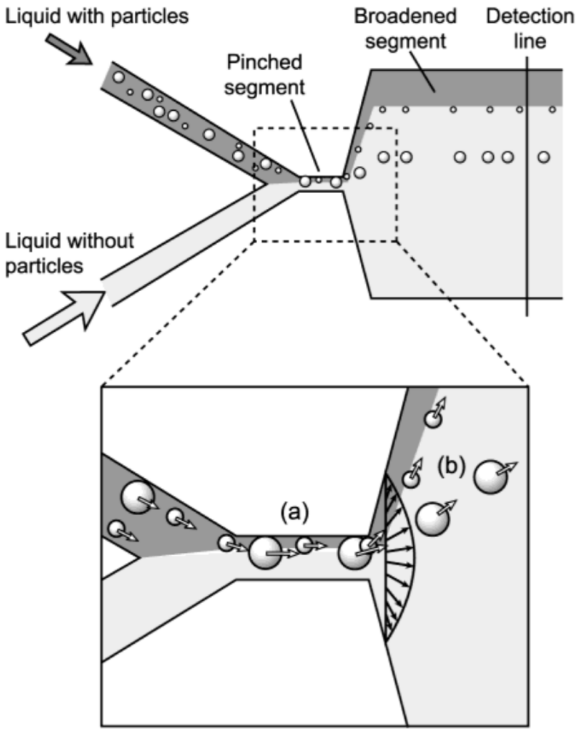

Figure 1.7: Schematic representation of pinched flow fractionation. Particles are previously focused on the upper wall by using a sheath flows. After the pinched segment, they are pushed on different flow line, i.e. are separated, basing on their size. Reprinted with permission from Yamada *et al.* [39]

dynamic conditions, particles experience different forces depending on their size. In particular, small particles follow a streamline close to the upper wall in the sudden expansion, while bigger particles flow close to the centreline.

This method allows to separate particles of 15 μm from particles of 30μm. The technique was also scaled down later [40] to separate particles of 1μm from particles of 2μm. The main advantage of this technique is its versatility, as separation of particles of various sizes can be achieved, while the disadvantages are the complex geometry design and in multiple inlet controlling.

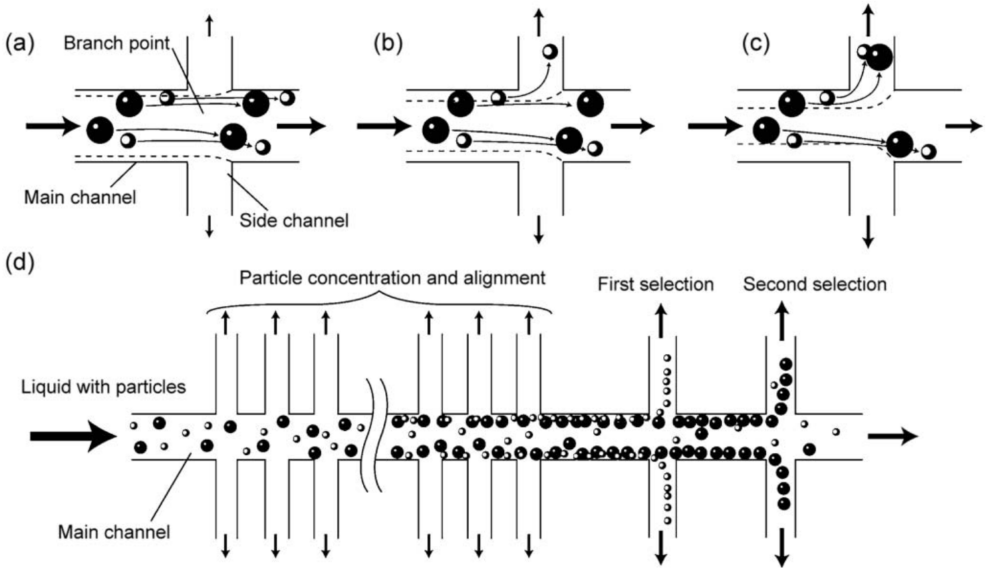

Figure 1.8: Schematic representation of hydrodinamic filtration. (a) Particles migrate towards the walls due to the presence of the lateral channels. (b) Particles smaller than a certain threshold (that depends on the channel design) flow in the lateral channel. (c) When a large part of the fluid flow in the lateral channels, bigger particles move in the lateral channels. (d) Overview of the separation technique. Reprinted with permission from Yamada *et al.* [41]

1.3.2 Hydrodynamic filtration

Another technique involving purely hydodrynamic effects is the so-called *hydrodynamic filtration* [41, 42], shown in Figure 1.8. The suspension containing particles of different sizes is injected from a common inlet. In this case there are no sheath flows and, in inertialess conditions, particles flow in the main channel without migrating transversally to the flow direction [7]. The main channel is surrounded by several lateral channels that are not inlets but outlets. All the particles are deflected towards the walls. Particles with a diameter smaller than a certain threshold (that depends on the channel design) flow in lateral channels (see Figure 1.8(a-b)), while 'bigger'particles

continue to flow in the main channel. Finally, when a large part of the flow has gone in the lateral channels, the remaining bigger particles also move in the side channels (see Figure 1.8c). By repeating this procedure several times, particles of different dimensions are separated by using only hydrodynamic effects (see Figure 1.8d). The main advantage of this technique is to manage and control just one inlet. Nevertheless, the device is very complex to fabricate, and is not versatile. In fact, the channel design strongly depends on the particle diameter and it is not always possible to use the same device to separate different 'couples' of particle sizes. With this method, particles of 1 and 3 μm were firstly separated. Afterwards, particles of 1 and 2 μm were also separated.

1.3.3 Deterministic lateral displacement

Amother important method for hydrodynamic particle separation is the so called *deterministic lateral displacement* (DLD) [43] a schematisation of which is shown in Figure 1.9. In this configuration, rows of obstacles are shifted with refer to each other of a certain amount (see Figure 1.9a), and then realigned again after few rows.

Imposing a laminar flow in y direction, particles diffuse around the obstacles following a specific path depending on their size. Particles quite smaller than the distance between obstacles will follow a certain path, but larger particles will follow a different path. Since this mechanism depends on the interaction between particles and obstacles only, it is possible to *deterministically* separate particles of different sizes. It is also possible to combine the flow around the obstacles with electric fields [6]. This combined method was used to separate DNA molecules of different dimensions in few seconds [45]. When DNA molecules go inside the microchip, they experience a first strong electric field E_1 applied diagonally, so they move in the E_1 direction without diffusing. E_1 is switched to a weaker electric field E_2 applied in x direction, so molecules diffuse around obstacles in different way due to their sizes. After this step, E_2 is switched to E_1 again, so molecules move diagonally and

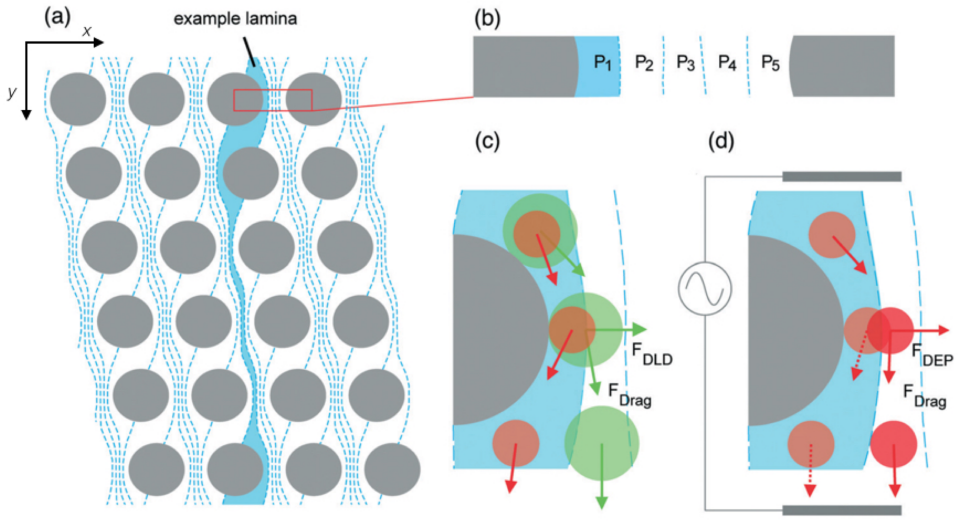

Figure 1.9: Schematic representation of the Deterministic Lateral Displacement DLD. (a) Example of laminar flow between the obstacles. (b) Magnification of the flow between the obstacles. (c) Force balance on the particles. Particles of different sizes follows different paths. (d) Force balance on the particles as in (c) when an electric field is involved. Reprinted with permission from McGrath *et al.* [44]

the cycle is repeated; at the end they are separated. This method allows the separation of DNA molecules, but with several problems due to the electric field and Brownian motion controlling.

Due to the its simplicity, DLD (with and without electric field) was widely used for several applications reviewed in [44]. The most important advantage of this technique is the possibility to determine particles or molecules paths *a priori*, thus achieving a really high efficiency as compared with other methods.

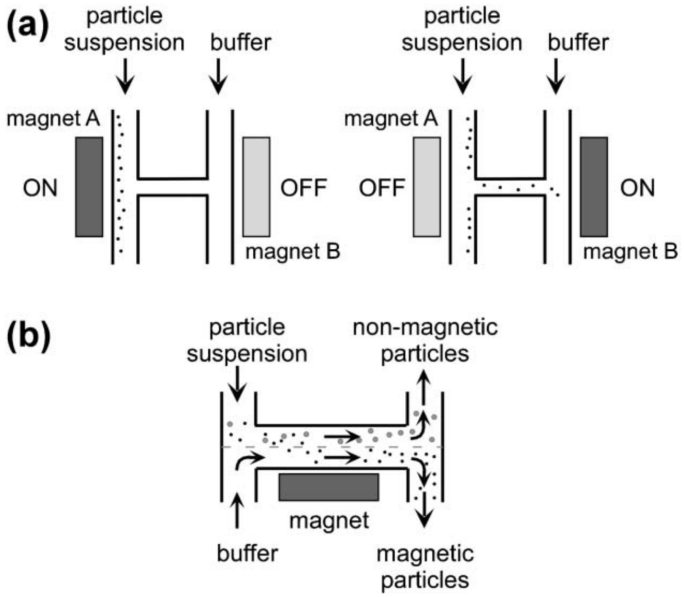

Figure 1.10: Principle of the H-shaped microchannel for (a) particle isolation in different streams and (b) separation in flow of magnetic from non magnetic particles. Reprinted with permission from Pamme [46]

1.3.4 Magnetophoresis-based separation

Magnetophoresis-based separation is widely used for several purposes such as magnetic particles/cells sorting and separation of particles/cells from a contaminated streamflow [6, 46]. Several devices to separate magnetic from non-magnetic particles or magnetic particles of different size have been proposed [46, 47]. A recently used design consists of a central separation chamber with two inlets and two outlets [46, 48, 49, 50].

This device is commonly referred to as 'H-shaped' channel (see Figure 1.10) [46]. In one inlet, the sample containing magnetic beads and non-magnetic particles is injected, whereas a buffer solution enters the other inlet at the same flow rate. Laminar flow prevents the mixing of the two streams in the separation chamber.

A magnetic field (e.g., generated by a permanent magnet) is used to recruit the magnetic beads towards the clean buffer stream. Xia et al. [48] inte-

grated a microfabricated high-gradient magnetic field concentrator (HGMC) at one side of the central chamber to separate magnetic beads from 1.6 to 2 μm in diameter, either bare or carrying bacteria, in a 200 $\times$ 50 μm rectangular cross-section microchannel with a separation efficiency of $\sim$ 90%. Kim *et al.* [49] were able to implement continuous immunoconjugation of 4.5 μm-diameter microparticles and 7.5 μm-diameter cells and their subsequent separation within a single microfluidic device. More recently, Wu *et al.* [50] studied the separation of Red Blood Cells conjugated with magnetic 1 μm microbeads. A multichannel version of this device has also been proposed, which is able to separate magnetic beads of different size [51]. In addition, sorting of cells from 9 to 13 μm in diameter, loaded with magnetic nano-particles was demonstrated [47].

1.3.5 Inertia-based separation

As anticipated in Section 1.1.1, particles subjected to inertial flow experience forces that push them towards some equilibrium position [21, 29]. The kinetics of inertial migration strongly depends on the particle dimension, in fact the inertial migration velocity $V_{inertial} \propto D_p^3$ [52]. However, it was predicted that particle equilibrium position is independent of particle size when the particle Reynolds Number $Re_p < 1$ [52]. In other words, particles with different dimensions will occupy the same spatial equilibrium positions. Thus, in these conditions, inertial-based particle separation is possible only when there is an additional force that acts on the particles in contrast with the lift force. As anticipated in Section 1.2, particles in curved microchannels experience the so-called Dean vortices that generate additional forces. Di Carlo *et al.* [52] proposed a serpentine microfluidic device that is able to separate particles and droplets with high efficiency and throughput. In particular, they separate 9 μm particles from 3.1μm particles with a purity of particles that varies from 99.9% for bigger particles to 56% for smaller particles.

An improvement of this technique was more recently presented by Kuntaegowdanahalli *et al.* [53] and a process device schematisation is reported

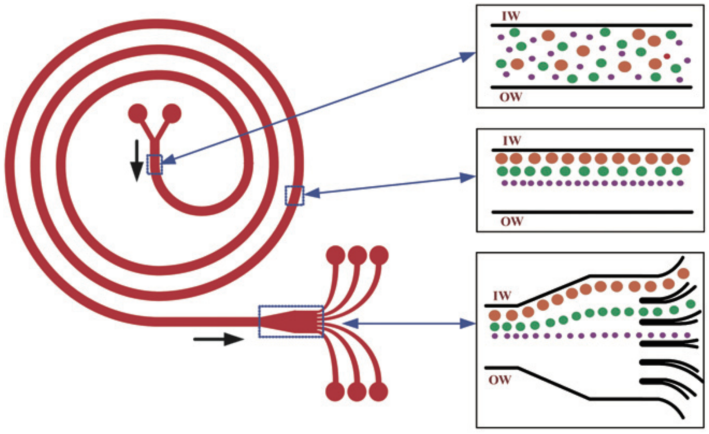

Figure 1.11: Schematisation of the microfluidic device. Particles are initially randomly distributed while after several spirals they are focused on different positions towards the inner wall. At the end they are separated in different channels. Reprinted with permission from Kuntaegowdanahalli *et al.* [53]

in Figure 1.11. In this device, particles of three different sizes, namely 10, 15 and 20 μm, are suspended in water all together. At the device inlet, particles injected from the inner inlet (left one in Figure 1.11) are randomly distributed between the inner and the outer wall. After some loops, particles occupy different equilibrium positions in dependence on their size. At the end, particles are collected in three different channels (for each half of the main channel). Particles are separated in a 5-loop Archimedean spiral microchannel with an efficiency of $\sim$90%. In order to prove the versatility of the device, the authors separate neuroblastoma and glioma cells with an efficiency around 80%. In addition with this device it is possible to achieve a throughput of $\sim$1 millioncells/min. Other more recent applications of inertial-based microfluidic can be found in [54, 55].

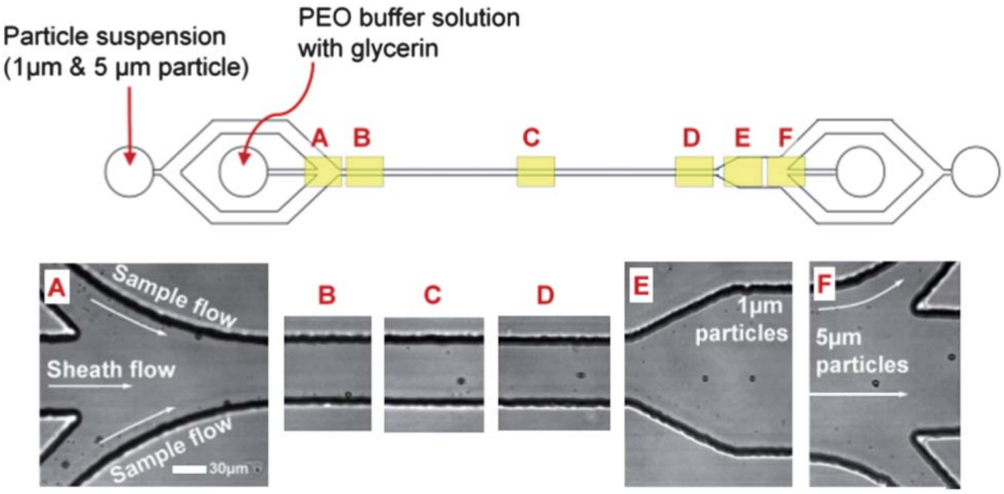

Figure 1.12: Schematisation of the separation device. Particles are injected from two side inlets and are pushed towards the walls from the central sheath flow. Then bigger particles migrate towards the channel centreline while smaller one stay closed to the wall. Reprinted with permission from Nam *et al.* [56]

1.3.6 Viscoelasticity-based separation

In Sections 1.1.2 and 1.2.4, we saw that particles suspended in a viscoelastic fluid and subjected to a Poiseuille flow can migrate transversally to the flow direction, by occupying some equilibrium positions depending on the flow rate Q, the fluid relaxation time λ, and the fluid properties (constant viscosity or shear-thinning). The particle viscoelastic migration velocity is strongly size dependent [10]. Hence, particles of different sizes, in the same channel, can reach their equilibrium position with different kinetics. In other words, for a given channel length L, particles of different sizes will occupy different positions in the channel. Yang *et al.* [13] were the first to separate particles of different sizes (5.4 and 2.4 μm) in a device made of a straight channel and an abrupt expansion, just by using fluid viscoelasticity. In another work, Yang *et al.* [57] use the same procedure of ref. [13] to separate red-blood

cells from particles because of their different migration behaviours.
Nam *et al.* [56] use the device schematised in Figure 1.12 to separate particles of 1 μm and 5 μm with an efficiency $\sim$99%. In particular, particles of different sizes are injected from two side inlets and are all pushed towards the two walls by the central sheath flow. Then, bigger particles start to migrate towards the channel centreline, while smaller ones stay close to the wall. In this way, at the channel outlet, particles of different sizes can be collected in different streams. They also use the same device to separate platelets from red blood cells with a purity of 99.9%.

Very recently Ahn *et al.* [58] extended the work of Yang *et al.* [13], by considering the effects of the initial particle concentration (particle-particle interactions play in fact a significant role), of the polymer concentration in the suspending matrix, and of the flow rate on the separation efficiency in a simple straight channel.

Recently D'Avino [59], presented a numerical study on the non-Newtonian deterministic lateral separator. He found that a shear-thinning fluid gives rise to a lower 'critical diameter', i.e. the diameter for which two different particles (one larger and one smaller than such diameter) follow different paths, in the deterministic lateral displacement constriction. Thus, by using a shear-thinning fluid as a suspending liquid, it is possible to tune opportunely the critical diameter for a fixed design.

Chapter 2

Materials and Methods

2.1 Suspending fluids and particles

Fluids

Several polymers in water solutions at different mass concentrations were used in this work.

Poly Vynil Pyrrolidone (PVP), with average Molecular weight M_w=360 kDa, was purchased by Sigma Alderich. Aqueous solutions of PVP at mass concentration of 8% have been used. The solutions were stirred at 400 rpm by using a magnetic stirrer for 24 h at $T \sim 40°C$.

PolyEthylene Oxide (PEO), with average Molecular weight M_w=4 MDa, was purchased by Sigma Alderich. The solvent used to prepare the solutions is a glycerol-water solution at 25% wt of glycerol, in order to avoid particle sedimentation problems. The solvent viscosity is $\eta = 0.002$ Pa·s. Solutions of PEO at several mass concentrations ranging from 0.08% to 0.8%, have been used. The solutions were stirred at 400 rpm by using a magnetic stirrer for 24 h at $T \sim 25°C$.

Non-ionic PolyAcrylamide (niPAM), with average Molcular weight M_w=5-6 MDa, was purchased by Sigma Alderich. The solvent used to prepare the solutions is a glycerol-water solution at 25% wt of glycerol, in order to avoid particle sedimentation problems. The solvent viscosity is again $\eta = 0.002$

Pa·s. Solutions of niPAM at several mass concentration ranging from 0.05% to 0.5%, have been used. The solutions were stirred at 400 rpm by using a magnetic stirrer for 12 h at $T \sim 25°C$. NiPAM have also been used for the experiments discussed in Section 5.2; in particular an aqueous solution 0.5% w/w was used.

Two ionic PolyAcrylAmides (iPAM, from Polysciences Inc.) having nominal molecular weight of $M_w = 1,500\ Da$ and of $M_w = 1,145,000\ Da$ were used to prepare aqueous solution at mass concentrations ranging from $\approx 5\%\ w/w$ to $\approx 40\%\ w/w$ and from $\approx 0.1\%\ w/w$ to $\approx 1\%\ w/w$, respectively. The solutions were stirred at 200 rpm for 48 h at room temperature.

HydorxyEthyl Cellulose (Average Molcular weight M_w=250 kDa) was purchased by Sigma Alderich. Aqueous solutions of HEC at mass concentrations of 0.05%, 0.08%, 0.1%, 0.2%, 0.3%, 0.4%, 0.5%, 0.8% w/w, have been investigated. The solutions were stirred at 200 rpm for 48 h at room temperature.

Particles

Two sets of polystyrene (PS) particles (Polysciences) with diameter 5.8±0.6 μm and 10±1 μm are used. In both cases, a dilute suspension with a volume fraction $\phi = 0.01\%$ is prepared. Particles are added to the matrix and put in a mixer (Vortex, Falc Instruments) to guarantee a good dispersion, and then in an ultrasonic bath (Falc Instruments) to remove air bubbles; this procedure is repeated before each experiment. The PS particles have a density $\rho_\mathrm{p} = 1.05$ g/ml; we estimate that PVP solution has a density $\rho = 1$ g/ml. A rough calculation of the sedimentation velocity from the Stokes law shows that this density mismatch does not induce any relevant particle sedimentation effect in our experimental timescales. Regarding PEO and PAM solutions, the amount of glycerol in the solution matches the particle density, therefore no sedimentation occurs. Regarding the experiments reported in Section 5.2, magnetic, Nickel-covered spherical particles (Dynabeads) with diameter $D_\mathrm{p} = 10 \pm 1$ μm, $\rho_\mathrm{p} = 1.1$ g/ml, magnetisation $m = 1.8$ emu/g

have been suspended in aqueous solution of niPAM 0.5% w/w, with a volume fraction $\phi = 0.02$.

2.2 Rheological Measurements

Rheological measurements were performed by using a stress-controlled rotational rheometer MCR 302 (Anton Paar Instrument) able to detect Torque down to about $\sim 0.1\ \mu Nm$. The measurements were performed with a cone and plate geometry of 50 mm and of 60 mm diameter and equipped with a solvent trap to avoid fluid evaporation. Temperature was kept to $22°C$.

2.3 Microfluidic Devices Fabrication

In this section we present the two different fabrication techniques used to produce the devices used in this work. All the experiments described in Chapter 4 and in Section 5.1 were carried out in a square-shaped microchannel made of Poly Methyl Metachrilate (PMMA), while the experiments discussed in Section 5.2 were carried out in a PolyDimMthylSiloxane (PDMA) microdevice. Both techniques are presented in the follow.

Poly Methyl Metachrilate (PMMA) Device

The square-shaped microchannel is milled on the PMMA substrate (PMMA, substrate thickness 1 mm, Goodfellow) using the Micromilling (Minitech CNC Mini-Mill): a 2 mm tip is first used to mill all the substrate of 150 μm to guarantee level uniformity. A tip with the same dimension of the channel side is, then, inserted in the machine to mill the channel. Finally, two holes are made in the substrate to prepare the access to the inlet and the outlet of the channel (see below). An analysis with a profilometer (Veeco Dektak 150) has been performed to confirm that the accuracy of the channel depth is within 10%. The channel is bonded on another PMMA substrate by immersing the two pieces in absolute ethanol (from Sigma-Aldrich) for about

20 minutes, clamping them together and putting in the oven at $T = 40^\circ$ C for about two hours.

PolyDimMthylSiloxane (PDMA) device

In this case we proceeded in two main steps: i) Fabrication of the master mold; ii) PDMS replica on the master fabricated in i).

i) The master mold was made of Poly Methyl MethAcrylate (PMMA, substrate thickness 1 mm, Goodfellow) by following the same steps described above without the bonding part.

ii) A PolyDiMethylSiloxane (PDMS) master has been obtained from the PMMA mold as follows. Dow Corning Sylgard 184 Silicone elastomer and curing agent (10:1 in weight) were thoroughly mixed. The mixture was degassed in a vacuum chamber for 30 minutes in order to remove air bubbles arising from the mixing. Afterwards, the mixture was poured on the PMMA mold and cured at 80°C for 2 hours. Such a temperature is below the PMMA melting temperature (~ 95°C), thus assuring that the channels milled on the PMMA block do not deform. After curing, the PDMS was peeled off the PMMA block. Solid PDMS was used as an intermediate master to generate PDMS replicas of the microfluidic device by pouring liquid PDMS on it. In order to prevent adhesion of the PDMS replicas on the PDMS master, this was immersed for about 2 minutes into a silane solution, i.e., a mixture of 94% v/v isopropanol (Sigma Aldrich), 1% acetic acid (Sigma Aldrich), 1% Fluorolink S10 (Solvay), and 4% deionized water [60]. Then, the PDMS master was placed in the oven at 120°C for 30 minutes, thus allowing a complete reaction of the master PDMS surface with the fluorinated polymer. The treated PDMS master was thoroughly rinsed in ethanol and cleaned in an ultrasonic bath (20 min). To make a replica, PDMS mixture (10:1) was poured on the silanized PDMS master and cured as described above, and finally peeled-off. Inlets and outlets were created by using a puncher. The PDMS replica was bonded on a glass microslide after performing an oxygen plasma treatment with a Plasma cleaner (Diener Electronics-Femto) at 50 W

and 0.4 mbar for 1 minute. Then, the microfluidic chip was incubated in the oven at 120°C for 1 hour to complete glass-PDMS bonding. Finally, Teflon pipes were sealed on the two inlets with standard PDMS that was cured at 120°C for 15 minutes.

2.4 Feeding system

The flow rate is controlled by a syringe pump (Nemesys apparatus), using glass syringes. This machine is able to discriminate different flow rates with a precision of 0.001 μl/min. The flow rates applied vary in the range 0.01 μl/min $\leqslant Q \leqslant$ 12 μl/min. Steady state conditions and absence of possible leaking are verified through the invariance of the particle velocity.

2.5 Atomic Force Microscopy Measurements

Atomic force microscopy (AFM) imaging, used in Section 3.4, was performed using a JPK NanoWizard II Bio AFM (JPK, Germany), in combination with an MLCT-UC (Bruker company) cantilever (spring constant = 0.01 N/m). The AFM is mounted upon a Zeiss Observer A1 Axio (Zeiss, UK) confocal microscope, which is used for the alignment and positioning of the AFM cantilever upon the sample. The imaging process was undertaken in contact mode in air at room temperature.

2.6 Particle distributions

Particles flowing in the channel are observed using an inverted microscope (Olympus Flash IX-71) and a straight microscope (Olympus BX63) with a 4x objective to reach the best field of depth without losing information on particle motion. Image sequences are collected with a fast camera (IGV-B0620M, Imperx and CCD Hamamatsu) at a frame rate variable between 10 and 600 fps depending on the flow rate. The observations are all made at a

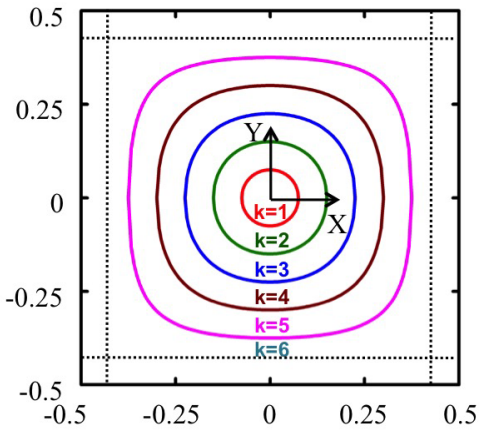

Figure 2.1: Concentric bands dividing the channel cross-section used to compute the particle distributions. X and Y are the dimensionless coordinates of the channel cross-section. The dashed lines delimit the region accessible to the particles. The bands are progressively numbered from the inner one ($k = 1$) to the outer one ($k = 6$). Notice that the first band has almost the same dimension of the particle.

fixed distance from either channel inlet. All the experiments are performed at room temperature.

The velocity distributions are measured by particle tracking. To quantify the particle focusing, we evaluate the fraction of particles passing in a certain zone of the square cross-section by considering concentric *bands*, as reported in Figure 2.1. We compute the fraction f_k of particles in the band k as [11]:

$$f_k = \frac{\frac{n_k}{A_k \overline{v}_k}}{\sum_k \frac{n_k}{A_k \overline{v}_k}} \tag{2.1}$$

where n_k is the number of particles flowing in the band k (always at a fixed distance from the inlet), A_k and $\overline{v}_k$ are the cross-sectional area and the average velocity of the band k, respectively. The normalization of each n_k in Eq. (2.1) through the product $A_k \overline{v}_k$ in Eq. (2.1) is made to properly take into account that different bands have different areas and velocities. To obtain a

good statistical sample, at each flow rate we collect a number of frames to get, in total, more than 100 particles.

To describe the procedure adopted to compute the number of particles in each band n_k, let us introduce a Cartesian reference frame with the origin at the center of the channel cross-section. (The coordinates are made dimensionless by using the cross-section side H as characteristic length.) We denote with Z the flow direction, and with X and Y the directions parallel and orthogonal to the plane containing the device (see Figure 2.1). From the particle tracking experiments, we measure the particle velocity V_z along the flow direction as well as the coordinate X_p of the particle center. Notice that the two particle velocity components within the channel cross-section, V_x and V_y, which contribute to the migration velocity, are not directly visualized from the tracking method. Indeed, migration is a very slow process, and no appreciable change in those velocities can be detected in the observation window used in our analysis (that covers a distance of about 1 mm).

To locate a particle with a known translational velocity V_z in one of the bands, we performed preliminary numerical simulations (the details are given in the next subsection) aimed to calculate the velocity of a sphere along the flow direction in a square-shaped channel for different positions in the cross-section, i.e. the function $V_\mathrm{z,sim}{=}V_\mathrm{z,sim}(X_\mathrm{p}, Y_\mathrm{p})$, where the subscript 'sim' stands from simulated velocity. The solid lines in Figure 2.1 are the isovelocity contours $V_\mathrm{z,sim}(X_\mathrm{p}, Y_\mathrm{p}) = V_k$ with V_k a velocity value depending on the band k. We select V_k as the values such that the corresponding isovelocity curves divide the cross-section semiaxes in six equally-spaced segments. In this way, the knowledge of the measured particle velocity V_z and of the calculated $V_\mathrm{z,sim}$ univocally allows to collocate a particle in a specific band. Notice that, with the adopted choice for V_k, the first band, bounded by the red curve, is only slightly larger in size than the particle.

The procedure just discussed is similar to the one used for a cylindrical channel [11, 61]. However, in the latter case, the fluid velocity field without particles was considered. In all the experiments of Section 4.1 and Section 5.1,

we account for the effective particle velocity, thus getting high accuracy, especially far from the channel center, where confinement leads to large 'slip velocities' (defined as the difference between the actual particle velocity and the virtual fluid velocity at the same position of the particle). Therefore, in Figure 2.1, the solid lines are the loci of points corresponding to the same velocity of the particle (and not of the 'empty' fluid). The details of these simulations are reported in Section 2.10. On the other hand for the experiments of Section 4.2 and 4.3, we used numerical simulations of the unloaded fluid. The details of these simulations are given in Section 2.10

The knowledge of the particle coordinate X_p and of the particle translational velocity, combined with the numerically computed velocity map, now allows us to find out the exact position of the particle within the band. Indeed, the following equation:

$$V_{\mathrm{z,sim}}(X_\mathrm{p}, Y_\mathrm{p}) = V_\mathrm{z} \tag{2.2}$$

can be solved for Y_p giving the coordinate of the particle center along the observation direction. Notice that, in Eq. (2.2), the quantities X_p and V_z are measured by experiments, whereas the functional form of $V_{\mathrm{z,sim}}$ is computed by simulations.

2.7 Microrheological Measurements

All the microrheology data in Section 3.3 and 3.4 were derivded by using Optical tweezers. Optical trapping was achieved by means of a titanium-sapphire laser with a 5 W pump (Verdi V5 laser; Coherent Inc.), which provides up to 1 W at 830 nm. OT are built on an inverted microscope, where the same objective lens (100x, 1.3 numerical aperture, Zeiss, Plan-Neofluar) is used for both focus the trapping laser beam and visualise the thermal fluctuations of a single 5μm diameter silica bead. Samples were mounted on a motorized microscope stage (Prior Pro-Scan II). A CMOS camera (Dalsa Genie HM640 GigE) was used to collect high-speed images of

a reduced field of view. These images were processed in real time at ∼1 kHz using homemade LabVIEW (National Instrumens) single-particle-tracking software [62] running on a personal computer. Note that each trajectory was made from at least 10^6 data points.

2.8 Microrheology with Optical Tweezers

When a micro-sized spherical particle is immersed in a fluid at thermal equilibrium, it experiences random forces due to thermal fluctuations of the surrounding fluid's molecules; these forces generate the so called Brownian motion of the particle. The statistical mechanics study of the particle trajectory has the potential of providing information on the viscoelastic properties of the suspending fluid as introduced by Mason and Weitz [63] in the case of freely diffusing particles. When the particle fluctuations are constrained by a harmonic potential generated by the optical tweezers, the particle trajectory can be described by means of a generalised Langevin equation [64]. The stiffness of the optical trap k can be easily determined by applying the principle of equipartition energy:

$$\frac{d}{2}k_bT = \frac{1}{2}k\langle r_j^2\rangle \tag{2.3}$$

where $\langle r_j^2\rangle$ is the time-independent variance of the Carteisan component ($j = x, y, z$) of the (d)-dimensional vector describing the particle's displacement from the trap center, the origin of $\boldsymbol{r}$. For example, Figure 2.2a shows the y-component of the trajectory of an optically trapped $5\mu m$ diameter bead suspended in water.

The linear viscoelastic properties of a fluid are fully defined by its shear complex modulus: $G^*(\omega) = G'(\omega) + iG''(\omega)$, which is a complex number that provides information on both the elastic and viscous nature of the fluid. In particular, the real part $G'(\omega)$ is called storage (elastic) modulus and the imaginary part $G''(\omega)$ is called loss (viscous) modulus and they provide information on the viscoelastic nature of the fluids.

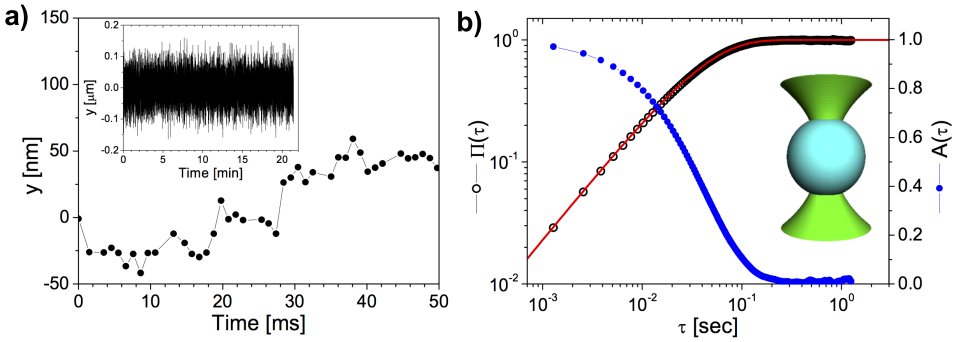

Figure 2.2: a) The y-component of the trajectory of an optically trapped $5\mu m$ diameter bead suspended in water over a period of $50ms$. The inset shows the same component as before, but over the entire experiment of $\sim$ 22 min. b) The normalised position autocorrelation function A(τ) and the normalised mean square displacement $\Pi(\tau)$ *versus* lag-time τ evaluated from the trajectory shown on the left. The red line is the theoretical prediction for such a system: $\Pi(\tau) = 1 - e^{-\lambda\tau}$[64]; where $\lambda = \kappa/(6\pi a\eta)$, κ the trap stiffness, η the fluid viscosity and a the bead radius. The inset is a schematic view of an optically trapped glass bead.

We now proceed to describe a novel method to derive the relative viscosity with optical tweezers without applying Fourier transform [65]. In particular the value of the relative viscosity $\eta_r = \eta/\eta_s$ (with η the fluid viscosity and η_s the solvent viscosity), is a direct reading from the Normalised Positions Autocorrelation Function (NPAF). This method was used to derive η_r values for ionic-PAM and HydroxyEthyl Cellulose in Sections 3.3 and 3.4. We therefore proceed to describe more in deeper this method. In the simplest case when a particle of radius a is suspended into a Newtonian fluid (i.e. a fluid with constant viscosity η and no elastic components), the particle normalised position autocorrelation function assumes the form of a single exponential decay [64]:

$$A(\tau) \equiv \frac{\langle x(t_0)x(t_0+\tau)\rangle_{t_0}}{\langle x^2\rangle_{eq}} = e^{-\lambda\tau} \tag{2.4}$$

where $\lambda = \kappa/(6\pi a\eta)$ is the characteristic relaxation rate of the compound sys-

tem (also known as the "*corner frequency*" [66]). In the NPAF definition, the brackets $\langle \cdots \rangle_{t_0}$ indicate the average taken (by time-translation invariance) over all initial times t_0 within a single trajectory, τ is the lag-time (or time interval $(t - t_0)$), $x(t)$ is the one dimensional particle position from the trap centre (which is assumed to be coincident with the origin of the coordinate system), and $\langle x^2 \rangle_{eq}$ is the equilibrium variance of the bead position. Notice that, the calibration method based on the *principle of equipartition energy* (see above) is independent from the rheological nature of the fluid under investigation, i.e. from its Newtonian/non-Newtonian character. However, when changing the suspending fluid (e.g., by changing concentration) or the laser properties (e.g., the laser power), the calibration procedure to determine κ must of course be repeated, because variations of the experimental conditions will affect the measured variance $\langle x^2 \rangle_{eq}$, hence the stiffness κ. From Eq (2.4), with a simple change of variables, it is possible to write:

$$A(\tau^*) = e^{-\tau^*/\eta_r} \tag{2.5}$$

where $\tau^* = \tau\kappa/(6\pi a \eta_s)$ is a *dimensionless* lag-time containing the pure solvent Newtonian viscosity η_s. It follows that, in an $A(\tau^*)$ *vs* τ^* plot, by drawing a horizontal line starting from the ordinate e^{-1}, the abscissa of its intercept with $A(\tau^*)$ provides a *direct reading* of the solution relative viscosity η_r. Notably, in the case of pure solvent (water), the abscissa of the intercept of e^{-1} with $A(\tau^*)$ is 1.

In general, polymer solutions as those employed in this work are non-Newtonian, especially at relatively high concentrations where the viscosity may not be constant, particularly at high frequencies (or high shear rates). It follows that Eq. (2.4) may not be valid for those solutions, at least not for all concentrations. In dilute conditions, however, at relatively low polymer concentrations, most of solutions tend to show a Newtonian behaviour over a wide range of shear rates (e.g. see Figure 3.2), and this is especially so towards vanishingly small values of concentration, which *coincidentally* are the same conditions required for measuring $[\eta]$. Hence, the applicability of Eqs. (2.4) and (2.5) for measuring η_r, and therefore $[\eta]$, is confirmed in those conditions.

When considering more concentrated solutions, we can argue as follows. It is always possible to write the NPAF in the general form:

$$A(\tau^*) = A_0(\tau^*)e^{-\tau^*/\eta_r} \tag{2.6}$$

The above described graphical procedure will therefore stay valid in general, i.e. for whatever solution concentration, if the following two conditions are met: i) $\tau_D\lambda_0 \ll 1$, where τ_D is the fluid's longest relaxation time and $\lambda_0 = \kappa/(6\pi a\eta_0)$ is the system corner frequency evaluated with the solution zero-shear viscosity η_0; ii) $A_0(\tau^* \geq \tau_D^*) \simeq 1$, where τ_D^* is a dimensionless time equals to $\tau_D/(6\pi a\eta_s/\kappa)$. Condition ii) simply states that the $A(\tau^*)$ function decays exponentially beyond τ_D^*, and, more importantly, that its 'initial decay', i.e. below τ_D^*, is *small* when compared to its 'complete decay', up to $A(-) = 1/e$. When taken together, therefore, conditions i) and ii) simply state that there exists a *large* range of lag-times $\tau_D < \tau \lesssim \lambda_0^{-1}$, where the decay described by Eqs. (2.6) is in fact indistinguishable from one mathematically described through Eq. (2.5). (Notice that, for $\tau > \lambda_0^{-1}$ the elastic component of the OT dominates the particle dynamics whatever the nature of the surrounding fluid.)

It is clear that, with the two just mentioned conditions fulfilled, the graphical procedure illustrated above will work properly even under non-dilute conditions. Of course, in rheological investigations, the fulfilling of conditions i) and ii) above is uncertain prior of performing the measurements, simply because the parameters τ_D and η_0 are yet unknown. As a practical recipe, therefore, we should simply look, when measuring the NPAF, to the linearity of the log-linear plot of $A(\tau^*)$ *vs* τ^*; if linearity is there, then η_r can be directly obtained, irrespective of other rheological measurements aimed to ascertain the Newtonian/non-Newtonian nature of the solution under investigation. In all the OT experimental data reported in Figures 3.7, 3.8 and 3.10, we have been ensured about the linearity of $A(\tau^*)$.

2.9 Dimensionless parameters

In this section we proceed to present several dimensionless parameters used in this work. The entity of fluid viscoelasticity can be quantified by the Deborah number defined, for a rectangular-shaped channel, as:

$$De = \frac{\lambda}{t_f} = \frac{\lambda Q}{H^2 W} \tag{2.7}$$

It is obvious that for square-shaped microchannel $De = \lambda Q/H^3$ because $H = W$. The Deborah number is the ratio between the fluid relaxation time λ and the flow characteristic time $t_f = H^2W/Q$. When $De = 0$ the fluid is Newtonian because $\lambda = 0$, while increasing De corresponds to more pronounced elasticity.

Another important parameter for the system under investigation is the Reynolds number:

$$Re = \frac{\rho Q}{\eta H} \tag{2.8}$$

i.e. the ratio between inertial and viscous forces.

Yang *et al.* [13] compared viscoelastic and inertial forces through the *Elasticity number*:

$$El = \frac{De}{Re} = \frac{\lambda \eta}{\rho H^2} \tag{2.9}$$

Viscoelastic or inertial forces are dominant when $El \gg 1$ or $El \ll 1$, respectively, whereas, if $El \sim 1$, the viscoelastic forces are comparable with the inertial ones. We anticipate here that, basing on the results of Section 4.3, this number is not sufficient in describing the synergic effect of inertia and elasticity.

Another important parameter is the so-called *confinement ratio* defined as:

$$\beta = \frac{D_p}{H} \tag{2.10}$$

A value of $\beta \sim 0.1$ is sufficient to promote non-linear phenomena in several flow conditions [11, 12, 13].

In order to analyse data of Section 5.2, we need to define a dimensionless number that involves a magnetic field. In particular we need of a parameters that compares the viscous force with the magnetic one. At this aim, let us consider a magnetic spherical particle with diameter D_p suspended in a viscoelastic fluid flowing in a straight microchannel. A cubic permanent magnet with side length l_m is located at a distance l_m from the side of the channel. We denote with x the flow direction, and y and z the directions that identify the channel cross-section. In microfluidic flows, inertial forces are commonly negligible with respect to viscous forces; therefore, the Reynolds number Re, that gives the relative weight of these two forces, is much less than unity. In the assumption of no particle sedimentation, the magnetic bead is subjected to a drag viscous force $\boldsymbol{F}_\mathrm{D}$, a magnetic force $\boldsymbol{F}_\mathrm{Mn}$ due to the permanent magnet and an elastic force $\boldsymbol{F}_\mathrm{el}$ due to the fluid viscoelasticity. These forces can be expressed as follows:

$$\boldsymbol{F}_\mathrm{D} = 3\pi\eta D_\mathrm{p}(\boldsymbol{u}_\mathrm{f} - \boldsymbol{u}_\mathrm{p}) \tag{2.11}$$

$$\boldsymbol{F}_\mathrm{Mn} = \frac{\pi D_\mathrm{p}^3}{6}\mu_0\frac{\chi_\mathrm{eff}}{2}\nabla H^2 \tag{2.12}$$

$$\boldsymbol{F}_\mathrm{el} = A\, D_\mathrm{p}^3\nabla N_1 \tag{2.13}$$

In Eq. (2.11), the Newtonian drag expression is used with η the fluid viscosity, and $\boldsymbol{u}_\mathrm{f}$ and $\boldsymbol{u}_\mathrm{p}$ the fluid and particle velocities. The magnetic force in Eq. (2.12) assumes that the particles are not magnetically saturated, so that their magnetization is a linear function of the magnetic field $\boldsymbol{H}$ (see, e.g., [67]). In this equation, μ_0 and χ_eff are the permeability of vacuum and the effective susceptibility of the beads which is related to the intrinsic susceptibility χ_i through $\chi_\mathrm{eff} = \chi_\mathrm{i}/(1 + \chi_\mathrm{i}/3)$ [67, 68]. Finally, the viscoelastic force in Eq. (2.13), is proportional to the gradient of the first normal stress difference $N_1 = T_\mathrm{xx} - T_\mathrm{yy}$, where $\boldsymbol{T}$ is the fluid stress tensor [10, 11] and A is a numerical factor. The normal stresses arise from fluid viscoelasticity and are responsible for particle migration.[10, 11, 69] The first normal stress difference can be rewritten as $N_1 = \Psi_1\dot{\gamma}^2$ where Ψ_1 is the first normal stress difference coefficient and $\dot{\gamma}$ is the shear rate.

A force balance on the magnetic bead leads to:

$$\boldsymbol{F}_{\mathrm{D}} + \boldsymbol{F}_{\mathrm{Mn}} + \boldsymbol{F}_{\mathrm{el}} = \boldsymbol{0} \tag{2.14}$$

Eq. (2.14) allows to calculate the velocity of the particle $\boldsymbol{u}_{\mathrm{p}}$ and, then, its trajectory in the channel. By using the expressions given in Eqs.(2.11)-(2.13), the force balance reads in dimensionless form as:

$$\begin{aligned} \boldsymbol{u}_{\mathrm{p}}^{*} =& \boldsymbol{u}_{\mathrm{f}}^{*} + Mn_{\mathrm{p}} \nabla^{*} \left[H^{*} \left(x_{\mathrm{p}}^{*}, y_{\mathrm{p}}^{*}, z_{\mathrm{p}}^{*}, l_{\mathrm{m}}^{*}, s_{\mathrm{m}}^{*} \right) \right]^{2} + \\ & CDe\beta^{2} \boldsymbol{f}^{*} \left(y_{\mathrm{p}}^{*}, z_{\mathrm{p}}^{*}, \frac{W}{H} \right) \end{aligned} \tag{2.15}$$

where starred symbols denote dimensionless quantities. Notice that the channel height H has been chosen as characteristic length and the average fluid velocity $Q/(WH)$ as characteristic velocity, where Q is the flow rate and W the channel width. The function $\boldsymbol{f}^{*}$ accounts for the shear rate gradient term arising from Eq. (2.13). Such a term can be derived from the fully developed velocity field in the rectangular channel which is available as a series solution [70, 71]. The function $\boldsymbol{f}^{*}$ depends on the particle position along the channel cross-section and on the aspect ratio of the cross-section W/H with W the width of the channel. The magnetic field is a function of the particle position in the channel, the distance between the magnet and the channel side l_{m} and the magnet side length s_{m}.

Eq. (2.15) contains the dimensionless parameter 'particle magnetization number', which compares magnetic and viscous forces. In symbols:

$$Mn_{\mathrm{p}} = \frac{D_{\mathrm{p}}^{2} w}{18 \eta Q} \mu_{0} \frac{\chi_{\mathrm{eff}}}{2} \left(\frac{B_{\mathrm{r}}}{\mu} \right)^{2} \tag{2.16}$$

in which Q is the flow rate, B_{r} is the remanence of the magnet and μ is the permeability of the beads.

In Eq. (2.15), other parameters are the channel aspect ratio W/H, the distance of the magnet from the channel side l_{m}^{*} and the length of the magnet s_{m}^{*}. Notice that all these parameters are related to the geometry of the system. Finally, C is a numerical factor.

2.10 Numerical simulations

Fluid loaded with particle

3D numerical simulations have been performed to derive the translational velocity of a spherical particle in a square-shaped channel in a pressure-driven flow. The suspending liquid was assumed to be inertialess and Newtonian. The no-inertia assumption is motivated by the negligible Reynolds number for the conditions of our experiments (see later). The second assumption derives from the polymer solutions' rheology at small mass concentrations (see Figure 3.1, 3.2, 3.5, 3.10),that shows a constant viscosity over the whole range of shear rates of experimental interest. If a particle is included in the fluid, the elastic stress distribution around the particle will alter its motion. However, the effect of the fluid elasticity on the slip velocity has been found to be quite small [72], and the Newtonian approximation is therefore acceptable.

With those assumptions, the governing equations for the fluid motion are the continuity and the momentum equations:

$$\nabla \cdot \boldsymbol{v} = 0 \tag{2.17}$$

$$-\nabla p + \eta \nabla^2 \boldsymbol{v} = \mathbf{0} \tag{2.18}$$

where $\boldsymbol{v}$ is the fluid velocity and p is the pressure. Regarding the boundary conditions, no-slip is imposed at the channel walls, periodic boundary conditions are prescribed between the inflow and outflow sections, together with a flow rate Q in inflow. Finally, the rigid-body motion is imposed at the particle surface:

$$\boldsymbol{v} = \boldsymbol{V_p} + \boldsymbol{\omega}_p \times (\boldsymbol{r} - \boldsymbol{r}_p) \tag{2.19}$$

with $\boldsymbol{V}_p$ and $\boldsymbol{\omega}_p$ the (unknown) translational and angular particle velocities, and $\boldsymbol{r}_p$ its center. Because of the inertialess assumption, the total force and torque acting on the particle surface are zero. Details on the numerical procedure are given elsewhere [11].

For a specific initial position $(X_{\mathrm{p0}}, Y_{\mathrm{p0}})$ of the particle in the channel cross-section, the solution of the above system of equation gives the velocity and

pressure fields along with the translational velocity $V_{\mathrm{z,sim}}$ (notice that $V_{\mathrm{z,sim}}$ is the only non-zero component of $\boldsymbol{V}_p$, as no migration occurs in an inertialess Newtonian fluid). By changing the initial coordinates of the particle center on a regular grid and by interpolating the computed velocity data with an high-order polynomial function, we end up to an expression for $V_{\mathrm{z,sim}}(X_{\mathrm{p}}, Y_{\mathrm{p}})$ that can be used for calculating the particle fraction, as previously described.

Unloaded fluid

Numerical simulations of the velocity profile of the fluid without particles in the square-shaped microchannel are performed, to be used in Section 4.2 and 4.3, together with particle tracking experiments, to reconstruct the particle positions. The following governing equations are solved by the finite element method:

$$\nabla \cdot \boldsymbol{v} = 0 \tag{2.20}$$

$$-\nabla p + 2\nabla \cdot [\eta(II_{\boldsymbol{D}})\boldsymbol{D}] = \boldsymbol{0} \tag{2.21}$$

where $\boldsymbol{v}$ is the fluid velocity, p the pressure, $\eta(II_{\boldsymbol{D}})$ the local shear rate dependent viscosity, and $\boldsymbol{D} = (\nabla\boldsymbol{v} + \nabla\boldsymbol{v}^T)/2$ the rate-of-deformation tensor. Indeed the viscosity is a function of the second invariant of the rate-of-deformation tensor $II_{\boldsymbol{D}} \equiv \sqrt{2\boldsymbol{D} : \boldsymbol{D}}$ which, in simple shear, becomes $II_{\boldsymbol{D}} = \dot{\gamma}$ [73]. For the constitutive equation $\eta(\dot{\gamma})$, we selected the Bird-Carreau model [74]:

$$\eta(\dot{\gamma}) = \eta_\infty + (\eta_0 - \eta_\infty)\frac{1}{[1 + (K\,II_{\boldsymbol{D}})^2]^{\frac{1-n}{2}}} \tag{2.22}$$

with parameters obtained by fitting the viscosity trends of the experimental fluids reported in Figure 3.2. The curves are superimposed to experimental data. The simulations are performed in a square-shaped microchannel of a 100 μm side (the same used for experiments of Section 4.2 and 4.3), with periodic boundary conditions between inflow and outflow, no-slip at the walls and by imposing the experimental flow rates at the inlet section.

Notice that velocity $V_{\mathrm{sim,z}}$ in Eq. (2.2) should be the particle velocity whereas the velocity $\boldsymbol{v}$ computed from Eqs. (2.20)-(2.22) is the fluid velocity, which is obtained in the absence of the particle. In confined systems, those two velocities are not exactly the same. In particular, in pressure-driven flows, the velocity of the fluid at the same location of the particle center is slightly higher than the particle velocity (it is conventionally stated that the particle *lags* the fluid). For the investigated confinement ratio, the discrepancies between those two velocities is quite small around the channel centreline [75] whereas it might become relevant for particles very close to the walls, i.e. for those particles belonging to the outermost bands. However, we recall that the aim of the procedure adopted to reconstruct the particle positions is that of assigning each particle to a specific band k. Thus, the most critical situation occurs for those particles lying close to the boundary between the fifth and sixth band for which an overestimation of the velocity will lead to an erroneous assignment of particles to the bands. However, those events are statistically irrelevant in all the cases considered in what follows, and hence particle distributions are never significantly altered.

Chapter 3

Rheolibrary

In this section we report the rheological characterisation of a wide class of fluids spacing from the liquids belonging to the so-called 'constant viscosity fluids' class to the much more complex cellulose solutions. Aim of this section is to introduce the reader to the polymers' solution rheological characteristics in order to have a possibly comprehensive overview of the viscoelastic fluids used in this work.

3.1 Poly Vynil Pyrrolidone (PVP)

Poly Vynil Pyrrolidone water solution could be taken as representative of the class of the elastic constant-viscosity fluids.
The PVP water solution 8% w/w was already used in literature to study particle migration in microchannels [10, 11, 13].

Figure 3.1 shows the rheology of the fluid. The viscosity is constant ($\eta = 0.09$ Pa·s) for about three decades of shear rate $\dot{\gamma}$. A very slight shear-thinning behaviour is observed for the largest shear rates. The frequency response measurements reported in Figure 3.1b highlight the viscoelastic character of the fluid, with a non-zero value of the storage modulus G'. The data shown in Figure 3.1b indicates the typical terminal behaviour of the moduli with the frequency, $G' \propto \omega^2$ and $G'' \propto \omega$, thus the PVP solution is

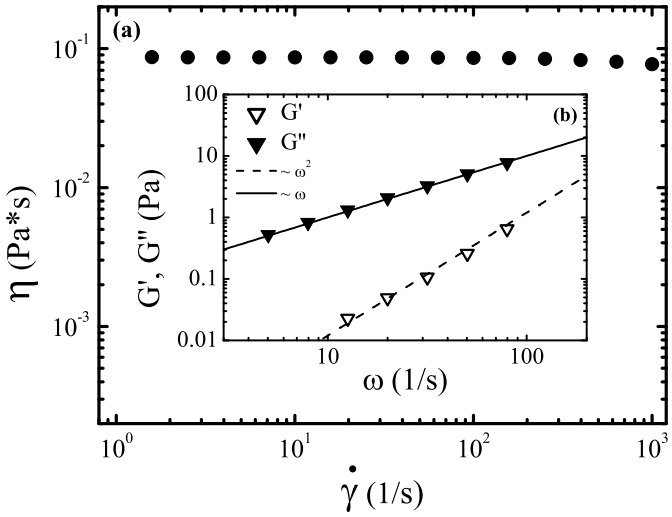

Figure 3.1: (a) Measured steady shear viscosity (black circles) for the aqueous 8% wt PVP solution. (b) Measured elastic modulus G' (white triangles) and loss modulus G'' (black triangles) for the aqueous 8% wt PVP solution. The slopes of the straight lines are 2 and 1 for G' and G'', respectively, and indicate the expected frequency dependence in the 'terminal region' of a viscoelastic fluid.

well-described by a Maxwell fluid [19] with a single relaxation time λ that can be obtained from the intersection of the slopes of the two moduli giving a value of $\lambda \sim 1.3 \cdot 10^{-3}$ s.

3.2 PolyEthylene Oxide (PEO)

Polyethylene Oxide is one of the most studied polymers due to its wide range of applications [76, 77]. In addition, it was recently used in several microparticle manipulation applications [13, 34, 37]. At low polymer concentration (dilute regime), PEO solutions exhibit a constant viscosity over several decades of $\dot{\gamma}$. By increasing the concentration, however, PEO solutions start to show a shear thinning behaviour [78], i.e. the viscosity does

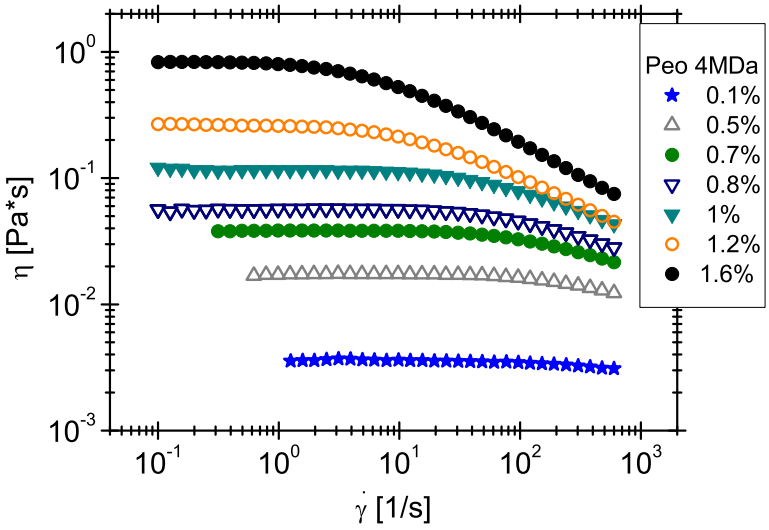

Figure 3.2: Measured steady shear viscosity for several concentration of PEO in Glycerol-water solution at 25% w/w.

depend on the shear rate. In particular, the viscosity of PEO solutions at relatively high concentration (semi-dilute and entangled regime) is a decreasing function of the shear rate $\dot{\gamma}$.

Figure 3.2 shows the rheology of different concentrations of PEO in Glycerol-water solution at 25% w/w. At $c = 0.1\%$ the solution viscosity is constant over three decades of $\dot{\gamma}$. When increasing the polymer concentration up to $c = 0.5\%$ the PEO solution exhibits a shear-thinning behaviour starting from $\dot{\gamma} \sim 100\ s^{-1}$. This behaviour is more and more pronounced when increasing the polymer concentration; in particular at $c = 1.6\%$ the shear-thinning zone starts from $\dot{\gamma} \sim 1\ s^{-1}$. This is due to the intermolecular interactions between polymer chains, that cause shear-thinning at lower shear rate values [19, 79].

It is possible to determine the polymer solution behaviours at different concentrations, i.e. the different polymer regimes, from the plot of the so-called *zero-shear* viscosity as a function of the concentration [19]. As a matter of fact, only for the polymers regime characterisation, we mainly use the specific viscosity η_{sp} defined as:

$$\eta_{sp} = \frac{\eta_0}{\eta_s} - 1 \tag{3.1}$$

where η_0 is the zero-shear viscosity of the polymer solution and η_s is the solvent viscosity.

The rheological behaviour of polymer solutions is strongly dependent on concentration and on the nature of the solvent [19, 80]. It has been theoretically predicted and experimentally demonstrated that the physico-chemical and rheological behaviour of a solution with flexible polymers drastically changes at some characteristic concentrations [80, 81]; of interest are the overlap concentration c^* and the entanglement concentration c_e. Such two quantities mark the transitions between different concentration regimes, from dilute to semidilute unentangled (through c^*) and to semidilute entangled (through c_e), by increasing polymer concentration.

Different scaling laws apply depending on the polymer solution's concentration regime [80]. These laws also contain important information about the 'quality' of the solvent for the dissolved polymer [80, 81, 82] through the *fractal polymer dimension* ν, that somehow quantifies the volume pervaded by a polymer coil within the liquid. A value of $\nu = 0.5$ identifies the so called *θ-solvent*, while $\nu = 0.6$ defines a *good solvent* [83].

The scaling law for η_{sp} as a function of concentration and fractal polymer dimension ν for Dilute, SemiDilute Unentangled and SemiDilute Entangled regime are respectively [80, 81]:

$$\eta_{sp,D} \propto c \qquad \eta_{sp,SDU} \propto c^{1/(3\nu-1)} \qquad \eta_{sp,SDE} \propto c^{3/(3\nu-1)} \tag{3.2}$$

with obvious meaning of the subscripts.

Regarding PEO solutions, the value for the ν coefficient is available from the literature. Tirtaatmadja *et al.* [82] took several experiments on PEO solutions, at different molecular weight, in water and glycerol-water mixtures, finding $\nu = 0.55$ in all cases, in good agreeement with the Polymer Handbook [84] and with other works [85, 86].

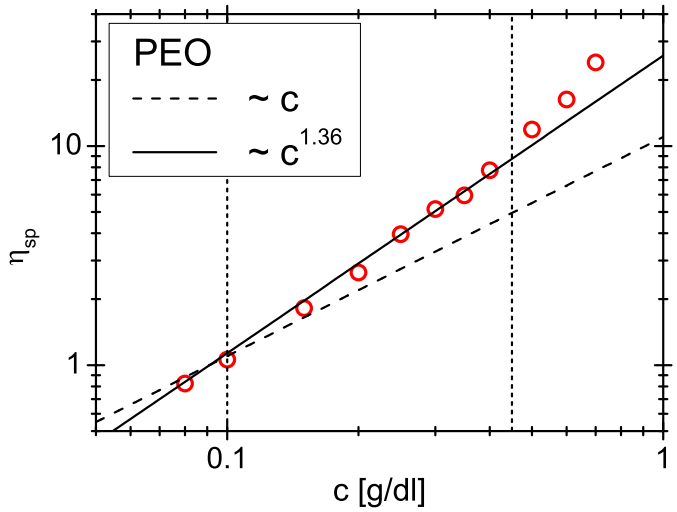

Figure 3.3: Plot of the specific viscosity as a function of concentration for PEO 4 MDa. Dashed and solid lines are the scaling law predictions for a neutral polymer with fractal dimension $\nu = 0.55$ in the dilute and semidilute unentangled regime, respectively. Error bars, estimated from the average of the zero-shear viscosity values in the rheology curves, are always smaller than the symbol size. Vertical black dashed lines are an estimate of the values of c^* (left) and c_e (right), respectively (see text).

Figure 3.3 shows the plot of the specific viscosity as a function of concentration for PEO solutions. Dashed line and solid line in Figure 3.3 are the theoretical predictions of the specific viscosity for a neutral polymer in good solvent, with $\nu = 0.55$. Dashed line refers to the dilute regime while solid one refers to the semidilute unentangled regime. With $\nu = 0.55$, the expressions for η_{sp} in those regimes are (from Eq. (3.2)):

$$\eta_{sp,D} \propto c \qquad \eta_{sp,SDU} \propto c^{1.36} \tag{3.3}$$

The curves given by Eq. (3.3) can of course be vertically shifted depending on prefactors, which however are not easily assessed from theoretical arguments. Thus, in order to properly identify the different regimes, i.e. the

vertical positions of the two curves, we proceed as follows. We fit different subsets of our complete data set with the available prediction of Eq. (3.3); we then choose the data subset with the highest number of data points that gives the coefficient of determination R^2 closest to the unity as the subset representative of a concentration regime. For example, we take the data subset ranging from 0.08 g/dl $< c <$ 0.8 g/dl and evaluate the R^2 imposing the equation $\eta_{sp,SDU} = A\, c^{1.36}$. We thereafter compare this R^2 value with the one obtained by choosing a narrower data subset, e.g. in the range 0.1 g/dl $< c <$ 0.6 g/dl, and choose the subset with the R^2 value closer to unity. By repeating this procedure, we arrive to the curves reported in Figure 3.3, thus identifying the dilute and semidilute unentangled regime. From Figure 3.3 it is now possible to estimate the value of the overlap concentration c^*, and also that of the entanglement concentration c_e: we find $c^*_{\mathrm{PEO}} \sim 0.1$ g/dl and $c_{\mathrm{e,PEO}} \sim 0.45$ g/dl. Indeed, when $c > 0.45$ g/dl, experimental data clearly start to deviate from the theoretical prediction for the semidilute unentangled regime, suggesting the transition to a new regime.

In Figure 3.4 the viscoelastic response of several PEO solutions is reported. At $c = 0.7\%$ the solution behaves like a Maxwell fluid with a single relaxation time λ given by the intersection of the two straight lines in the terminal region of G' and G''. When increasing the polymer concentration, a more pronounced deviation from the pure Maxwell model is observed. For example at $c = 1\%$ the solution follow the Maxwell model up to $\omega \sim 10\ rad/s$, after that it starts to deviate. This behaviour is enhanced at $c = 1.6\%$, in fact the terminal region finishes at $\omega \sim 1\ rad/s$; above $\omega \sim 1\ rad/s$ the solution deviates from the Maxwell fluid model. This behaviour is common in almost all the polymer solution in the semidilute entangled regime, i.e. above the entanglement concentration c_e [79]. The explanation of this deviation resides again in the intermolecular interaction between polymer chains; furthermore it is not possible to consider these fluids as Maxwell-like with a single λ, but they can be mathematically modelled as a modified Maxwell fluid with several relaxation times, or λ-spectra. Nevertheless, the intersection between

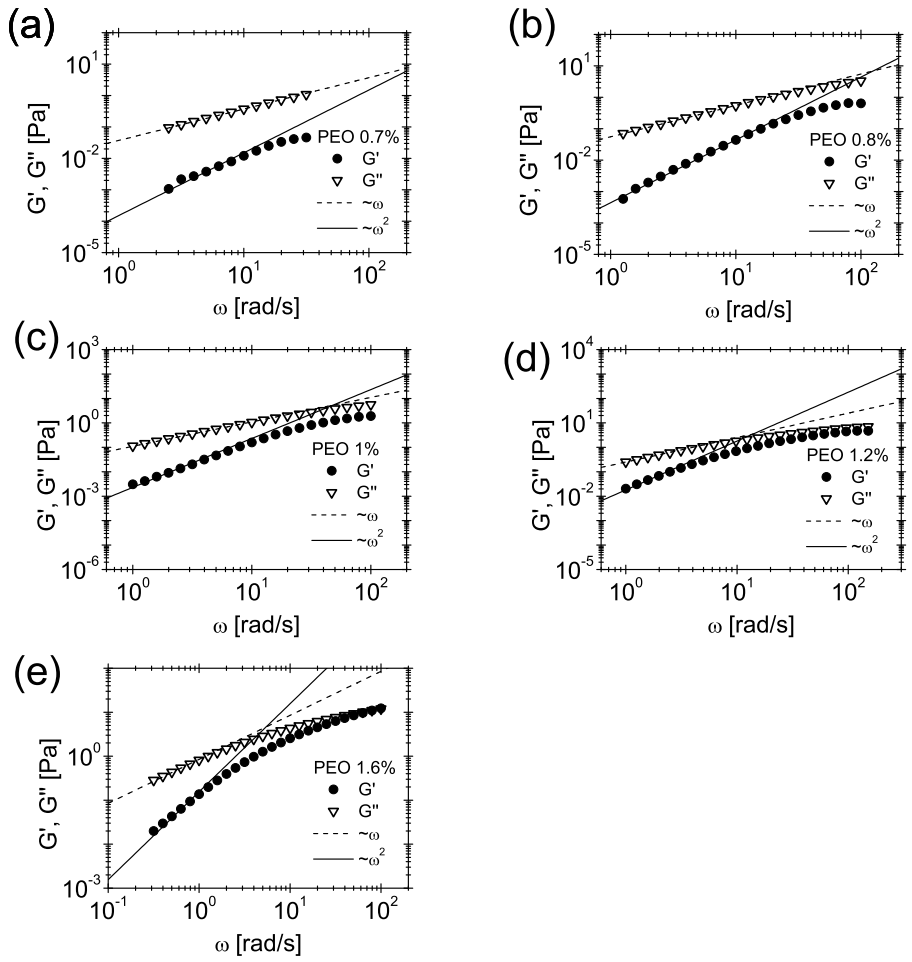

Figure 3.4: Measured elastic modulus G' (black circle) and loss modulus G'' (white triangles) for several concentration of PEO in Glycerol-water solution at 25% w/w. (a) $c = 0.7\%$. (b) $c = 0.8\%$. (c) $c = 1\%$. (d) $c = 1.2\%$. (e) $c = 1.6\%$. The slopes of the straight lines are 2 and 1 for G' and G'', respectively, and indicate the expected frequency dependence in the 'terminal region' of a viscoelastic fluid.

the straight lines of the Maxwell model gives the *longest* relaxation time, that will be used later to describe the dynamics of microparticles suspended in a non-Newtonian matrix subjected to pseudo-Poiseuille flow.

c [%]	λ [ms]
0.7	4
0.8	8
1.0	20
1.2	80
1.6	190

Table 3.1: Longest relaxation times at different PEO concentration. These values are evaluated by the intersection of the two straight lines in the 'terminal region' as for the Maxwell fluids model.

Table 3.1 reports the longest λ-value, evaluated by the intersection of the two straight lines in the 'terminal region' as for the Maxwell fluids model.

Finally, notice that λ-values at $c < 0.7\%$ are not detectable by conventional rheometer because of technological limitations. A novel method to evaluate fluid relaxation time values down to millisecond is presented in Section 5.1.

3.3 PolyAcrylAmide (PAM)

PolyAcrylamide solutions are widely used for several different applications ranging from biology [87, 88] to industry [89]. It is well known that strongly different rheological behaviours can show up, depending on the synthesis procedure, leading to the nomenclature of *ionic* and *non-ionic* PAM [90, 91, 92, 93]. In particular, non-ionic PAM behaves like a neutral flexible polymer; the ionic one, in contrast, behaves like a polyelectrolyte polymer as comprehensively reported in several works [87, 91].

We anticipate here that we used the non-ionic PAM for some applications described in Section 5 and the ionic PAM to validate the method to derive the relative viscosity by Optical Tweezers, previously described (See Section 2.8).

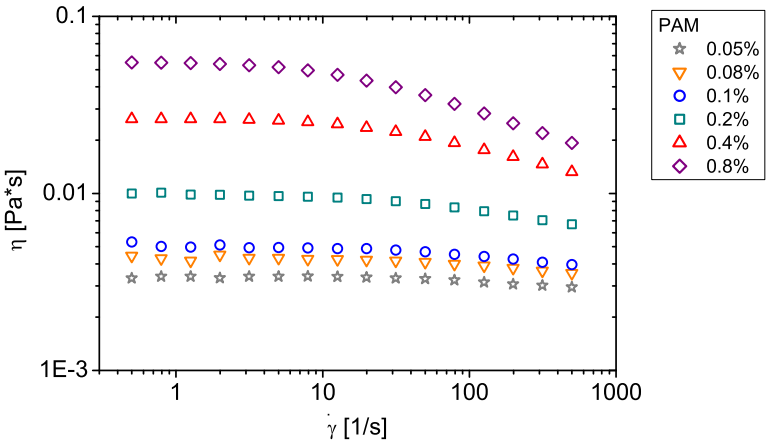

Figure 3.5: Measured steady shear viscosity for several concentration of PAM in Glycerol-water solution at 25% w/w.

non-ionic PolyAcrylAmide (niPAM)

The shear rheological behaviour of non-ionic PAM (niPAM) for several mass concentrations is reported in Figure 3.5.

At low polymer concentration niPAM solutions behave like a constant-viscosity fluid as for the PEO. By increasing the polymer concentration up to $c = 0.8\%$, it is possible to appreciate a weak shear-thinning behaviour starting from $\dot{\gamma} \sim 30\ s^{-1}$.

Figure 3.6 shows the specific viscosity η_{sp} of niPAM solutions, as a function of the concentration. Dashed line and solid line in Figure 3.6 are the theoretical predictions of the specific viscosity for a neutral polymer in good solvent, with $\nu = 0.585$. Dashed line refers to the dilute regime while solid one refers to the semidilute unentangled regime. With $\nu = 0.585$, the expressions for η_{sp} in those regimes are (from Eq. (3.2)):

$$\eta_{sp,D} \propto c \qquad \eta_{sp,SDU} \propto c^{1.32} \tag{3.4}$$

Also in this case, by following the same procedure previousy described, we determine the prefactors in Eq. (3.4) and then draw the dashed and the solid

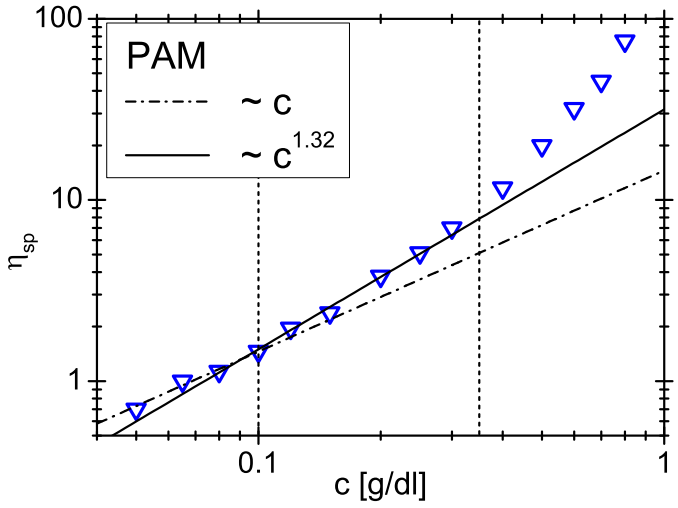

Figure 3.6: Plot of the specific viscosity as a function of concentration for PAM 5-6 MDa. Dashed and solid lines are the scaling law predictions for a neutral polymer with fractal dimension $\nu = 0.585$ in the dilute and semidilute unentangled regime, respectively. Error bars, estimated from the average of the zero-shear viscosity values in the rheology curves, are always smaller than the symbol size. Vertical black dashed lines are an estimate of the values of c^* (left) and c_e (right), respectively (see text).

lines in Figure 3.6. We estimate an overlapping concentration $c^*_{\mathrm{PAM}} \sim 0.1$ g/dl and an entanglement concentration $c_{\mathrm{e,PAM}} \sim 0.35$ g/dl.

Concerning the fluid viscoelasticity, information on the fluid relaxation time λ will be given later in the Section 5.1.

ionic PolyAcrylAmide (iPAM)

PolyAcrylamide in ionic form, iPAM, shows a different rheological behaviour respect to the non-ionic one as already reported in literature [92, 93].

Figure 3.7 shows the relative viscosity $\eta_r = \eta/\eta_s$ as a function of the mass concentration c for several ionic PAM solutions at two molecular weights (1500 Da and 1.145 MDa). Notice the really good agreement in Figure 3.7

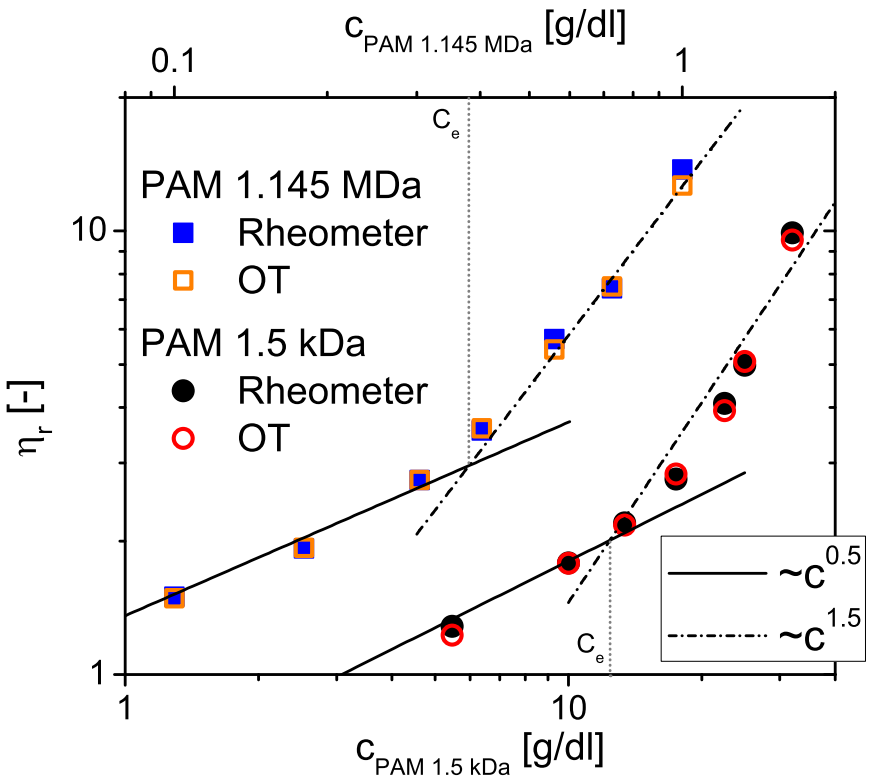

Figure 3.7: Comparison of the relative viscosity (respect to the water) as a function of concentration for ionic PAM 1.145 MDa and ionic PAM 1500 Da, by using Bulk rheology and Optical Tweezers . Solid and Dashed lines are the scaling law predictions for a polyelectrolyte with fractal dimension $\nu = 0.585$ in the semidilute and entangled regime, respectively.

between data measured by conventional rheometry and the ones by using Optical Tweezers coupled with the method described in section 2.8. Let us discuss the ionic PAM 1500 Da first. For this solution the chain length is quite small because of its small molecular weight (compared to PAM 1.145 MDa). It implies that in order to reach the overlapping and the entanglement concentration, high polymer concentrations are needed. That is why in Figure 3.7 we investigate mass concentration for ionic PAM 1500 Da up to $c = 32\ g/dl$. At mass concentration up to $c_e \sim 12\ g/dl$, the relative viscosity $\eta_r \propto c^{0.5}$; while for $c > c_e$, the relative viscosity $\eta_r \propto c^{1.5}$, both

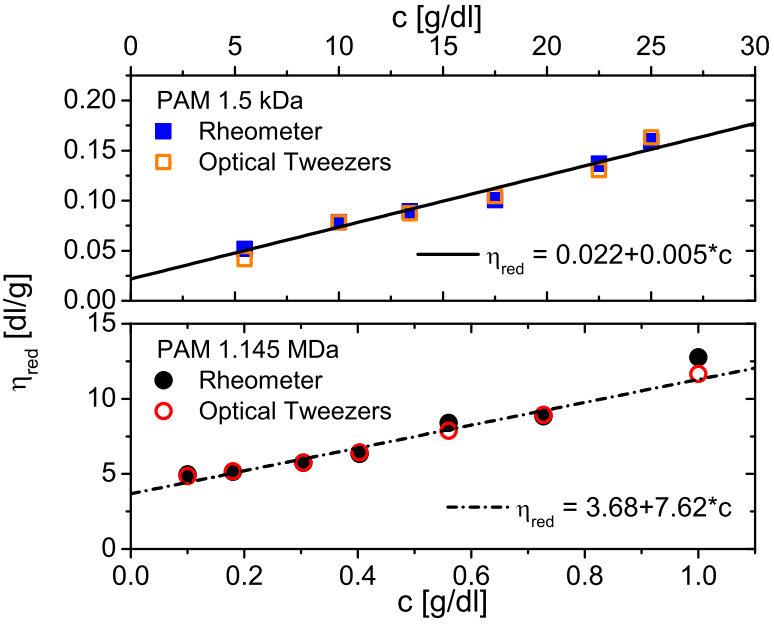

Figure 3.8: **Extrapolation of the intrinsic viscosity**. The reduced viscosity *vs.* concentration derived from the data shown in Figure 3.7. The lines are linear fits of OT data. The linear extrapolation of η_{red} to zero concentration provides a *reading* of the PAMs' intrinsic viscosities.

in good agreement with the theoretical prevision for polyelectrolyte solution in good solvent in the semidilute and the entanglement regime, respectively [80]. From Figure 3.7 it is possible to notice the same trend described above for the ionic PAM 1.145 MDa. The only difference resides inside the position of the entanglement concentration c_e due to the difference in the chain length. Regarding the ionic PAM 1.145 MDa, the entanglement concentration $c_e \sim 0.38\ g/dl$. It is also possible to plot the same data of Figure 3.7 in terms of the reduced viscosity $\eta_{red} = \eta_{Sp}/c$, as showed in Figure 3.8.

The extrapolation of η_{red} for $c \to 0$ gives the intrinsic viscosity $[\eta]$, that is used to estimate the polymer molecular weight by using the well known Mark Houwink relations (that depends on the polymer nature) [19]. Mark Houwink equations for the ionic PAM solution presented here can be written as [94]:

$$[\eta] = 6.31 \times 10^{-3} M^{0.80} \tag{3.5}$$

$$[\eta] = 4.90 \times 10^{-3} M^{0.80} \tag{3.6}$$

where the above two equations are valid for PAMs with low ($\lesssim 10^5\ Da$) and high ($\gtrsim 10^5\ Da$) molecular weights, respectively.

In Table 3.2 we report the results obtained by substituting the values of $[\eta]$ derived from Figure 3.8 in both Eqs (3.5) and (3.6) and compare them with the nominal values of the molecular weights provided by the supplier; the agreement is very good, especially when considering the respective range of validity of the two equations.

In order to give more details about the shear viscosity and the frequency response of a polyelectrolyte solutions, we report in Figure 3.9 the rheology of ionic PAM 1500 Da only at some chosen concentrations.

Figure 3.9a shows the comparison between shear rheology measured by conventional rheometry and frequency data derived by microrheology with Optical Tweezers. At lower mass concentration the viscosity is almost constant over four order of magnitude like for the constant-viscosity fluids. By increasing the concentration up to $c = 32\%$ the fluid exhibits a shear thinning behaviour from $\dot{\gamma} \sim 100 s^{-1}$. At low shear rate, instead, optical tweezers reveals an increasing of the viscosity when decreasing $\dot{\gamma}$. This behaviour can be related to some intermolecular interaction between polymer chains in the entangled regime; such interactions are destroyed when increasing $\dot{\gamma}$ because

$[\eta][g/dl]$	Equation	M [Da]	M[Da]
-	Nominal	1500	1145000
0.022 ± 0.008	Equation (3.5)	**1506**	906302
3.68 ± 0.24	Equation (3.6)	2066	**1240000**

Table 3.2: Comparison between nominal and measured molecular weights of two commercially available polyacrylamides.

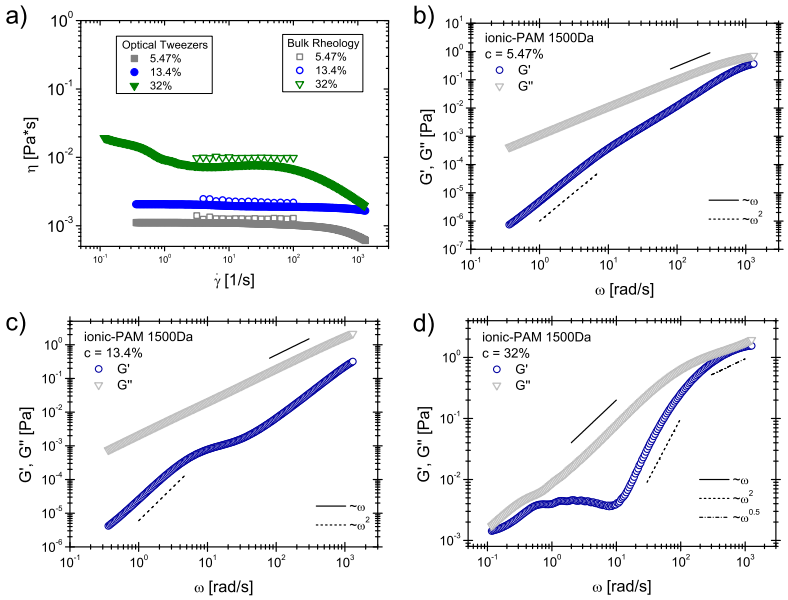

Figure 3.9: (a) Comparison between bulk (open symbols) and microrheology (closed symbols) measurements of the shear and complex viscosity, respectively, of ionic PAM 1500 Da at several concentrations. (b-d) Measured elastic modulus G' (blue circle) and loss modulus G'' (grey triangles) for several concentration of ionic PAM 1500 Da water at (b) $c = 5.47\%$. (c) $c = 13.4\%$. (d) $c = 32\%$. Straight and dashed lines are the theoretical prevision for polyelectrolyte polymers in good solvent.

of the fast shearing process. Figure 3.9(b-d) show the frequency response of ionic PAM at some mass concentrations. In semidilute regime at low frequencies, G' and G'' follow the well known scaling law for the Maxwell fluid [19]. In addition, in the entangled regime the solutions behaves like a Maxwell fluid at low frequencies and deviate from that at high frequencies, in fact from $\omega \sim 100\ rad/s$ we find $G', G'' \propto \omega^{0.5}$, as theoretically predicted [80].

3.4 HydroxyEthyl Cellulose (HEC)

Cellulose is the most abundant material on earth [95]. In particular, HydroxyEthylCellulose (HEC) is obtained by reacting ethylene oxide with wood-based cellulose [96]. Due to its water solubility, HEC is widely used as thickening agent in several industrial applications such as paints [97], textile [98] and in many biomedical applications such as membrane preparation [99], pharmaceutical applications [100], drug delivery [101] and tissue engineering [102]. Hence the general interest in the rheological properties of HEC solutions [96, 102, 103, 104]. Previous rheological measurements [96] showed that, at relatively high flow rates, all the investigated HECs solutions manifest a shear thinning behaviour; this was confirmed by further studies [103]. In addition, it is well known that cellulose contains nanofibers with high degree of crystallinity [105, 106, 107]. In particular, HEC nanofibers in solution behave like semi-flexible rods and that the nanofibers interact each other by hydrogen bonds and/or Van der Waals interactions [106], forming mesoscopic structures and/or local networks. A further evidence of the existence of elongated supramolecular structures in HEC water solutions was provided by Arfin and Bohidar [107] *via* transmission electron microscopy (TEM) images. Here we report the rheological characterisation of the HEC through Bulk rheology measurement, i.e. by using conventional rheometers, and microrheological measurements by using Optical Tweezers.

In Figure 3.10 the comparison between viscosity curves (open symbols) obtained from bulk rheology measurements and complex viscosity (filled symbols) obtained by Optical Tweezers of HEC solutions at concentrations ranging from 0.05% to 0.8% w/w are reported. The results indicate that for $c < 0.2\%$ all the solutions have an almost constant viscosity value for shear rate ($\dot{\gamma}$). For $c > 0.2\%$, in contrast, at high shear rates, the solutions exhibit a weak shear thinning behaviour [96, 103, 104], as shown in Figure 3.10.

In addition, we appeal to the empirical Cox-Merz rule [108], which allows comparison between linear and non-linear rheology measurements; as reported in Figure 3.10. Quantitative agreement between micro- and bulk-

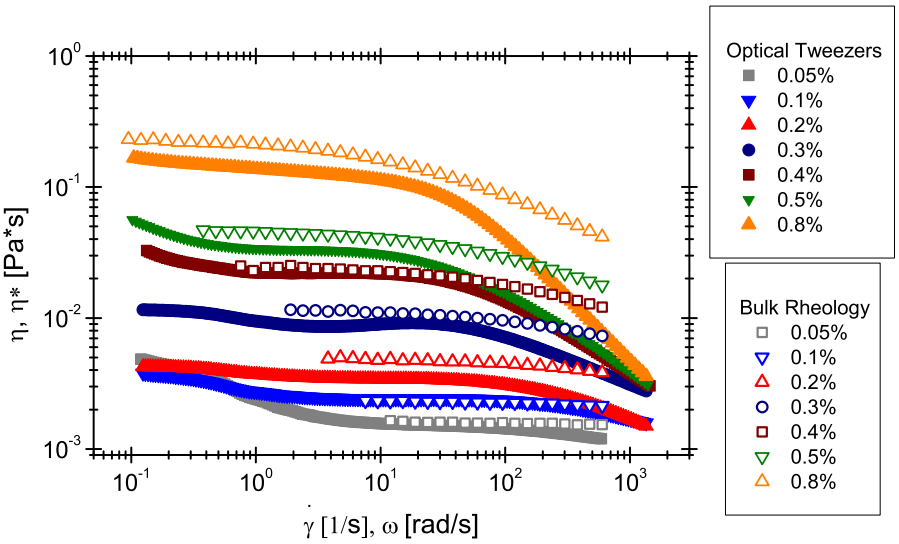

Figure 3.10: Comparison between bulk (open symbols) and microrheology (closed symbols) measurements of the shear and complex viscosity, respectively, of HEC at several concentrations.

rheology is apparent.

In Figure 3.11 we report the plateau value of the viscosity as a function of the HEC concentration for both the adopted methods of investigation. At low concentrations (i.e. for $c < 0.2\%\ w/w$) the viscosity scales with the concentration as $\eta \propto c^{0.5}$; whereas, at HEC concentrations $c > 0.2\%\ w/w$, the viscosity scales with the concentration as $\eta \propto c^3$. These scaling laws are typical of rod-like polymer solutions [109, 110, 111, 112] moving from a dilute to an entangled regime, respectively. Notably, these results are in agreement with the transmission electron microscopy images reported by Arfin and Bohidar [107] that show the existence of rod-like structures due to the HEC nanofibers interaction. In order to assess the presence of complex structures in our system, we carried out dry atomic force microscopy images, reported as insets in Figure 3.10. For $c > 0.2\%$, we found rod-like structures similar to those found by Arfin and Bohidar [107]. We report, as an example, in the insets the AFM images for $c = 0.05\%$ and $c = 1\%$. Rod-like structures

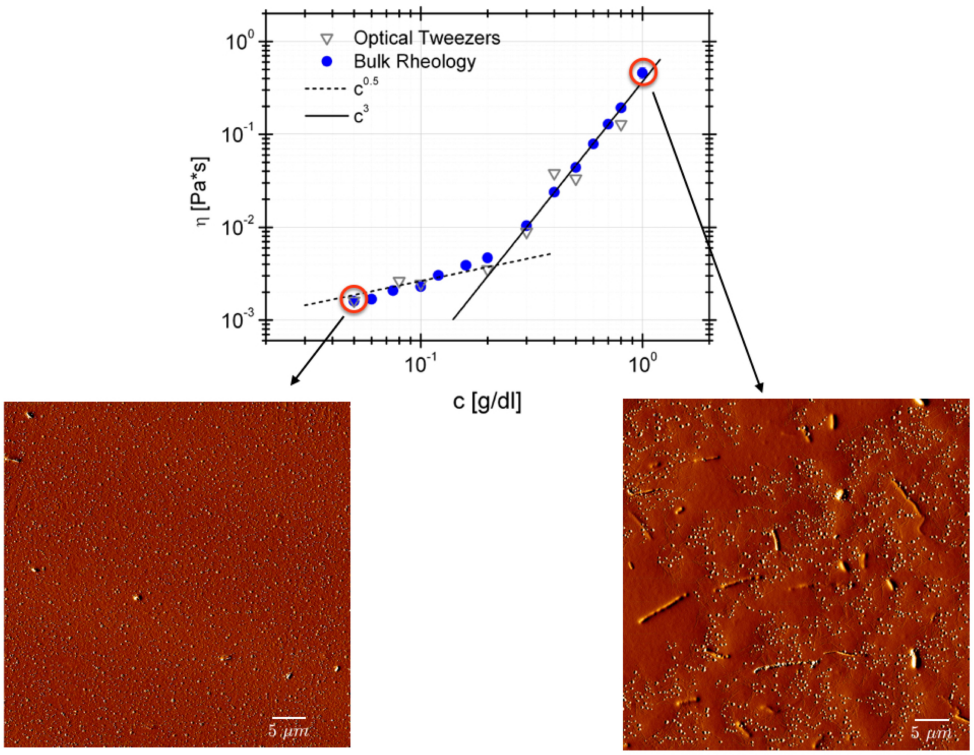

Figure 3.11: Comparison between micro- and bulk-rheology measurements of the viscosity concentration scaling laws obtained from the measurements shown in Figure 3.10. Insets are AFM images of HEC solution at $c = 0.05\%$ (left side) and $c = 1\%$ (right side). The scale bar is reported in white with $L_{scale} = 5\mu m$.

are present only in the concentrated regime; in fact, several measurements taken at concentration lower than $c = 0.2\%$ did not reveal the existence of any meso-structures like those observed in the entangled regime. Finally, it is worthy to highlight that the value of the overlapping concentration, measured at the transition between the above mentioned regimes, i.e. $c^* \cong 0.22\%\ w/w$, is in good agreement with those found in literature of $c^* \cong 0.2\%\ w/w$ [107, 113, 114].

Some microrheology results have been already shown in Figure 3.10 in terms of the fluids' complex viscosity $|\eta^*(\omega)| = G^*(\omega)/\omega$, and a good agree-

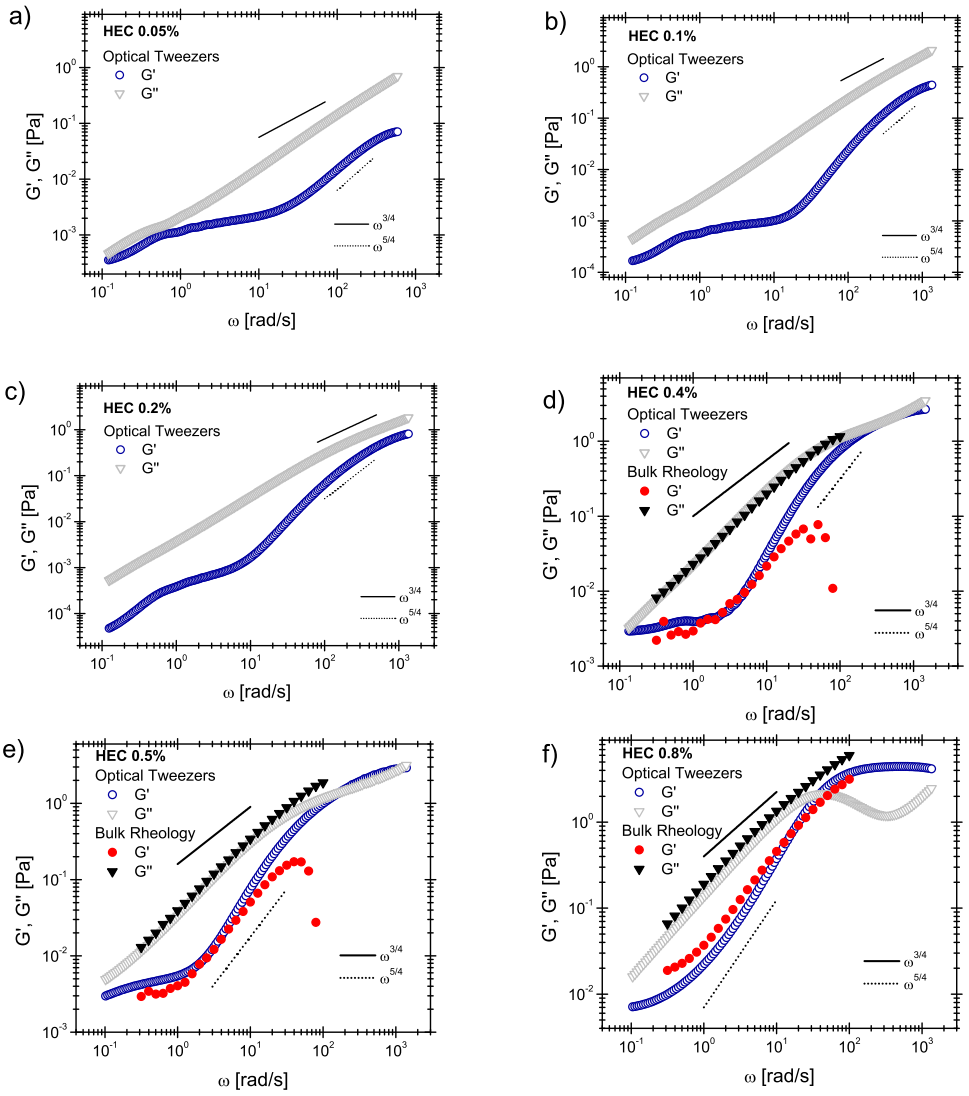

Figure 3.12: Comparison between the HEC solutions' linear viscoelastic moduli *versus* frequency measured with both a conventional rotational rheometer (filled symbols) and with optical tweezers (open symbols) for HEC concentrations: a) 0.05%, b) 0.08%, c) 0.1%, d) 0.2%, e) 0.3%, f) 0.4%, g) 0.5%, h) 0.8%w/w.

ment with the bulk rheology measurements has been found for all the explored HEC concentrations. We proceed now to compare the micro- and the bulk-linear rheology measurements, in terms of storage modulus G' and viscous modulus G'', performed on water based solutions of HEC at different concentrations as shown in Figure 3.12. At very low concentration the rheometer is not able to detect the low elasticity of the samples, while optical tweezers do, as also reported by Pommella *et al.* [91]. Different is the story for the solutions at relatively high HEC concentrations, where both the moduli are measurable by both the techniques and they are in remarkable agreement. Moreover, the results shown in Figure 3.12 are also in good agreement with the theoretical predictions for the linear viscoelastic response of rod-like polymer solutions [115]. In particular, in Figure 3.12 it is possible to identify the characteristic frequency scaling laws of the moduli, predicted for instance by Morse [116, 117, 118] and Shankar *et al.* [115], for rod-like polymers solutions: i.e. $\omega^{5/4}$ and $\omega^{3/4}$.

Chapter 4

Particle Migration in Viscoelastic Liquids

As anticipated in Chapter 1, particles suspended in viscoelastic fluids and subjected to shear or Poiseuille flow, are pushed towards several equilibrium positions in dependence on the fluid rheology [10, 12, 119, 120, 121]. In this section we report the effect of fluid rheology on particle migration in a square-shaped microchannel. We will use the viscoelastic fluids previously described. Aim of this section is to give an overview of the migration phenomenon and its entity, under qualitative and quantitative arguments.

4.1 Particle Migration in Elastic Constant-Viscosity Fluids

We proceed now to study the particle migration dynamic for particle suspended in PVP 8%, i.e. a constant-viscosity fluid as described in Section 3.1, in two different PMMA square-shaped microchannels (see Chapter 2 for fabrication details). The channel schematisation together with the channel cross section division in bands (see Section 2.6 for details) is reported in Figure 4.1

In order to study the effect of the entrance, two differently shaped entrances at the channel ends are made. The first entrance (triangular shape

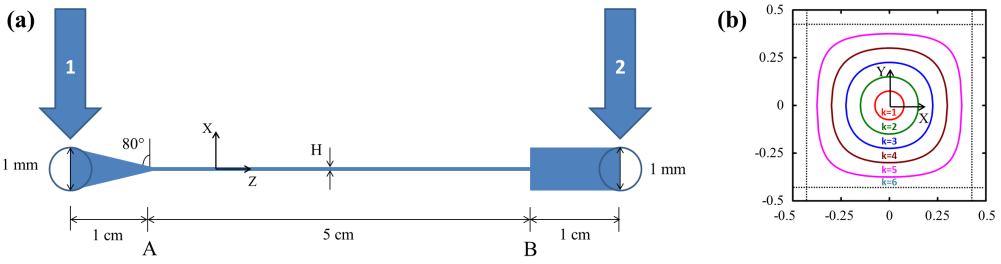

Figure 4.1: (a) Schematic representation of the channel used in the experiments. A smooth (indicated by the arrow number 1) and an abrupt (indicated by the number 2) entrances at the channel ends are fabricated in order to study entrance effects on the particle distributions. In the figure, the relevant dimensions are reported. (Dimensions along X and Z are not in scale.) (b) Concentric bands dividing the channel cross-section used to compute the particle distributions. X and Y are the dimensionless coordinates of the channel cross-section. The dashed lines delimit the region accessible to the particles. The bands are progressively numbered from the inner one ($k = 1$) to the outer one ($k = 6$). Notice that the first band has almost the same dimension of the particle.

from the top view, left side of Figure 4.1a) is designed in such a way to assure a smooth velocity field from the inlet to the main channel. The second entrance (rectangular shape from the top view, right side of Figure 4.1a) is designed to study the effect of an abrupt contraction on the particle distribution. As sketched in Figure 4.1a, the inlet/outlet holes are positioned at the end of the diverging sections, hence far from the main channel, avoiding clogging. In what follows, we refer to the first entrance as *smooth* and to the second one as *abrupt*.

The relevant dimensions of the device are shown in Figure 4.1a. Two dimensions for the side of the channel cross-section H are considered (50 μm and 100 μm). In the 50 μm channel the suspension with particle diameter 5.8 μm is made to flow, whereas a suspension of particles with diameter $D_\mathrm{p} =$ 10 μm is pumped through the 100 μm channel. In this way, the confinement

ratio $\beta = D_p/H$ is about 0.1 for both systems.

First, we study the particle migration in the 50 μm channel ($El = 49$). In Figure 4.2a, the particle fractions in the six bands at 4 cm from the inlet of the channel for a smooth entrance are reported, for different Deborah numbers. For $De = 0.0045$, the particles are uniformly distributed within almost the whole cross-section, as expected. Indeed, at such a low Deborah number, the fluid is essentially Newtonian. Only the external band ($k = 6$) is empty of particles, likely due to some migration that, although weakly, is taking place.

At $De = 0.012$ we observe a particle depletion from the two external bands due to an increased viscoelastic effects, although the particles are still randomly distributed within the rest of the channel section. Starting from $De = 0.061$, a peak corresponding to the inner band appears and grows as the Deborah number increases. For the highest flow rate, corresponding to $De = 0.18$, we found that about 84% of particles are enclosed within the circle around the channel centreline.

In Figure 4.2b and 4.2c, the particle positions over the channel cross-section are reported. Each point in the figures, generated by the position reconstruction procedure described previously (see Chapter 2), represents the coordinates of a particle center. The data are denoted by different colors according the bands they belong to. At $De = 0.0045$ (Figure 4.2b), the particles are randomly distributed along the whole cross-section, in agreement with the black bars of Figure 4.2a. At $De = 0.18$, the most of the points are included in the first band reflecting the quantitative behaviour of the purple bars in Figure 4.2a. Particles are also present in the second band (green symbols). Notice that the number of the green circles is about one-half of the red ones; nevertheless, the height of the bar corresponding to the second band is much lower than the height of the first one. In this regard, we recall that, in the calculation of the particle fractions through Eq. (2.1), the number of particles n_k is normalised by the area of the band that is quite large for the green data as compared to the red ones. On the other hand,

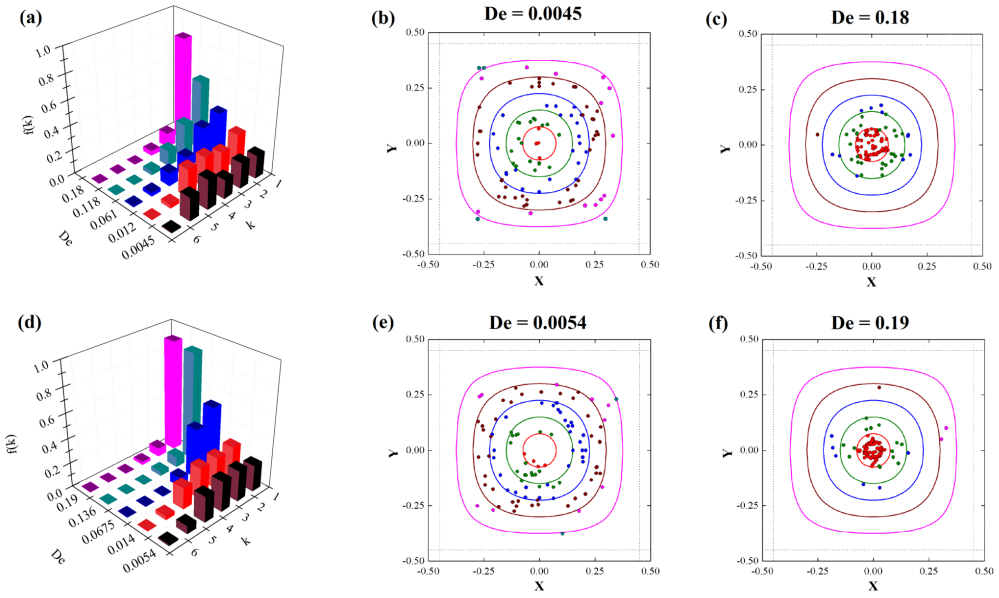

Figure 4.2: Experimental results for the 50 μm channel (Elasticity number $El = 49$). (a) Fractions of particles in the different band k measured at 4 cm from the inlet, for a smooth entrance, as a function of De. (b) Particle positions on the square cross-section for the smooth inlet at $De = 0.0045$. The symbols denote the position of the particle centers and are colored according the band they belong to. See Figure 5.3 for the meaning of the solid and dashed lines. (c) Particle positions as in (b), at $De = 0.18$. (d) Fractions of particles in the different band k measured at 4 cm from the inlet, for an abrupt entrance, as a function of De. (e) Particle positions as in (b), for an abrupt entrance at $De = 0.0055$. (f) Particle positions as in (b), for an abrupt entrance at $De = 0.2$.

the average velocities of the two bands, $\overline{v}_1$ and $\overline{v}_2$, are comparable, and only slightly affect the particle fractions. Much less particles are found in the third band that is almost absent in terms of particle fractions. In conclusion, the data shown in Figs. 4.2a and 4.2c clearly demonstrate the possibility to align particles on a single streamline (the channel axis) in a square-shaped channel by exploiting purely viscoelastic effects, i.e. a 3D purely viscoelastic

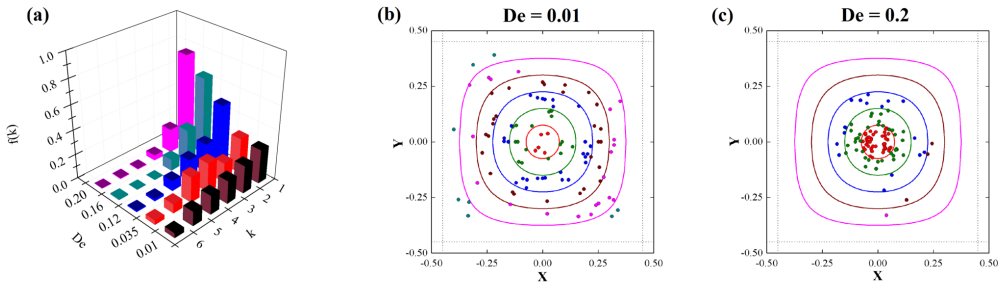

Figure 4.3: Experimental results for the 100μm channel (Elasticity number $El = 12$). (a) Fractions of particles in the different band k measured at 4 cm from the smooth inlet as a function of De. (b) Particle positions on the square cross-section for the smooth inlet at $De = 0.01$. (c) Particle positions on the square cross-section for the smooth inlet at $De = 0.2$. In (b) and (c), the same colouring of symbols as in Figure 4.2 is adopted.

focusing is here achieved for the first time in a square-shaped geometry. The required focusing length decreases with the Deborah number, as reported in the previous literature for different channel geometries [10, 11, 61].

The data shown above refer to a smooth entrance (left side of Figure 5.3a) that assures an uniform particle distribution over the inlet channel section, as confirmed by movies taken upstream the converging section. A non-uniform distribution may occur by modifying the shape of the region between the feed and the square-shaped microchannel. An effect of the entrance has been already noted in cylindrical channels where the contraction generated by two concentric pipes leads to a non-uniform inlet distribution [61].

To explore the entrance effect on the particle focusing, we feed the suspension from the side 2 shown in Figure 4.1a. The abrupt contraction has a large aspect ratio (20:1). The experimental results are reported in Figures 4.2(d-f). A similar qualitative behaviour as for the smooth entrance is found. However, the particle distributions are quantitatively different. By looking at the $De = 0.0054$ case, we clearly observe that the fifth bar is lower for the abrupt entrance as compared to the $De = 0.0045$ case of Figure 4.2a.

This is also confirmed by comparing the particle positions in Figures 4.2e and 4.2b: a lower number of particles is present in the fifth band (purple circles) and most of them are already on the boundaries of the fourth band. By increasing the Deborah number, it is observed that the same fraction of particles in the inner circle obtained for a smooth entrance at $De = 0.18$ (the highest purple bar in Figure. 4.2a) can be achieved at a lower Deborah number for an abrupt contraction ($De = 0.136$, the highest green bar in Figure 4.2d). Equivalently, for a fixed Deborah number, an abrupt inlet contraction requires a shorter channel length, as compared to a smooth entrance, to achieve 3D particle focusing. The higher focusing efficiency is readily observed from the data in Figure 4.2f where the most of the particles have the center within the inner band (compare with Figure 4.2c). A possible explanation for the observed *entrance effect* could be the existence of high normal stress regions around the corners of the abrupt contraction [122] that push the particles away from the corners, leading to a free-particle depletion layer along the channel walls.

Finally, we investigate the effect of the channel dimension on the particle focusing. In Figures 4.3a, 4.3b, 4.3c, the particle distributions and the positions on the channel section are reported for a channel with side length $H = 100$ μm. The confinement ratio $\beta = D_\mathrm{p}/H = 0.1$ is essentially the same as in the previous case. However, the Elasticity number is 4 times lower ($El = 12$). The analysis of the distributions show a similar qualitative behaviour as for the 50 μm channel, supporting a fair scalability of the 3D viscoelastic focusing. The similar trends for both channel size also confirm that the value of the Elasticity number $El = 12$ (large channel) is still sufficiently high, assuring the predominance of the viscoelastic forces over the inertial ones.

By further increasing the channel dimension, the Elasticity number decreases and inertia should start to play a role, reducing the efficiency of the elastic focusing (inertial forces push the particles away from the center [16]). In the opposite situation of smaller channel and particle dimensions, thermal

fluctuations become important, and should again lead to a dispersion of the particles over the channel section [123].

4.2 Particle Migration in Shear-thinning Fluids

In order to study particle migration in shear-thinning liquids, we adopted the PEO 4MDa in Glycerol-water solution 25% w/w at several mass concentrations, as a representative suspending medium. Experiments were carried out in a PMMA square-shaped microchannels (see Chapter 2 for fabrication details) with $H = 100\ \mu m$. The channel schematisation together with its relevant dimensions are reported in Figure 4.4.

We present the experimental results for the PEO suspending fluid at the concentration of 0.8% wt first. As shown in Fig. 3.2, the fluid viscosity is essentially constant with the shear rate up to $\dot{\gamma} \sim 30\ s^{-1}$. In the range of flow

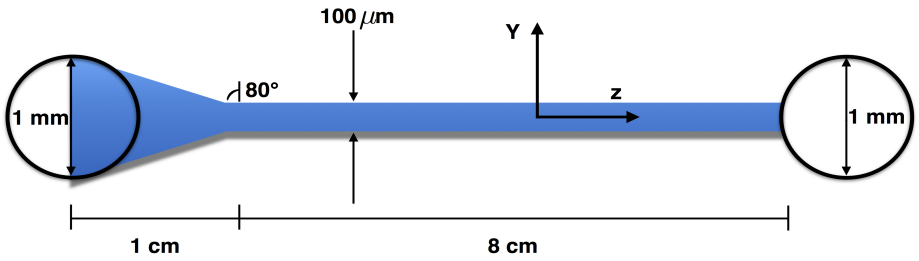

Figure 4.4: Schematic representation of the channel used in the experiments. A smooth entrance at the channel ends are fabricated in order to guarantee an uniform particle distributions. In the figure, the relevant dimensions are reported. The dimensions along Y and Z are not in scale.

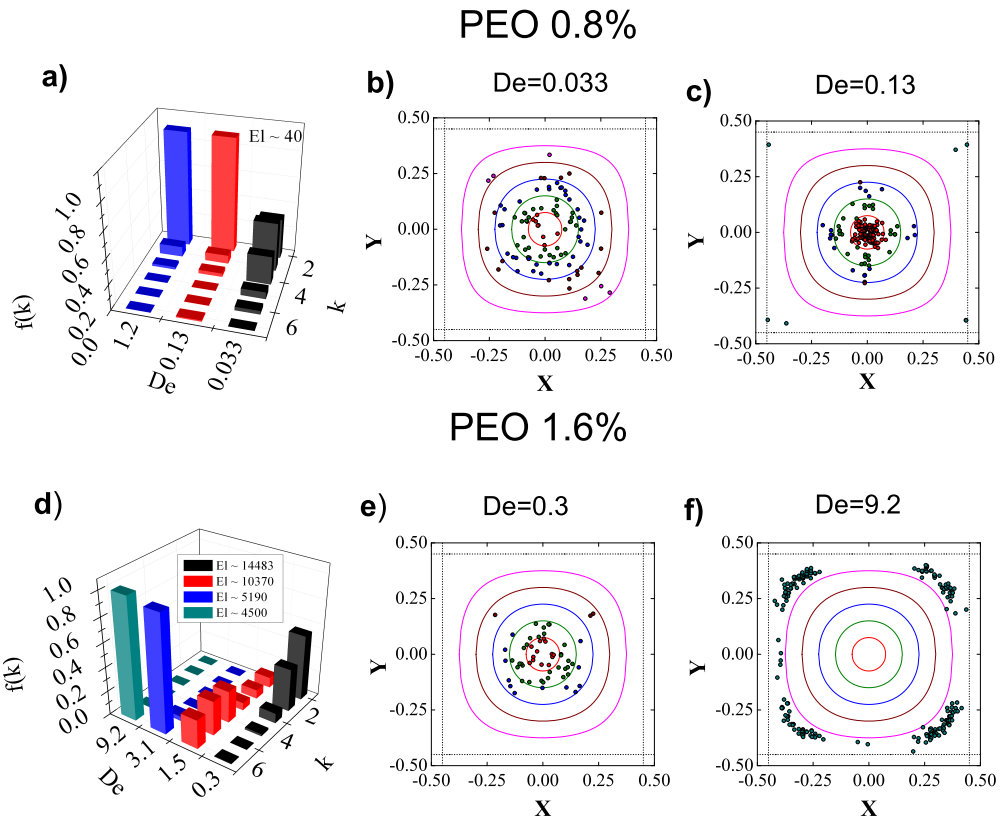

Figure 4.5: Experimental results for PEO 0.8%(a-c) wt and PEO 1.6% wt(d-f). (a) Fractions of particles in the different band k measured at 8 cm from the inlet as a function of De. (b) Particle positions on the square cross-section at $De = 0.033$. The symbols denote the position of the particle centers and are colored according the band they belong to.(c) Particle positions as in (b), at $De = 0.13$. (d) Fractions of particles in the different band k measured at 8 cm from the inlet as a function of De. (e) Particle positions as in (b) at $De = 0.3$. (f) Particle positions as in (b), at $De = 9.2$.

rates investigated for this liquid, the Elasticity number is constant as well. For this set of experiments, we evaluate $El \sim 40$, i.e. the fluid elasticity is expected to be dominant with respect to inertia. We therefore expect results similar to those presented in the previous section.

Figure 4.5a reports the fraction of particles in the bands for three different

Deborah numbers, whereas Figures. 4.5b and 4.5c show the reconstruction of the particle positions over the channel cross-section for the minimum and maximum values of the Deborah number. It is readily observed that, at $De = 0.033$, viscoelastic effects are present but weak: the particles tend to still migrate towards the channel centreline but, at 8 cm from the inlet, they are distributed between the bands $k = 1$ and $k = 3$. By Increasing De, viscoelastic forces become stronger and the most of the particles are more focused in the innermost band. From this first set of experimental results it clearly appears that particles suspended in a fluid with constant viscosity under elasticity-dominant conditions are subjected to a migration force towards the channel centreline. In the above presented data, we reported results on particle migration when exploring the constant viscosity-region of the suspending fluid. Now we proceed to show the data on particle migration when exploring the constant viscosity and the thinning region. To this aim, we report in Figure 4.5d, the migration of particles suspended in the high concentration PEO 1.6%. Due to the high viscoelasticity of the solution ($\lambda \sim 0.18$ s), the Deborah number is relatively high even at low flow rates. At the lowest Deborah number here considered ($De = 0.3$), the viscosity is equal to the zero-shear one; at the highest De number ($De = 9.2$) instead, the viscosity is $\sim 1/4$ of its zero-shear value (see Figure 3.2). In short, except for the lowest De, the fluid is always in the shear-thinning region of the flow curve for all the examined flow rates. As a consequence, the Elasticity number will be changing with the flow rate in the experiments. Notice, however, that the smallest Elasticity number is $El \sim 4500$ (corresponding to $De = 9.2$), i.e., for the PEO 1.6% suspending fluid, inertial effects are always definitely irrelevant. From Figures. 4.5a-4.5c, a qualitative difference from the previous case is observed. At the lowest Deborah number ($De = 0.3$) particles still migrate towards the centreline in agreement with the previous cases. The presence of the shear thinning, however, does influence the migration phenomenon, because only around 60% of the particles are focused in the centreline (see Figure 4.5b), in contrast with higher percentage values

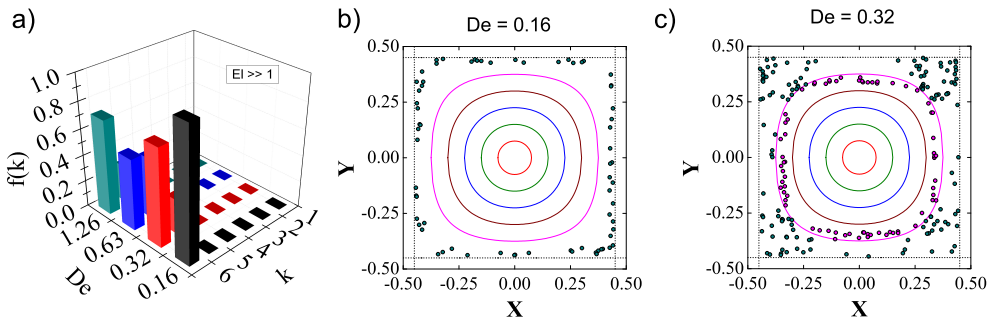

Figure 4.6: Experimental results for HEC 1% wt. (a) Fractions of particles in the different band k measured at 8 cm from the inlet of the microchannel with $H = 100\mu m$, as a function of De. (b) Particle positions as in (b) at $De = 0.0158$. (f) Particle positions as in (b), at $De = 0.316$.

found before. Notice, however, that all the particles are located between the first two bands, somehow confirming the previous results pertaining to lower values of λ. By increasing the Deborah number for the PEO 1.6%, a different scenario takes place as apparent in Figure 4.5: the particles now do not migrate towards the channel centreline, but towards the corners. At $De = 9.2$, all the particles belong to the outermost band and are positioned at the corners only (see Figure 4.5c). Apparently, also the particles initially located around the channel centreline have been driven outwardly towards the channel corners.

We proceed now to describe migration of particles suspended in HEC water solutions. As already mentioned before, HEC is a shear thinning fluid that, in the entangled regime, shows the formation of supramolecular structures (see insets in Figure 3.11) due to the interactions between polymer chains.

We therefore report in Figure 4.6a the fraction of particles in the bands for fours different Deborah numbers and in Figure 4.6(b-c) the reconstruction of the particle positions. Here we expect to see the same qualitative behaviour encountered for PEO 1.6%. Particles suspended in HEC 1%, migrate always

towards the channel walls in the range of examined De. As a difference with PEO 1.6%, at $De = 0.158$ particles migrate towards the whole band $k = 6$. When increasing the De by a factor 2, particles migrate towards the four corners and also towards the corners of the fifth band. This behaviour is, strictly speaking, different from the one showed in Figure 4.5f and it could be ascribed to the presence of supramolecular structures with a length comparable to the particle size. It could imply, in fact, a wide depletion layer closed to the channel walls that affects the migration phenomenon. Nevertheless a more deeper investigation is necessary in order to fully clarify these results.

At the end of this section, we want to highlight that the motion towards the channel corners reported in the present paper, occurring at high De for shear-thinning fluids, agrees with recent 3D finite element simulations where the motion of a single spherical particle suspended in liquids modelled through several constitutive equations and flowing in a square-shaped microchannel under inertialess conditions is investigated [12]. In that work, for fluids with a zero second normal stress difference (for which secondary flows are absent), the numerical predictions show that the particle migrates towards the channel centreline or the corners depending on its initial position. The two migration directions are separated by a closed curve. The position of such a curve strongly depends on the constitutive and flow parameters and, in particular, on the entity of the shear-thinning. For strongly shear-thinning fluids and high De, the separatrix approaches the channel centreline and wall attraction results.

4.3 Effect of Inertia and Elasticity on Particle Migration

In this section we investigate the co-occurring effect of inertia and elasticity on particle migration by selecting the PEO 0.1% wt as suspending liquid (Figure 4.7(a-c)) . Same results apply for HEC 0.05% (Figure 4.7(d-f)).

For PEO 0.1%, indeed, we found that the Elasticity number $El \sim 0.6$, which would mean that inertial and viscoelastic forces are comparable. Experiments were carried out in the same square-shaped microchannel with $H = 100\ \mu m$ of Figure 4.4.

From the data shown in Figure 4.7a, however, we observe a qualitatively similar situation as the PEO 0.8% wt case (see Figure 4.5(a-c)): at low Deborah numbers, the particles are essentially randomly distributed between the bands $k = 1$ and $k = 5$ and only the outermost band is empty; as the Deborah number increases, more and more particles move towards the innermost band. For the highest flow rate considered, the most of the particles are confined in the inner two bands and only few of them still belong to the third one. Notice that no particle is anyway found at some equilibrium position between the channel centreline and the walls, or in the corners. It so appears that, even for an Elasticity number around unity, the focusing mechanism induced by the fluid viscoelasticity dominates being essentially unaffected by inertial effects. In other words, even when the Reynolds number becomes comparable with the Deborah number, the effective migration force acting on the particles stays always directed towards the centreline, regardless of the initial particle position, similarly to the purely viscoelastic case. In conclusion we found that inertia is negligible with respect to elasticity on the focusing mechanism. By varying the Elasticity number over almost two order of magnitude, from $El \sim 0.6$ (PEO 0.1%) to $El \sim 40$ (PEO 0.8%), no qualitative change in the final particle position (the centreline) is observed, suggesting that the migration induced by viscoelasticity is, as a matter of fact, the only relevant mechanism for elastic, constant-viscosity fluids. In this regard, we mention recent experiments by Choi *et al.* [30] on particle migration induced by inertial effects in Newtonian fluids flowing in square-shaped microchannel. They have found that particles confined in a channel with $\beta \sim 0.1$ experience a very limited migration across the streamline within 10 cm of channel length even at $Re \sim 7$. Only by increasing the Reynolds number up to $Re \sim 50$, a transversal motion towards four attractors located

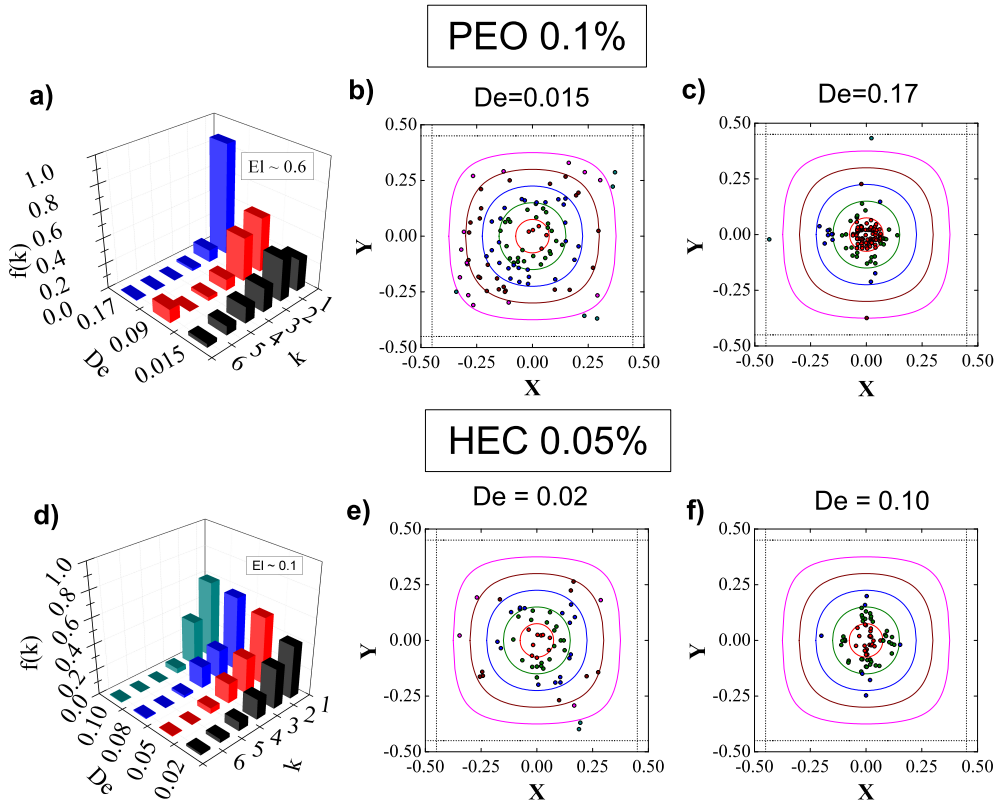

Figure 4.7: Experimental results for PEO 0.1% and HEC 0.05%. (a) Fractions of particles in the different band k measured at 8 cm from the inlet of the channel with $H = 100\mu m$ as a function of De for PEO 0.1%. (b) Particle positions on the square cross-section at $De = 0.015$. The symbols denote the position of the particle centers and are colored according the band they belong to.(c) Particle positions as in (b), at $De = 0.17$. (d) Fractions of particles as in (a) for HEC 0.05%. (e) Particle positions on the square cross-section at $De = 0.023$. The symbols denote the position of the particle centers and are colored according the band they belong to. (f) Particle positions as in (e), at $De = 0.1$.

at the center of each face is found. A similar situation has also been reported in a cylindrical channel [34]. In other words, for a fixed confinement ratio β, the condition $\mathcal{O}(De) = \mathcal{O}(Re)$, corresponding to $\mathcal{O}(El) = 1$, seems to de-

note a situation where the particle migration is distinctly governed by elastic effects rather than inertial ones.

An idea about the relative strength of elasticity and inertia on particle migration can be given by comparing the theoretical expressions for the migration velocity due to elastic and inertial effects. In Poiseuille tube flow, the inertial migration velocity can be expressed as [124]:

$$\left|V_{\mathrm{m}}^{\mathrm{in}}\right| = B\, Re_{\mathrm{c}}\, \beta^3 \frac{r}{R} \tag{4.1}$$

where r and R are the particle radial position and the tube radius, respectively, B is a constant and $Re_{\mathrm{c}} = \rho \bar{U} R/\eta$ the Reynolds number defined for a cylindrical channel with average velocity $\bar{U}$.

In the same flow field, the migration velocity due to elasticity is [11]:

$$\left|V_{\mathrm{m}}^{\mathrm{el}}\right| = A\, De_{\mathrm{c}}\, \beta^2 \frac{r}{R} \tag{4.2}$$

with A a constant and $De_{\mathrm{c}} = \lambda \bar{U}/(2R)$ the Deborah number defined for a cylindrical channel. Both relationships hold around the channel centreline and for small confinement ratios and flow rates. From the two expressions above, we get:

$$\left|\frac{V_{\mathrm{m}}^{\mathrm{in}}}{V_{\mathrm{m}}^{\mathrm{el}}}\right| = \frac{B}{A}\frac{Re_{\mathrm{c}}}{De_{\mathrm{c}}}\beta = \frac{B}{A}\frac{1}{El}\,\beta \tag{4.3}$$

By taking the values of the constants $A \approx 6.6$ and $B \approx 1.4$ from Refs. [11] and [124], respectively, an estimate of the right-hand side the PEO 0.1% gives that the ratio of the migration velocities is about $3.3 \cdot 10^{-2}$, confirming that inertial effects are much smaller than the elastic ones. Therefore, from Eq. (4.3) appears that the Elasticity number alone gives misleading indications about the relative strength of inertia and viscoelasticity, and one should account for the confinement ratio as well as the correct prefactor B/A. A similar conclusion concerning the inability of the Elasticity number alone to describe the relative effects of inertia and viscoelasticity can be reached by looking at the results reported in Ref. [125]. In that work, indeed, the authors succeeded in going down to $El = 0.05$, and nevertheless found focusing towards the centreline, as in a purely viscoelastic situation. We would also

like to signal that recent 2D simulations of the coupled inertia-viscoelastic case [126] appear to confirm that Re much larger than De is needed (by at least one order of magnitude) to appreciate deviations from the purely viscoelastic case.

Chapter 5

Applications

In this chapter we will use all the informations about particle migration in viscoelastic fluids previously described, in order to present two microfluidic applications, both of interest for the scientific community. The first one is a novel method to derive the fluid relaxation time λ down to milliseconds. The second one combines particle migration in viscoelastic liquids with the magnetophoresis in order to achieve high-efficiency deflection of magnetic particles from a contaminated streamflow into a cleaned one.

5.1 Determination of the fluid relaxation time λ from particle migration in square-shaped microchannel

As comprehensively described in the previous chapters, an accurate knowledge of the fluid relaxation time λ is crucial in the microfluidic design [11, 35]. A major problem in measuring fluid relaxation time by conventional techniques [127] arises for small values of λ (down to milliseconds). The latter is just the case, however, for polymer solutions at low polymer concentrations, which are just the ones generally used in microfluidic devices due to their capability to be pumped through small channels with acceptable pressure

drops. Other important examples of fluid with quite small relaxation times are dilute solutions containing proteins, DNA or biopolymers, all of them being of interest in biological applications [35, 125].

5.1.1 Conventional techniques for measuring λ

Several methods to measure the fluid relaxation time are commonly used, as reported in the literature. A first way to measure λ is through the so-called *linear viscoelastic response* experiments, in which a shearing sinusoidal deformation is applied to the material placed between parallel plates, and the viscous and elastic response of the material are separately evaluated [19]. From these measurements, it is possible to derive the fluid characteristic time by varying the oscillation frequency and observing the switch from a predominantly viscous to a predominantly elastic response [79], those responses being quantified by the loss modulus G'' and the storage modulus G', respectively. Fluids with really small relaxation times (around milliseconds), however, experience the transition from a predominantly viscous to a predominantly elastic regime at rather high frequency ($\sim$300 Hz), where the inertia of the rheometer can affect the measurement [19]. It remains possible to extrapolate the value of λ for a wide class of non-Newtonian fluids from the linear viscoelastic response data at low frequencies [19]. The fundamental bottleneck in this case resides in the possibly small values of the storage modulus G' (less than 10^{-3} Pa), which might even be not detectable by conventional rheometers [127]. In conclusion, the main difficulty of this procedure is due to technological limitations of conventional rheometers presently available on the market [128].

A second approach to determine λ is based on the measure of the *first normal stress difference* N_1 by a steady state shearing experiment [79] and on using the relation $N_1 \propto \lambda$ [19]. Because of the steady state conditions of this kind of experiment, the measure might seem easier than the one through linear oscillations [19]. However, values of N_1 are typically rather low, and are scattered [129], and so it is difficult to extract an accurate value for λ

from this method.

To overcome these difficulties, a novel method named Capillary Breakup Extensional Rheometry (CaBER) has very recently been proposed [82]. The CaBER measurement is based on the evaluation of the rheological *extensional properties* of the liquid, that are related to its viscoelasticity [130, 131]. As anticipated, the main advantage of this technique is in its ability to measure relatively low values of the fluid relaxation time[13, 20, 82]. The intrinsic difficulties in controlling an elongational flow field should be considered, however. Moreover, Zell *et al.* [129] recently showed that a significant difference between the relaxation time measured by CaBER and by conventional rheometers through N_1 may exist. Specifically, it has been demonstrated that, for PolyEthylene Oxide and PolyAcrylAmide solutions, λ-values taken by CaBER experiments are about forty times larger than those derived from N_1 measurements in shear [129].

It so appears that an accurate method for measuring relaxation times of an important class of non-Newtonian fluids (i.e., with low elasticity) is missing. As previously mentioned, this is a relevant issue in microfluidic applications using viscoelastic fluids, because the relaxation time is needed in the design formulas of focusing and separation devices [11, 20, 56, 61], and an erroneous estimate would result in under/oversized devices.

5.1.2 Microfluidc techniques for measuring λ

Novel promising techniques for probing non-Newtonian properties have been developed just in the microfluidics field. As pointed out by Pipe and McKinley [132], the emergent field of microrheometry allows to measure rheological properties of materials, overcoming the technical limitations of conventional rheometry. Indeed, a variety of techniques to accurately measure shear and elongational viscosities have been proposed [132, 133]. Very recently, Zilz *et al.* [127] presented a microfluidic device to derive the fluid relaxation time of low-viscoelastic polymer solutions. The idea is to relate the viscoelastic instability generated in a serpentine microchannel [134] to the fluid relaxation

time λ. This technology requires a complex channel geometry (several bendings) and an efficient controlling system. The flow instability, in addition, is a delicate phenomenon, as testified by the width of the error bars in the their experimental data [127].

5.1.3 Working principle of our 'microrheometer'

We proceed know to show the working principle of our 'microrheometer'. In previous chapter we have seen how fluid elasticity is able to efficiently focus particles along the centreline of a microfluidic channel [11, 20, 56, 61]. In this regard, Romeo *et al.* [61] showed that the spatial evolution of the particle distribution along the micropipe axis is univocally determined by a single dimensionless parameter given by $\theta = De(L/D)\beta^2$, where L is the distance from the inlet, D is the channel diameter and $\beta = D_\mathrm{p}/H$ is the confinement ratio with D_p the particle diameter. Such a scaling (Blue circle in Figure 5.1), valid for low Deborah numbers and for values of $\beta < 0.1$, has been validated through numerical simulations [61] and experiments [34, 61]. In Figure 5.1, we report the data taken from Section 4.1 (open symbols) along with numerical predictions (blue closed circles) obtained through a (dimensionless) migration velocity of the form $V_\mathrm{M}(r) \propto -De\,\beta^2\,r$, with r the distance of the particle from the channel centreline. In this figure, f_1 is the fraction of particles within a circular region in the channel cross-section around the centreline, with radius approximately equal to a particle diameter. We recall that the experiments of Figure 5.1 were carried out by using a water-polymer solution of Poly Vinyl Pyrrolidone (PVP) at 8% wt. In particular they are the same data presented in Section 3.1 and plotted as a function of θ. Numerical simulations [61] were performed at low Deborah numbers (thus non-linear effects such as shear-thinning are not accounted for), and for relatively low confinement ratios, i.e. for $\beta < 0.15$ (see Section 2.10 for details). The good agreement between experiments and simulations even in a square-shaped microchannel confirmed the validity of the above mentioned scaling.

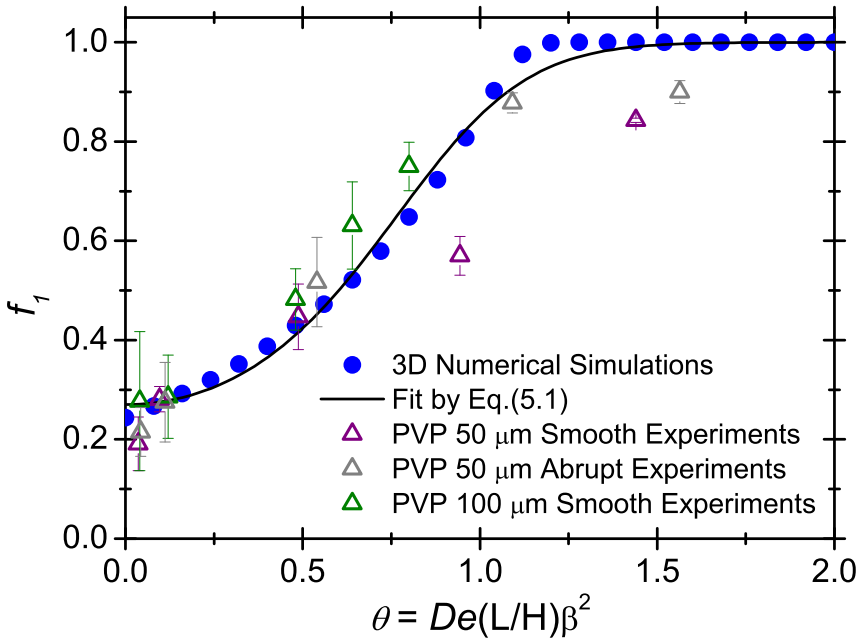

Figure 5.1: Fractions of particles in the first band f_1 as a function of the dimensionless parameter $De(L/H)\beta^2$ as derived from 3D simulations (filled symbols) and experiments (open symbols) as reported in Section 4.1 . The black solid line is a fit of the simulation data through Eq. (5.1). Error bars are calculated from three sets of measurements; error bars smaller than the symbol size are not shown.

Notice that the trend shown in Figure 5.1 is, in principle, valid for any viscoelastic fluid, provided that the Deborah number is low, which holds for most of viscoelastic fluids with λ of the order of milliseconds. In other words, within the assumptions discussed above, the blue symbols in Figure 5.1 represent an *universal mastercurve* describing the spatial evolution of the fraction of particles in the inner band f_1 along the channel axis. Thus, no calibration curve is needed as the experimental conditions, such as channel and particle dimensions, are varied. Therefore, for a given set of geometrical parameters (cross-section channel side length H, confinement ratio β) and flow rate Q,

by measuring the fraction of particles f_1 at a distance L from the inlet, the relaxation time λ (included in De) can be evaluated from the mastercurve.

The previous arguments are based on the predominance of purely elastic effects, with the neglecting of other hydrodynamic phenomena [61]. As a matter of fact, particles subjected to flow in a microfluidic straight channel, even in the case of a Newtonian suspending liquid, can experience hydrodynamic effects due to inertia, such as the Segré-Silberberg [16] effect and the Saffman lift force [135]. It is readily shown, however, that both these inertia-driven migration effects are negligible with respect to the viscoelastic migration. Indeed, the ratio between the Segré-Silberberg and viscoelastic migration velocity can be estimated as proportional to $(Re_\mathrm{f}/De)\,\beta$ [11, 124], with Re_f the Reynolds number of the fluid. Similarly, the ratio between the Saffman [135] and viscoelastic migration velocity can be estimated as proportional to $\sqrt{Re_\mathrm{p}}V_\mathrm{s}/(De\beta^2)$ with Re_p the Reynolds number of the particle and V_s the so-called 'slip velocity' i.e., the longitudinal actual velocity of the particle minus the fluid velocity at the same position. Thus, it is apparent that, when both these two velocity ratios are less than unity, the only relevant mechanism of migration is the one due to viscoelasticity. As shown below, our experiments are so designed as to meet the just mentioned working conditions; hence, since all the hydrodynamic effects are negligible, the measured λ corresponds to the elastic relaxation time only.

As a further confirmation that the characteristic time measured in our experiments is the constitutive relaxation time of the suspending fluid, we compare such constitutive time with the only other characteristic time present in our situation, namely, the so-called 'particle hydrodynamic characteristic time' given by $\tau = \rho_d d^2/(18\eta)$ [136]. It is readily shown that the ratio τ/λ comes out proportional to $(Re_\mathrm{p}/De)\,\beta$ which, in our conditions, is much smaller than unity.

The blue filled symbols in Figure 5.1 were derived from 3D numerical simulations, thus no analytical curve is available. It is helpful to adopt an interpolating analytical expression through the simulation data in Figure 5.1

in order to easily obtain the θ-value from the measured f_1. We find that the following function describes the data with a sufficient accuracy:

$$f_1 = \frac{1}{1 + Be^{-C\,\theta^2}} \tag{5.1}$$

(Eq. (5.1) has to be regarded as a simple formula describing the calculated data, with no physical justification.) This equation is reported with the black line in Figure 5.1, with $B = 2.7$ and $C = 2.75$ obtained by fitting the simulation data. The solid line well fits the data except around the bending towards the plateau. As discussed below, measurements should be avoided in this region, thus the deviations from Eq. (5.1) are not relevant for our purposes.

By inverting the equation above, we get:

$$\theta = \sqrt{\frac{1}{C} \ln\left(\frac{f_1 B}{1 - f_1}\right)} \tag{5.2}$$

that allows to directly compute θ from f_1.

A final remark about the choice of the θ-value is in order. The trend reported in Figure 5.1 reaches a plateau at $\theta > 1$, i.e. all the particles have been focused in the circular band around the channel centreline. In this case, the mastercurve is not invertible. Thus, a feasible measure of the fluid relaxation time through f_1 requires $\theta < 1$. From the definition of θ, it so appears that such a parameter can be changed in several ways. However, the channel side length H needs to be selected sufficiently low in order to guarantee negligible inertial effects. The confinement ratio must satisfy the condition $\beta < 0.15$ but, at the same time, the particle size should be sufficiently large to avoid diffusion, and problems in particle tracking experiments. Recommended ranges for these two parameters are $H = 50 - 100\ \mu m$ with $\beta = 0.05 - 0.1$. Therefore, those two quantities are constrained within quite small intervals. On the other hand, the flow rate Q and the distance from the channel inlet L can be easily adjusted in order to get the θ value in the correct range. More specifically, to speed-up the measurement, it is desirable to use relatively high flow rates, with the only limitation due to avoiding the

arising of inertial effects that can alter the phenomenon. In conclusion, the distance from the inlet of the observation section, proportional to θ, is the tunable parameter to perform reliable measurements.

5.1.4 Determination of the fluid relaxation time with our Microrheometer

We proceed to prove the validity and reliability of the presented method, on two polymer solutions classes, namely PEO and NiPAM, described in Section 3.2 and in Section 3.3, respectively. We compare the so obtained experimental results with those available in literature and with theoretical predictions. With the characterisation of both polymer solutions completed in previous sections, i.e., having identified their respective concentration regimes, we proceed now to show the predictions for the relaxation time, and to compare our data and those by Zell *et al.* [129] with such predictions. The predicted scaling laws for the relaxation time, are [80]:

$$\lambda_D \propto c^0 \qquad \lambda_{SDU} \propto c^{(2-3\nu)/(3\nu-1)} \qquad \lambda_{SDE} \propto c^{3(1-\nu)/(3\nu-1)} \tag{5.3}$$

for the dilute, semidilute unentangled and semidilute entangled regime, respectively [80, 81]. Regarding PEO solutions, the following expressions should hold (see Eq. (5.3) with $\nu = 0.55$):

$$c < c^*_{\mathrm{PEO}} \sim 0.1 \text{ g/dl} \qquad \lambda \propto c^0 \tag{5.4}$$

$$c^*_{\mathrm{PEO}} < c < c_{\mathrm{e,PEO}} \sim 0.45 \text{ g/dl} \qquad \lambda \propto c^{0.69} \tag{5.5}$$

Figure 5.2a shows the relaxation time λ as a function of the concentration. Vertical dashed lines are the estimate of the overlap concentration c^*_{PEO}(left) and of the entanglement concentration $c_{\mathrm{e,PEO}}$(right) from our previous analysis. It is apparent from Figure 5.2a that most of our λ data(red circles) are in the semidilute unentangled regime. We draw the black line in Figure 5.2a,

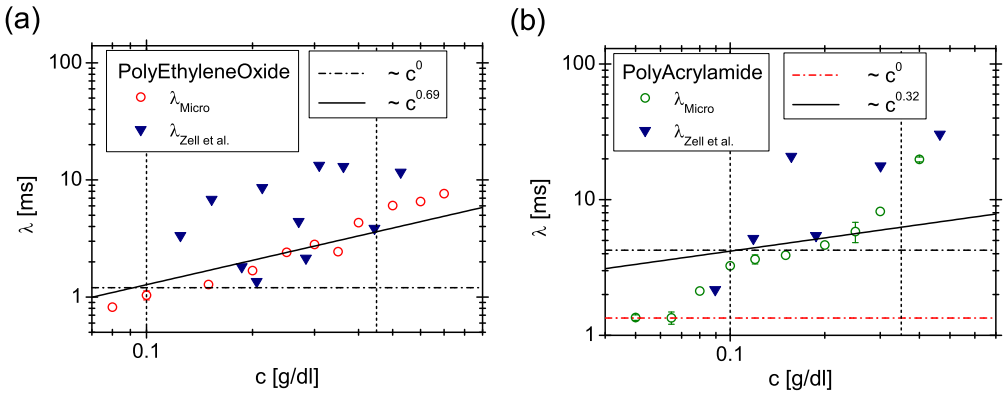

Figure 5.2: (a) Comparison between experimental results on the fluid relaxation time λ derived from our 'microrheometer' with the ones by Zell *et al.*[129], for PEO 4 MDa at different concentrations. Dashed line is the Zimm prediction for the dilute regime, solid line is the Rouse prediction for the semi-dilute unentangled regime, both of then with $\nu = 0.55$. Vertical black dashed lines are at c^* (left) and c_e (right), respectively. Error bars, evaluated by dividing the statistical samples in three sets and calculating the standard deviation between the three λ-values, are smaller than the symbol size. (b) Comparison between experimental results on the fluid relaxation time λ derived from our 'microrheometer' with the ones by Zell *et al.*, for PAM 5-6 MDa at different concentrations. Dashed lines are two possible Zimm predictions for the dilute regime. Solid line is the Rouse prediction for the semi-dilute unentangled regime. All these lines are for $\nu = 0.585$. Black dashed line is the expected theoretical prediction below $c^*_{\rm PAM}$. Red dashed line is the Zimm prediction through our own data for $c << c^*_{\rm PAM}$. Vertical black dashed lines are at c^*(left) and c_e(right), respectively. Error bars are evaluated by dividing the statistical samples in three sets and calculating the standard deviation between the three λ-values. Error bars smaller than the symbol size are not shown.

i.e. the theoretical prediction as in Eq. (5.5), after having computed the prefactor from the data subset in between the two vertical dashed lines. Notice how our data are less scattered with respect to the those by Zell *et al.* [129],

obtained from steady shear measurements of N_1. Our experimental data are also in rather good agreement with the power-law prediction of Eq. (5.5). In particular, by applying the fitting procedure described above for data in the semidilute unentangled regime we find $R^2_{\mathrm{PEO,micro}} = 0.96$, whereas it is $R^2_{\mathrm{PEO,Zell\ et\ al.}} = 0.49$ for Zell *et al.* data [129]. Hence, our results are largely less scattered than those obtained from standard rheometrical measurements.

Figure 5.2b shows the relaxation time λ as a function of the concentration for the PAM solutions. The scaling law are here obtained by assuming $\nu = 0.585$ in Eq. (5.3):

$$c < c^*_{\mathrm{PAM}} \sim 0.1 \text{ g/dl} \qquad \lambda \propto c^0 \tag{5.6}$$

$$c^*_{\mathrm{PAM}} < c < c_{\mathrm{e,PAM}} \sim 0.35 \text{ g/dl} \qquad \lambda \propto c^{0.32} \tag{5.7}$$

Most of the data are again in the semidilute unentangled regime, and show again a good agreement with the power-law of Eq. (5.7) (the prefactor was obtained again from data in between c^*_{PAM} and $c_{\mathrm{e,PAM}}$ only), with $R^2_{\mathrm{PAM,micro}} = 0.96$. Notice that, also in this case, the R^2 calculated from the rheometrical data by Zell at al. [129] ($R^2_{\mathrm{PAM,Zell\ et\ al.}} = 0.45$) is much smaller than our own, thus confirming that conventional rheometrical techniques are less effective than the microrheometrical technique proposed here. For $c < c^*_{\mathrm{PAM}}$, conversely, data are not in strict agreement with theoretical predictions. Indeed, data would be expected to lye on the black horizontal dashed line of Figure 5.2b, whereas they tend to lye (for $c \ll c^*_{\mathrm{PAM}}$) on the red dashed line of the same plot. This behaviour possibly evidentiates that the dilute-semidilute unentangled transition is not sharp. The same kind of discrepancy with the theory around c^* had been previously found by Tirtaatmadja *et al.* [82] on PEO solutions. Indeed they found that, for $0.05\ c^* < c < c^*$, the relaxation time $\lambda \propto c^{0.65}$, in contrast with the Zimm prevision in Eq. (5.3); they also found that the Zimm prevision is only recovered when $c \ll c^*$. This unexplained behaviour is, in fact, similar to our observations below c^*_{PAM}. However, more data in the low concentration range would be needed to confirm or deny the presence of such pre-transitional behaviour.

5.2 Magnetic particles deflection in a modular microfluidic device combining magnetophoresis and viscoelasticity

The deflection efficiency of magnetic beads in a microfluidic channel through magnetophoresis can be improved if the particles are somehow focused along the same streamline in the device. In this section, we present a microfluidic device aimed to deflect magnetic beads from a contaminated stream into a cleaned one. At this aim, we design and fabricate a microfluidic device made of two modules, each one performing a unit operation. A suspension of magnetic beads in a viscoelastic medium is fed to the first module, which consists in a straight rectangular-shaped channel. Here, the magnetic particles are focused by exploiting fluid viscoelasticity. Such a channel is one inlet of the second module, which is a H-shaped channel, where a buffer stream is injected in the second inlet. A permanent magnet is used to displace the magnetic beads from the original to the buffer stream. Experiments with a Newtonian suspending fluid, where no focusing occurs, are carried out for comparison. When viscoelastic focusing and magnetophoresis are combined, magnetic particles can be deterministically separated from the original streamflow to the buffer, thus leading to a high deflection efficiency (up to $\sim 96\%$) in a wide range of flow rates. The effect of the focusing length on the deflection of particles is also investigated.

5.2.1 Concept design

A schematic top view of the device used in this work is reported in Figure 5.3a: the microfluidic system is composed of two modules in series, and each of them performs a unit operation. The first module (light blue in Figure 5.3a) is a straight microchannel with rectangular cross-section with sides $W = 100$ μm and $H = 50$ μm, and length L_{f}. A suspension of 10 μm diameter magnetic beads is fed at the inlet of this channel with a flow rate Q.

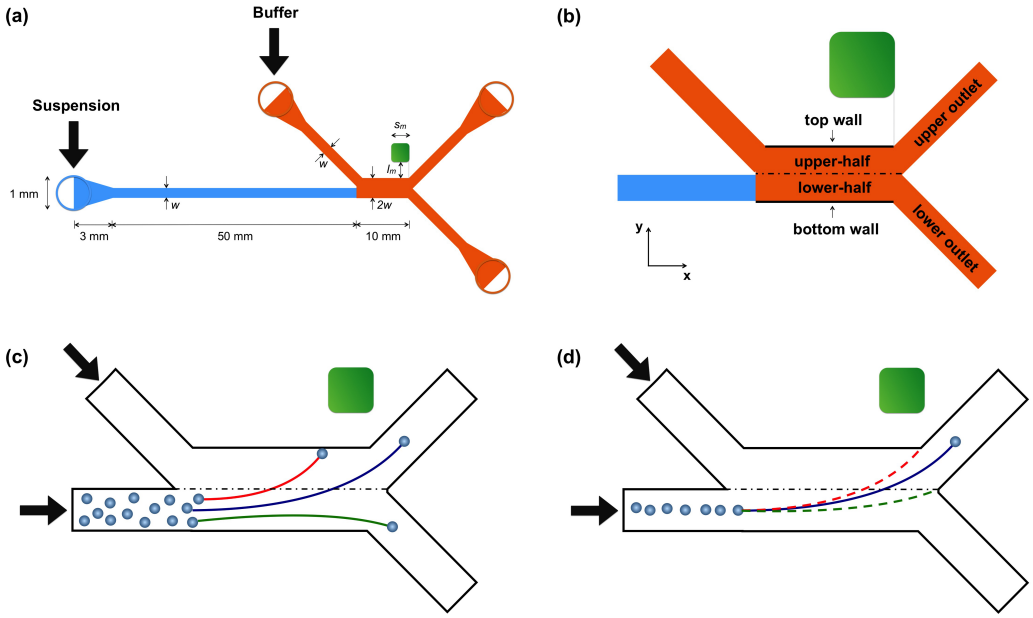

Figure 5.3: (a) Schematic top view (not to scale) of the modular microfluidic device. The focusing module is shown in light blue, the separation module is shown in orange. The height of the device is $H = 50$ μm. (b) Closer view of the separation channel. The nomenclature adopted in the main text to indicate the two parts of the separation chamber, the outlets and the walls of the separation channel orthogonal to the xy-plane is reported. (c) Schematic representation of the possible trajectories of the magnetic beads in a Newtonian fluid. The green paths correspond to beads that do not cross the dashed-dotted line and exit the channel through the lower outlet. The blue curves denote particles that correctly migrate in the buffer stream and are transported out of the device through the upper outlet. The red paths correspond to beads that deviate too much and get close to the top wall. (d) Schematic representation of the magnetic beads trajectories after viscoelastic focusing. The blue line is the ideal path followed by the focused particles. The green and red dashed lines delimit the range of possible trajectories corresponding to the correct displacement of the particles.

When a viscoelastic fluid is used as suspending medium, particle alignment is expected to occur in this module. For this reason, we will refer to such a channel as the 'focusing module'.

The focusing module is connected to the second part of the device (orange in Figure 5.3a) consisting of a microchannel with rectangular section with sides $2W$ and H, and length L_{d}. As discussed below, magnetic deflection of the beads takes place in this channel, thus it will be referred as 'deflection module'. The focusing module is one inlet of the deflection module, which possesses a second side inlet and two outlets. From the side inlet, a buffer solution made by the same fluid as the suspending matrix of the suspension is injected with the same flow rate Q of the particle suspension. Thus, the fluid (suspension and buffer solution) in the deflection chamber flows at a flow rate $2Q$. Due to the low Reynolds numbers (see below), no mixing occurs downstream the junction [21]. In this channel, of course, the viscoelastic normal stresses still act on the particles. However, the confinement ratio along the $y-$direction in the deflection channel (see Figure 5.3b) is twice smaller as compared to the focusing channel. As the migration velocity is proportional to the square of the confinement ratio [11], the lateral motion in the deflection module is much less effective than that occurring in the focusing module. Hence, without other external forces, the magnetic beads as well as other particles suspended in the sample essentially keep on traveling on the same streamlines as in the focusing module and remain below the dash-dot line of Figure 5.3b. We will refer to the region of the channel below the dash-dot line, i.e., the one aligned with the cross-section of the focusing module, as 'lower-half' of the deflection chamber. Conversely, we will refer to the region of the channel above such dash-dot line, i.e., the one corresponding to the cross-section of the buffer solution inlet, as 'upper-half' of the deflection chamber. Similarly, the two exit channels are referred to as lower and upper outlets. Since the outlets are symmetric with respect to the deflection channel centerplane, the suspension and the buffer solution leave the channel from the lower and upper outlets, respectively. Finally, we indicate with 'top'

and 'bottom' walls, the two walls of the deflection channel orthogonal to the $xy-$plane (see Figure 5.3b) near the upper and lower outlets, respectively.

The objective of the device is to displace the magnetic beads from the original to the buffer stream. To this aim, a cubic permanent magnet with side s_{m} (green in Figure 5.3) is placed at a distance l_{m} from the top wall of the deflection module. The magnetic particles are subjected to a lateral magnetic force that deflects their path and move the beads from the lower to the upper half of the deflection chamber.

In the absence of focusing, the magnetic beads are randomly distributed along the cross-section of the channel inlet. Neglecting small flow disturbances due to the junction, it can be assumed that the beads are still randomly distributed as they get in the lower half of the deflection channel (Figure 5.3c). The beads near the walls travel slower than those near the centreline. Furthermore, the particles near the centreline are closer to the magnet than those near the bottom wall and, as such, experience a stronger magnetic force. Depending on the flow rate and on the magnitude of the magnetic force, three different behaviours may occur: i) the particles can be correctly displaced from the lower to the upper half of the deflection chamber and leave the device through the upper outlet (blue trajectory in Figure 5.3c); ii) the particles are displaced to the upper half of the channel but travel very close to the top wall whether the flow rate is too low and/or the magnetic force is too high (red trajectory in Figure 5.3c); iii) the particle displacement is insufficient and they leave the device through the lower outlet if the flow rate is too high and/or the magnetic force is too low (green trajectory in Figure 5.3c). Needless to say, particles traveling close to the top wall are undesired as they flow very slowly (decreasing the deflection throughput) or, even worse, they can remain attached to the wall. It should be noted that, for a fixed flow rate and magnetic force, the path followed by each particle strongly depends on its position along the channel cross-section. In dimensionless terms, a specific value of the particle magnetization parameter might be optimal for particles near the centreline but not for those near the walls,

or vice versa.

If the particles have been effectively aligned on the centreline of the focusing module as schematically shown in Figure 5.3d, they should follow the same streamline in the deflection module. Of course, the magnetic force as well as the particle velocity changes as the beads cross the deflection chamber. However, in principle, the history of the magnetic force and velocity experienced by each particle should be the same. Therefore, we expect that, in a range of the particle magnetization parameter, all the particles are equally displaced from the lower to the upper half of the deflection chamber and leave the device through the upper outlet, as shown by the blue trajectory in Figure 5.3d. Low values of the particle magnetization parameter (i.e., a low magnetic force and/or high flow rate) would lead to an insufficient displacement and all the particles leave through the lower outlet. On the contrary, high Mn_{p}-values (i.e., a high magnetic force and/or low flow rate) would push the particles near the upper wall of the deflection chamber, reducing the deflection efficiency. The appropriate range of Mn_{p} is determined by the two values corresponding to the dashed green and red trajectories in Figure 5.3d.

From the discussion just presented, it clearly appears that the deflection efficiency is strictly related to the focusing efficiency that, in turn, can be improved in several ways (e.g., by increasing the fluid elasticity, the flow rate, the confinement or the channel length [11]). To analyse the combined effect of the focusing on the magnetic particle displacement, we fabricated two devices with different lengths of the focusing module L_{f} and of the deflection channel L_{d}. More specifically, we refer to 'short' device corresponding to $L_{\mathrm{f}} = 5$ cm and $L_{\mathrm{d}} = 1$ cm and to 'long' device the one corresponding to $L_{\mathrm{f}} = 7$ cm and $L_{\mathrm{d}} = 1.6$ cm.

5.2.2 Device efficiency

Figure 5.4 shows a top view of the deflection module near the two outlets for four different conditions. The long device, as defined in section 5.2.1 was

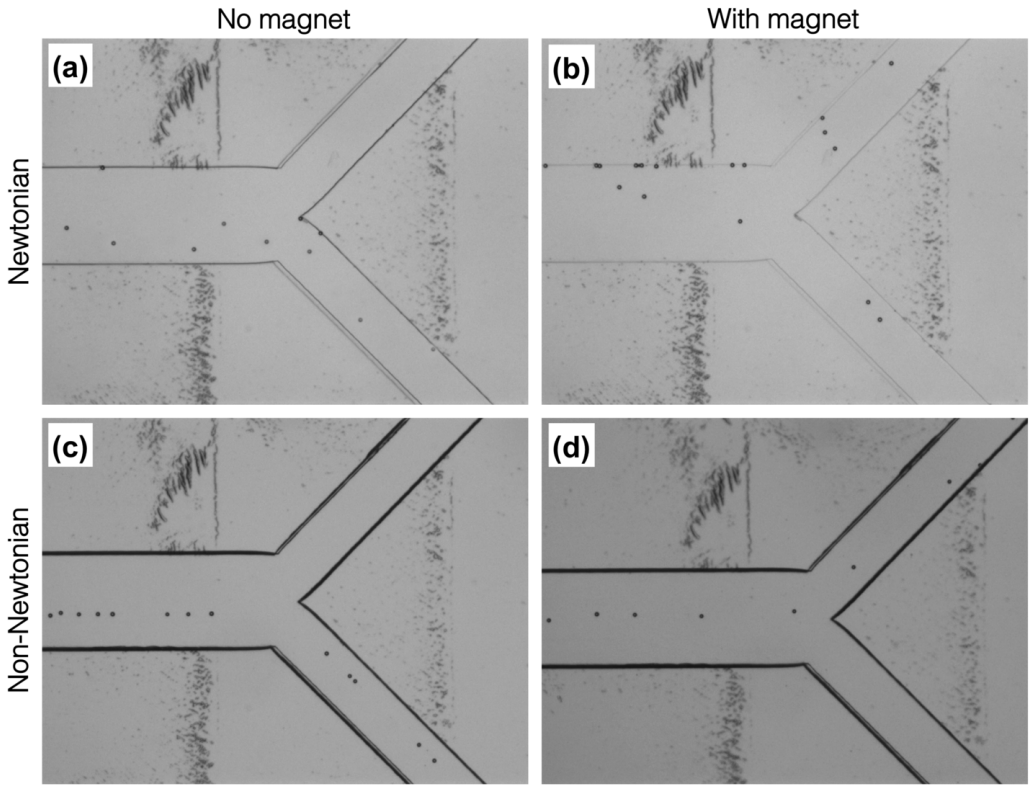

Figure 5.4: Top-view of the deflection module bifurcation with a suspension of particles flowing in the long device. Four different experimental settings are considered: (a) particles suspended in 60% w/w GWS without magnet ($De = Mn_{\mathrm{p}} = 0$); (b) particles in 60% w/w GWS with the permanent magnet ($De = 0$, $Mn_{\mathrm{p}} = 0.5$); (c) particles in 0.5% w/w PAM without magnet ($De = 0.24$, $Mn_{\mathrm{p}} = 0$); (d) particles in 0.5% w/w PAM with the permanent magnet ($De = 0.24$, $Mn_{\mathrm{p}} = 0.21$).

used in these experiments. In Figure 5.4a, a snapshot of the distributions of particles suspended in 60% w/w GWS in the absence of the magnet, i.e., for $De = Mn_{\mathrm{p}} = 0$, is reported. All the particles are confined in the lower half of the channel, due to the fluid dynamics action of the buffer solution stream; moreover, since no lateral migration occurs in inertialess Newtonian fluids, the particles are randomly distributed within the channel cross-section. In such a situation, they follow the fluid streamlines and leave

the device through the lower outlet.

When the magnet is introduced, the nickel-coated particles feel the magnetic force and cross the streamlines of the fluid carrier moving from the lower to the upper half of the deflection channel. However, as the beads arrive in the deflection module randomly distributed, they flow with different velocities and perceive different magnetic forces depending on their position. A typical situation is shown in Figure 5.4b, corresponding to the Newtonian suspension ($De = 0$) with $Mn_{\mathrm{p}} = 0.5$. In this case, some particles are deviated to the upper outlet, whereas other particles still exit the channel through the lower outlet. In addition, it can be also noted that the particles that crossed to the upper part of the deflection channel are very close to the upper wall, and can eventually roll over or get stuck on the PDMS wall.

In the case of the suspension of particles in the 0.5% w/w PAM, the alignment of the beads on the centreline of the focusing module occurs owing to the fluid viscoelasticity. Hence, in the absence of the magnet ($Mn_{\mathrm{p}} = 0$), they are expected to exit the deflection module through the lower outlet by following the same streamline. This is indeed the case, as confirmed in Figure 5.4c for $De = 0.24$.

By introducing the magnet, the particles are deviated towards the upper half of the channel. In contrast with the Newtonian suspension, the particles are focused on the same streamline thus moving with similar velocities and they perceive a similar magnetic force while traveling in the deflection channel. Therefore, they can be deterministically addressed to the desired outlet, as displayed in Figure 5.4d for $Mn_{\mathrm{p}} = 0.21$ and $De = 0.24$. In addition, viscoelastic forces acting in the deflection module push the beads towards the channel center, thus preventing them to stick on the top wall.

A quantification of the device's performance is done by introducing the deflection efficiency η_{tot} as:

$$\eta_{\mathrm{tot}} = \frac{N_{\mathrm{up}}}{N_{\mathrm{up}} + N_{\mathrm{down}} + N_{\mathrm{stuck}}} \tag{5.8}$$

with N_{up} the number of particles exiting the deflection module through the upper branch, N_{down} the number of particles exiting through the lower

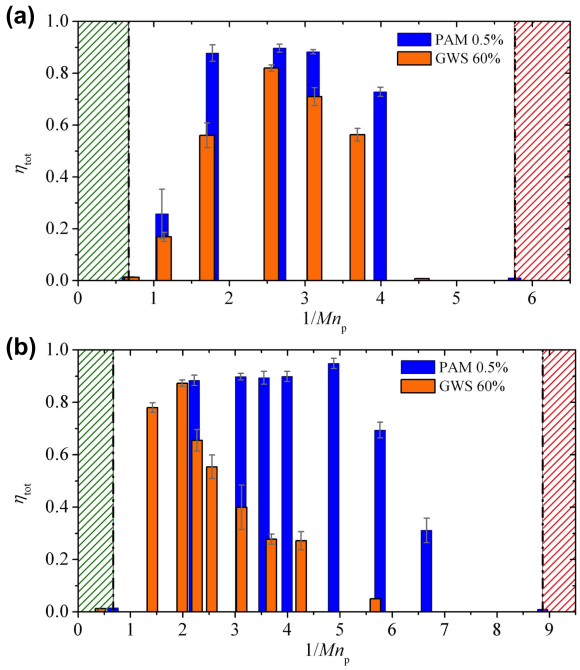

Figure 5.5: deflection efficiency η_{tot} as a function of the inverse of the particle magnetization number $1/Mn_{\text{p}}$ for 60% w/w GWS (orange bars) and 0.5% w/w PAM (blue bars), (a) refers to the short device whereas (b) to the long device. The error bars are obtained by dividing each sample in three subsets and calculating the average efficiency and the corresponding standard deviations for these three data subsets. The right red dashed region corresponds to Mn_{p}-values such that all the particles exit the deflection channel through the lower outlet. The left green dashed region corresponds to Mn_{p}-values such that all the particles move in proximity of the top wall of the deflection channel and do not exit the device within the observation time of the experiments. The values of $1/Mn_{\text{p}}$ corresponding to the boundaries of these two regions (dash-dot lines) refer to the PAM solution.

branch, and N_{stuck} the number of particles stuck on the wall in the observation time, respectively. We performed experiments at different flow rates in both the short and long device.

In Figure 5.5, η_{tot} is shown as a function of the inverse of Mn_{p} for 60%

w/w GWS (orange bars) and 0.5% w/w PAM (blue bars), for the short (Figure 5.5a) and long (Figure 5.5b) device. We choose to plot the efficiency versus $1/Mn_{\mathrm{p}}$ as, for fixed fluid and geometrical parameters, it is proportional to the flow rate, which is our operating variable. For both suspending fluids and in both devices, by decreasing Mn_{p} (i.e., by increasing the flow rate), the deflection efficiency η_{tot} first increases, then it attains a maximum, and finally decreases. Such a behaviour can be explained in terms of the competition among drag force, magnetic force, and, for the PAM solution, elastic force.

For the Newtonian matrix, at high Mn_{p}-values (low flow rates), the magnetic force is much stronger than the drag force, so the term N_{stuck} is high, and η_{tot} decreases. In addition, as discussed above, sedimentation also plays a role at low flow rates, pushing the particles towards the channel wall parallel to the xy-plane (see Figure 5.3). Here, the beads velocity is low, enhancing the effect of the magnetic force in deflecting the particle trajectories, and increasing the fraction of particles that are collected to the top wall of the deflection channel. On the other hand, at very low Mn_{p}-values (very high flow rates), the drag force largely overcomes the magnetic attraction. In this case, the flow velocity is so high that the magnetic force is unable to displace the particles from the lower to the upper half of the deflection channel and the particles get out of the device through the lower outlet. This increases the term N_{down} and consequently decreases the deflection efficiency.

Similar considerations can be done for the viscoelastic suspension. In this case, however, at the lowest flow rate, the onset of normal forces pushes the particles away from walls. In addition, the normal forces also contrast sedimentation by pushing particles towards the middle of the channel cross-section. Both effects contribute to decrease N_{stuck} and, in fact, an efficiency higher than the Newtonian case is observed. At the largest flow rate, similarly to the Newtonian case, the translational particle velocity is too large and the beads escape from the magnetic field and go through the lower branch. These two limiting behaviours are indicated as green and red dashed zones in Figure 5.5. Notice that the values of $1/Mn_{\mathrm{p}}$ reported in this Figure that delimit

these zones (dash-dot lines) correspond to the lowest and the highest flow rates such that the deflection efficiency of beads in the viscoelastic suspension is approximately zero.

Interestingly, at intermediate flow rates, a systematically higher efficiency is found for the viscoelastic case compared with the Newtonian one. Let us first consider the data pertaining to the short device shown in Figure 5.5a. While the best efficiency achievable with 60% w/w GWS is about 80% at $1/Mn_{\mathrm{p}} = 2.55$, the best performance with 0.5% w/w PAM is 92% at $1/Mn_{\mathrm{p}} = 2.66$. Moreover, such a remarkable efficiency-value is almost invariant in the range $1.77 < 1/Mn_{\mathrm{p}} < 3.1$, whereas significant decreases are detected for the Newtonian suspending liquid as Mn_{p} moves away (in both directions) from 2.55. The higher efficiencies as well as the wider flow rate range that allows for the best deflection performances can be ascribed to the effect of particle alignment in the focusing module: the beads, following the same streamline, perceive the same magnetic action and are equally displaced from the original suspension to the buffer solution. As discussed in section 5.2.1, if the particles are perfectly aligned before entering the deflection module and feel the same magnetic force (i.e., the beads are exactly equal in size and have the same magnetic susceptibility), they should follow a single path for a fixed particle magnetization parameter. Therefore, the operative range of the device in terms of Mn_{p} is readily identified: the lowest Mn_{p}-value (the highest flow rate) corresponds to the path such that the particles 'hit' the junction between the two outlets (green line in Figure 5.3d); the highest Mn_{p}-value (the lowest flow rate) corresponds to the path such that the beads approach the upper wall of the deflection channel just before the outlets (red line in Figure 5.3d). For particle magnetization numbers in between these two limiting values, all the particles leave the device through the upper outlet achieving, theoretically, an efficiency close to unity. The lower efficiency found in these experiments could be ascribed to several reasons: i) the focusing is strong but not perfect; ii) slightly different particle sizes and/or susceptibility affect the magnetic force; iii) particle aggregates

are occasionally observed in our experiments; iv) sedimentation might have a weak effect in the focusing module, working against alignment. Nevertheless, the measured efficiency is always larger than the Newtonian case, proving the effectiveness in using fluid viscoelasticity combined with magnetophoresis.

The effect of the focusing on bead deflection efficiency is readily observed by looking at the data for the long device shown in Figure 5.5b. The longer focusing length improves the alignment of the particles entering the deflection chamber and, in turn, contributes to: i) increase the efficiency up to 96% (at $1/Mn_{\mathrm{p}} \sim 5$); ii) extend the operative range of particle magnetization parameter that assures high deflection efficiency. In this regard, it has to be mentioned that the longer deflection channel of this device (as compared to the short one) also contributes to increase the performances by preventing particle deflection due to the magnetic force while the beads travel in the focusing channel. Finally, a longer deflection channel is also responsible for the wider operative range of flow rates reported in Figure 5.5. (Notice, for instance, that η_{tot} is approximately zero for the viscoelastic case at $1/Mn_{\mathrm{p}} \sim 5.7$ for the short device and $1/Mn_{\mathrm{p}} \sim 9$ for the long one.) Indeed, in the long deflection channel, the particles are subjected to the magnetic force for more time before encountering the bifurcation. Hence, even at high flow rates (low Mn_{p}-values), they have sufficient space to cross from the lower to the upper-half of the deflection module.

We also remark that the separation efficiency achieved in our device through combination of viscoelastic focusing and magnetophoresis is higher than that obtained in similar devices where no particle alignment is preliminarily achieved [51]. Appreciable efficiency values can be obtained in Newtonian suspending media, but needing the use of extra components that considerably complicate the device fabrication such as micro-combs with sharp tips, ring conductors, angled ferromagnetic wire or strip arrays (see [137] and the references therein).

As a proof of principle, we run an experiment where we feed the device with a rhodamine-contaminated 0.5% w/w PAM solution carrying 10 μm

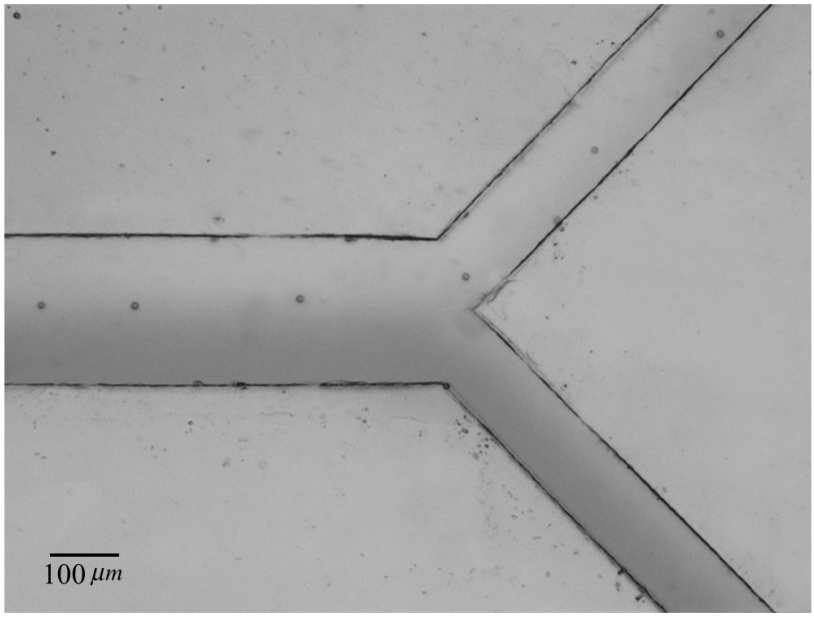

Figure 5.6: Top-view of the deflection module bifurcation showing the deflection of the magnetic particles from a rhodamine-contaminated 0.5% w/w PAM solution for $Mn_{\mathrm{p}} = 0.24$ and $De = 0.21$.

diameter nickel-coated particles, whereas the side flow is a 'clean' 0.5% w/w PAM solution with the same flow rate. The particle magnetisation number is $Mn_{\mathrm{p}} = 0.21$, whereas the Deborah number is $De = 0.24$. Figure 5.6 shows a snapshot of the top view of the deflection module near the bifurcation. The magnetic beads are displaced from the rhodamine-contaminated stream (dark grey) to the buffer solution (light grey) following approximately the same trajectory. The beads are finally collected at the end of the upper outlet.

Finally, we demonstrate the performances of our device by separating magnetic and non-magnetic beads simultaneously suspended in the inlet stream. Figures 5.7a1 and 5.7b1 show a top view of the deflection module near the two outlets when 10 μm diameter magnetic beads are suspended in the PAM solution together with either 6 μm or 20 μm diameter non-magnetic beads, respectively. The long device is used with $Mn_{\mathrm{p}} = 0.21$ and

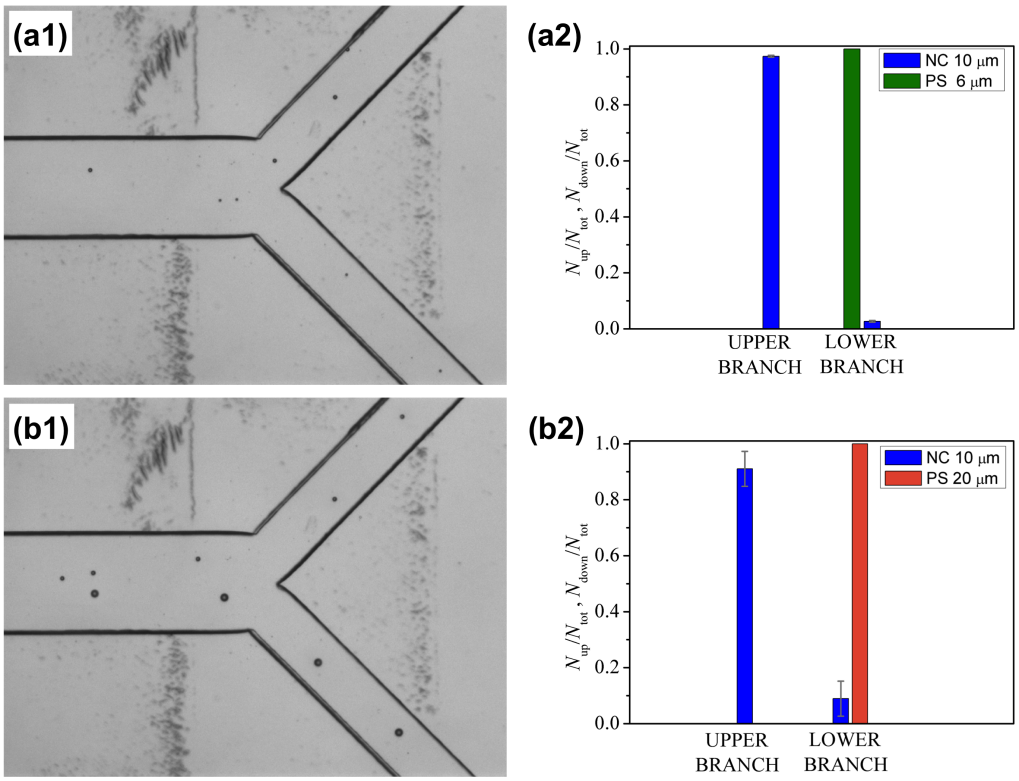

Figure 5.7: Left: Top-view of the separation module bifurcation showing the separation of 10 μm magnetic particles from 6 μm (a1) and 20 μm (b1) non-magnetic particles. The long device is used with $Mn_{\mathrm{p}} = 0.21$ and $De = 0.24$. Right: Number of beads exiting the outlet branches normalised by the total number of particles of the same size N_{tot} observed in the experiments. In the legend, PS and NC denote PolyStyrene and Nickel-Coated particles.

$De = 0.24$. In both cases, almost all the magnetic beads are displaced to the buffer stream and leave the device through the upper outlet. In contrast, the non-magnetic particles remain confined in the lower-half of the deflection channel. Notice that the non-magnetic beads are, of course, subjected to the alignment phenomenon in the focusing module and, indeed, travel through the deflection chamber following the same streamline. (Actually, the smallest beads are not perfectly aligned because of the lower confinement ratio in the focusing module that reduce the viscoelastic force [61]). In Figures 5.7a2 and

5.7b2, we report the number of magnetic and non-magnetic beads exiting the upper and lower branches normalized by the total number of particles N_{tot} of the same size observed in the experiments. It clearly appears that only a few fraction of magnetic particles (blue bars) leave the device through the lower branch, whereas all the non-magnetic particles, regardless of their size, remain confined in the lower-half of the deflection channel and leave the device through the lower outlet. We also mention that no particle (magnetic or non-magnetic) has been observed near the channel walls, confirming the improved fluid dynamic conditions induced by the focusing mechanism. As a final comment, the alignment of the non-magnetic beads has the further advantage of speeding up the particle outflow rate as they travel along a streamline close to the central one (that is the fastest).

Chapter 6

Conclusions

In this thesis the effect of fluid viscoelasticity on particle migration in square-shaped microchannels is studied. In Chapter 3 we characterised several polymer solutions *classes* ranging from the constant viscosity fluid (as the Poly Vynil Pyrrolidone solution) to the more complex HyroxyEthyl Cellulose (HEC). PVP presents a constant viscosity over three order of magnitude in the shear rate $\dot{\gamma}$. In addition, the fluid elastic properties reflect those of the Maxwell fluid [19]. Poly Ethylene Oxide solutions, in contrast, exhibit different rheological behaviours in dependence on their mass concentration. In particular, at low concentration they behave like the constant-viscosity liquids with an elastic Maxwell-like behaviour. At a polymer concentration $c = 0.5\%$, the solution exhibits a shear-thinning behaviour starting from $\dot{\gamma} \sim 100\ s^{-1}$. This behaviour is more and more pronounced when increasing the polymer concentration; in particular at $c = 1.6\%$ the shear-thinning zone starts from $\dot{\gamma} \sim 1\ s^{-1}$. This is due to the strong intermolecular interactions between polymer chains, that cause shear-thinning at lower shear rate values [19, 79]. We also characterised the transition between different polymers regimes for PEO 4 MDa. In particular we estimated the value of the overlap concentration c^*, and also that of the entanglement concentration c_e: we find $c^*_{\mathrm{PEO}} \sim 0.1$ g/dl and $c_{\mathrm{e,PEO}} \sim 0.45$ g/dl. In the semidilute entangled regime, a deviation from the pure Maxwell model in the elastic response at

high frequencies is observed. This behaviour, however, is common in almost all the polymer solution in this regime. The explanation of this deviation resides again in the intermolecular interaction between polymer chains; furthermore it is not possible to consider these fluids as Maxwell-like with a single λ, but they can be mathematically modelled as a modified Maxwell fluid with several relaxation times, or λ-spectra. Nevertheless, the intersection between the straight lines of the Maxwell model, i.e. at low frequencies, gives the *longest* relaxation time. Regarding the non-ionic PolyAcrylAmide (niPAM), results analogous to the PEO solutions have been found. We reported the estimate for the overlapping concentration $c^*_{\mathrm{PAM}} \sim 0.1$ g/dl and an entanglement concentration $c_{\mathrm{e,PAM}} \sim 0.35$ g/dl. Ionic PolyAcrylAmide (iPam) have a different rheological behaviour respect to the non-ionic one. In this case, in fact, macro- and micro-rheological measurement (the last one performed by using Optical Tweezers (see section 2.8)) show that iPam solutions behave like polyelectrolyte polymers. iPam with two different molecular weights, namely $M_w = 1500\ Da$ and $M_w = 1.145\ MDa$, in water solution at several mass concentrations are characterised. In particular, we found an entanglement concentration $c_e \sim 12\%$ for the iPam 1500 Da and $c_e \sim 0.38\%$ for iPam 1.145 MDa. A remarkable agreement between micro- and macrorheology data are found for both fluid by applying the procedure described in section 2.8. In addition, from microrheology measurements, we derive the solutions' frequency response for iPam 1.145 MDa. Good agreement between experimental data and theoretical predictions is found. We finally reported the rheology of HydroxyEthyl Cellulose solutions (HEC). The results indicate that for $c < 0.2\%$ all the solutions have an almost constant viscosity value for shear rate. For $c > 0.2\%$, in contrast, at high shear rates, the solutions exhibit a weak shear thinning behaviour. For $c > 0.2\%$ in addition, we found rod-like structures with a length $\sim 8\ \mu$m, similar to those found by Arfin and Bohidar [107]. Regarding the dynamic response, it was possible to identify the characteristic frequency scaling laws of the moduli, predicted for instance by Shankar *et al.* [115] and Morse [116, 117, 118], for rod-like poly-

mers solutions. We recall again the remarkable agreement between macro- and micro-rheology data.

In Chapter 4 several important results on particle migration in viscoelastic liquids are obtained. We demonstrated for the first time the capability to achieve 3D focusing in square-shaped microchannel by using purely viscoelastic forces. A water solution of 8% PVP is used as suspending liquid. A novel method to reconstruct the particle position over the channel cross-section by combining simple optical microscopy particle tracking measurements and numerical simulations is proposed (see section 2.6). Experiments are performed in two channels with cross-section side dimension of 50 μm and 100 μm at different flow rates. The confinement ratio is kept constant, $\beta \cong 0.1$, and the measurements are taken at a given distance from the inlet ($L = 4$ cm). In order to optimise the flow-focusing conditions, for the 50 μm channel, we also investigate the effect of the entrance shape (smooth and abrupt). For all the tested flow and geometrical conditions, our results show that the particles migrate towards the channel centreline, promoting 3D flow focusing. The focusing mechanism is enhanced for higher flow rates (higher Deborah numbers). An abrupt contraction at the entrance alters the inlet distribution, leading to a particle depletion layer along the channel walls, and reducing the focusing length.

In the same chapter, we carried out several experiments on particle migration in PEO solutions at different flow rates, in order to study the effect of the shear-thinning and the competition between inertia and elasticity. Measurements are taken at a fixed distance from the inlet $L = 8$ cm and the particle positions over the channel cross-section are recovered by combining a particle tracking method with 3D numerical simulations as reported in Section 2.10. Our results show that particles suspended in PEO at low concentration, i.e. a constant-viscosity fluid, are focused towards the channel centreline due to the medium elasticity. Such an inward migration occurs even at the lowest Elasticity number ($El \sim 0.6$) for which one could expect that inertial effects (working in opposite direction as the viscoelastic ones) play a role. Since

our experiments do not show any qualitative change from the high Elasticity number case, we conclude that elastic forces are much stronger than the inertial ones when the two representative dimensionless numbers (De and Re) are of the same order of magnitude, and hence $El \sim 1$. Indeed, the relevant dimensionless parameter should account for the confinement ratio as well as a prefactor 'measuring' the relative strength of the inertial and viscoelastic migration velocities. Finally, strongly shear-thinning fluids qualitatively alter the scenario; in particular, particles migrate towards the channel centreline when exploring the fluid constant-viscosity region, whereas at high flow rate, i.e. in the fluid shear-thinning region, particles are pushed towards the corners of the channel cross-section. This is the first experimental observation of particles at the corners. Same results hold for particle suspended in HEC solutions at concentrations $c < c_e = 0.2\%$. When $c > c_e$ in contrast, particles migrate towards the channel walls at low Deborah numbers De, while by increasing the De of a factor of 2, particles migrate towards the four corners and also towards the corners of the fifth band. This behaviour could be ascribed to the presence of supramolecular structures, in the entangled regime, with a length comparable to the particle size. It could imply, in fact, a wide depletion layer closed to the channel walls that affect the migration phenomenon. Nevertheless a more deeper investigation is necessary in order to fully clarify these results.

In Chapter 5 we reported two applications arose from the results of Chapter 4. First, we presented a novel method to measure the relaxation time λ of viscoelastic fluids down to milliseconds. The idea is to exploit the relation between the characteristic time λ and the phenomenon of viscoelasticity-induced particle migration in microchannel flow presented in Chapter 4. We demonstrate that an accurate measurement of λ can be obtained from the measurements of the normalised particle fraction f_1 at the axis of the microchannel. We point out that the measurements of f_1 does require rather standard particle tracking experiments, thus making the proposed method handy and relatively easy to be performed. The performances of the 'mi-

crorheometer' are tested on two glycerol-water solutions on PEO and niPAM solutions at various concentrations. The obtained data are reliable, accurate, and in good agreement with theoretical predictions [80, 81]. The range of applicability of our novel technique is comparable with that recently proposed by Zilz *et al.* [127]. Our device, however, is by far simpler in terms of design and working principles. Indeed, the working principle of our 'microrheometer', being based on the 'universal' curve, does not need a calibration procedure. In this regard, we remark that the measurements performed in this paper exploit a square-shaped microchannel with side $H = 100$ μm.

Finally, we presented a modular microfluidic device in which deflection of magnetic particles in a H-shaped channel is achieved with a deflection efficiency up to 96%. The idea is to align the magnetic beads in a focusing module before entering the deflection module. Particle alignment is induced by using a viscoelastic fluid as suspending medium. The focusing module is one inlet branch of the H-shaped channel, whereas a buffer solution is injected in the other inlet. A permanent magnet is used to generate an attractive magnetic force which displaces the beads from the original to the buffer stream.

We have demonstrated that the preliminary focusing effect improves the deflection efficiency by reducing the number of particles that leave the channel through the undesired outlet or that get stuck on the wall closer to the magnet. Furthermore, by confining the particles to move along a single streamline strongly enlarges the operative window of the device (in terms of flow rate, magnet and particle properties) that assures the highest deflection efficiency. Moreover, the normal stresses induced by fluid viscoelasticity also have a positive effect in contrasting sedimentation which is an issue when dealing with micrometer-sized particles. The proposed modular device has been successfully tested to separate magnetic and non-magnetic beads of different size with high efficiency.

As a final remark, we highlight that the viscoelastic fluid employed in this work is a 0.5% w/w aqueous solution of PolyAcrylamide, thus a very

dilute solution of a fully biocompatible polymer. Hence, the use of the device proposed here could be straightforwardly extended to biological and biotechnological applications.

In conclusion we have comprehensively analysed the particle migration phenomenon in viscoelastic liquids by using several suspending matrices. All the results found from the particle migration phenomenon are used to design a novel method to derive the fluid relaxation time and a modular microfluidic device useful for deflecting magnetic particles from a contaminated streamflow into a cleaned one.

Future works could explore more in deeper the effect of very complex fluids, like cellulose solutions and wormlike micellar solutions, on particle migration. In addition more concentrated solutions, in terms of particles concentration, could be explored in order to confirm or not such conclusions. Moreover, 3D particle focusing can be used to deterministically separate particles by adding a deflection modulus in series. Recent simulations [138], show that particles suspended in a non-Newtonian fluid, subjected to a Poiseuille flow and all starting from the centreline can be equally spaced along the centreline; at the best of out knowledge, no experimental evidence of this phenomenon are at the moment available in literature. Finally it could be interesting to extend the results of the 'microrheometer' to other fluid typology and in a wider concentration range.

Bibliography

[1] R.P. Feynman, Eng Sci **23**(5), 22 (1960)

[2] P. Tabeling, *Introduction to microfluidics* (Oxford University Press, 2010)

[3] P.A. Auroux, D. Iossifidis, D.R. Reyes, A. Manz, Anal Chem **74**(12), 2637 (2002)

[4] D.R. Reyes, D. Iossifidis, P.A. Auroux, A. Manz, Anal Chem **74**(12), 2623 (2002)

[5] G.M. Whitesides, Nature **442**(7101), 368 (2006)

[6] N. Pamme, Lab Chip **7**(12), 1644 (2007)

[7] F.P. Bretherton, J Fluid Mech **14**(02), 284 (1962)

[8] B. Ho, L. Leal, J Fluid Mech **65**(02), 365 (1974)

[9] B. Ho, L. Leal, J Fluid Mech **76**(04), 783 (1976)

[10] A. Leshansky, A. Bransky, N. Korin, U. Dinnar, Phys Rev Lett **98**(23), 234501 (2007)

[11] G. D'Avino, G. Romeo, M.M. Villone, F. Greco, P.A. Netti, P.L. Maffettone, Lab Chip **12**(9), 1638 (2012)

[12] M. Villone, G. D'Avino, M. Hulsen, F. Greco, P. Maffettone, J Non-Newton Fluid **195**, 1 (2013)

[13] S. Yang, J.Y. Kim, S.J. Lee, S.S. Lee, J.M. Kim, Lab Chip **11**(2), 266 (2011)

[14] R.B. Bird, W.E. Stewart, E.N. Lightfoot, *Transport phenomena* (John Wiley & Sons, 1960)

[15] M.M. Denn, *Process fluid mechanics* (Prentice-Hall Englewood Cliffs, NJ:, 1980)

[16] G. Segré, A. Silberberg, Nature **189**(209-210) (1961)

[17] J. Matas, J. Morris, E. Guazzelli, Oil Gas Sci Technol **59**(1), 59 (2004)

[18] R.G. Larson, Constitutive equations for polymer melts and solutions (1988)

[19] C. Macosko, *Rheology: Principles, measurements, and applications. 1994*

[20] H. Lim, J. Nam, S. Shin, Microfluid Nanofluid pp. 1–10 (2014)

[21] D. Di Carlo, Lab Chip **9**(21), 3038 (2009)

[22] G.B. Lee, C.C. Chang, S.B. Huang, R.J. Yang, J Micromech Microeng **16**(5), 1024 (2006)

[23] M.G. Lee, S. Choi, J.K. Park, Lab Chip **9**(21), 3155 (2009)

[24] X. Xuan, J. Zhu, C. Church, Microfluid Nanofluid **9**(1), 1 (2010)

[25] H. Chu, I. Doh, Y.H. Cho, Lab Chip **9**(5), 686 (2009)

[26] Y.W. Kim, J.Y. Yoo, J Micromech Microeng **18**(6), 065015 (2008)

[27] R. Repetti, E. Leonard, Nature **203**, 1346 (1964)

[28] R.C. Jeffrey, J. Pearson, J Fluid Mech **22**(04), 721 (1965)

[29] J. Zhou, I. Papautsky, Lab Chip **13**(6), 1121 (2013)

[30] Y.S. Choi, K.W. Seo, S.J. Lee, Lab Chip **11**(3), 460 (2011)

[31] D.R. Gossett, D.D. Carlo, Anal Chem **81**(20), 8459 (2009)

[32] J.M. Martel, M. Toner, Scientific Reports **3** (2013)

[33] J.F. Edd, D. Di Carlo, K.J. Humphry, S. Köster, D. Irimia, D.A. Weitz, M. Toner, Lab Chip **8**(8), 1262 (2008)

[34] K.W. Seo, H.J. Byeon, H.K. Huh, S.J. Lee, RSC Advances **4**(7), 3512 (2014)

[35] K. Kang, S.S. Lee, K. Hyun, S.J. Lee, J.M. Kim, Nat Comm **4**(2567) (2013)

[36] C. Bustamante, Z. Bryant, S.B. Smith, Nature **421**(6921), 423 (2003)

[37] K.W. Seo, Y.J. Kang, S.J. Lee, Phys Fluids **26**(6), 063301 (2014)

[38] P. Sajeesh, A.K. Sen, Microfluid Nanofluid pp. 1–52 (2013)

[39] M. Yamada, M. Nakashima, M. Seki, Anal Chem **76**(18), 5465 (2004)

[40] J. Takagi, M. Yamada, M. Yasuda, M. Seki, Lab Chip **5**(7), 778 (2005)

[41] M. Yamada, M. Seki, Lab Chip **5**(11), 1233 (2005)

[42] M. Yamada, M. Seki, Anal Chem **78**(4), 1357 (2006)

[43] L.R. Huang, E.C. Cox, R.H. Austin, J.C. Sturm, Science **304**(5673), 987 (2004)

[44] J. McGrath, M. Jimenez, H. Bridle, Lab Chip **14**(21), 4139 (2014)

[45] L.R. Huang, J.O. Tegenfeldt, J.J. Kraeft, J.C. Sturm, R.H. Austin, E.C. Cox, Nat Biotechnol **20**(10), 1048 (2002)

[46] N. Pamme, Lab Chip **6**(1), 24 (2006)

[47] N. Pamme, C. Wilhelm, Lab Chip **6**(8), 974 (2006)

[48] N. Xia, T.P. Hunt, B.T. Mayers, E. Alsberg, G.M. Whitesides, R.M. Westervelt, D.E. Ingber, Biomed Microdevices **8**(4), 299 (2006)

[49] J. Kim, H.H. Lee, U. Steinfeld, H. Seidel, IEEE Sens. J. **9**(8), 908 (2009)

[50] L. Wu, Y. Zhang, M. Palaniapan, P. Roy, Biotechnol Bioeng **106**, 68 (2010)

[51] N. Pamme, A. Manz, Anal. Chem. **76**(24), 7250 (2004)

[52] D. Di Carlo, J.F. Edd, D. Irimia, R.G. Tompkins, M. Toner, Anal Chem **80**(6), 2204 (2008)

[53] S.S. Kuntaegowdanahalli, A.A.S. Bhagat, G. Kumar, I. Papautsky, Lab Chip **9**(20), 2973 (2009)

[54] J.M. Burke, R.E. Zubajlo, E. Smela, I.M. White, Biomicrofluidics **8**(2), 024105 (2014)

[55] J. Zhang, S. Yan, R. Sluyter, W. Li, G. Alici, N.T. Nguyen, Scientific Reports **4** (2014)

[56] J. Nam, H. Lim, D. Kim, H. Jung, S. Shin, Lab Chip **12**(7), 1347 (2012)

[57] S. Yang, S.S. Lee, S.W. Ahn, K. Kang, W. Shim, G. Lee, K. Hyun, J.M. Kim, Soft Matter **8**(18), 5011 (2012)

[58] S.W. Ahn, S.S. Lee, S.J. Lee, J.M. Kim, Chem Eng Sci (2014)

[59] G. D'Avino, Rheol Acta **52**(3), 221 (2013)

[60] L.G. Occhipinti, F. Porro, (2010). US Patent App. 12/835,011

[61] G. Romeo, G. D'Avino, F. Greco, P.A. Netti, P.L. Maffettone, Lab Chip **13**(14), 2802 (2013)

[62] G.M. Gibson, J. Leach, S. Keen, A.J. Wright, M.J. Padgett, Opt express **16**(19), 14561 (2008)

[63] T.G. Mason, D. Weitz, Phys Rev Lett **74**(7), 1250 (1995)

[64] M. Tassieri, R. Evans, R.L. Warren, N.J. Bailey, J.M. Cooper, New J Phys **14**(11), 115032 (2012)

[65] F. Del Giudice, A. Glidle, F. Greco, P.A. Netti, P.L. Maffettone, J.M. Cooper, M. Tassieri, arXiv preprint arXiv:1403.6629 (2014)

[66] K. Berg-Sørensen, H. Flyvbjerg, Rev Sci Instrum **75**(3), 594 (2004)

[67] N. Modak, A. Datta, R. Ganguly, Microfluid Nanofluid **6**, 647 (2009)

[68] K. Smistrup, O. Hansen, H. Bruus, M.F. Hansen, J Magn Mater **293**, 597 (2005)

[69] F. Gauthier, H.L. Goldsmith, S.G. Mason, Trans Soc Rheol (1957-1977) **15**(2), 297 (1971)

[70] J.P. Brody, P. Yager, R.E. Goldstein, R.H. Austin, Biophys J **71**, 3430 (1996)

[71] N. Ichikawa, K. Hosokawa, R. Maeda, J Colloid Interface Sci **280**, 155 (2004)

[72] G. D'Avino, T. Tuccillo, P.L. Maffettone, F. Greco, M. Hulsen, Comput Fluids **39**(4), 709 (2010)

[73] R.B. Bird, R.C. Armstrong, O. Hassager, *Dynamics of polymeric liquids: Fluid Mechanics* (Wiley-Interscience, New York, 1987)

[74] R.B. Bird, P.J. Carreau, Chem Eng Sci **23**(5), 427 (1968)

[75] J. Higdon, G. Muldowney, J Fluid Mech **298**, 193 (1995)

[76] K. Devanand, J. Selser, Nature **343**(6260), 739 (1990)

[77] P. Molyneux, *Water-soluble synthetic polymers: properties and behavior* (CRC Press. Inc., 1983)

[78] K.W. Ebagninin, A. Benchabane, K. Bekkour, J Colloid Interf Sci **336**(1), 360 (2009)

[79] R.G. Larson, *The structure and rheology of complex fluids*, vol. 4 (Oxford university press New York, 1999)

[80] R.H. Colby, Rheol Acta **49**(5), 425 (2010)

[81] M. Rubinstein, R. Colby, *Polymers Physics* (Oxford, 2003)

[82] V. Tirtaatmadja, G.H. McKinley, J.J. Cooper-White, Phys Fluids **18**(4), 043101 (2006)

[83] M. Doi, S. Edwards, *The theory of polymer dynamics.* 73 (Oxford University press, 1988)

[84] E. Immergut, W. McDowell, *Polymer handbook* (Wiley, 1975)

[85] J. Cooper-White, J. Fagan, V. Tirtaatmadja, D. Lester, D. Boger, J Non-Newton Fluid **106**(1), 29 (2002)

[86] J. Ferguson, N. Hudson, B. Warren, J Non-Newton Fluid **44**, 37 (1992)

[87] J. Rosiak, K. Burozak, W. Pękala, Radiat Phys Chem **22**(3), 907 (1983)

[88] R.A. Zangmeister, M.J. Tarlov, Langmuir **19**(17), 6901 (2003)

[89] F. Durst, R. Haas, B. Kaczmar, J Appl Polym Sci **26**(9), 3125 (1981)

[90] M. Tassieri, T. Waigh, J. Trinick, A. Aggeli, R. Evans, J Rheol **54**(1), 117 (2010)

[91] A. Pommella, V. Preziosi, S. Caserta, J.M. Cooper, S. Guido, M. Tassieri, Langmuir **29**(29), 9224 (2013)

[92] N. Sastry, P. Dave, M. Valand, Eur Polym J **35**(3), 517 (1999)

[93] C. Bruce, W. Schwarz, J Polym Sci Part A-2: Polym Phys **7**(5), 909 (1969)

[94] P. Munk, T.M. Aminabhavi, P. Williams, D.E. Hoffman, M. Chmelir, Macromolecules **13**(4), 871 (1980)

[95] A. O'Sullivan, Cellulose **4**(3), 173 (1997)

[96] S. Naik, J. Pittman, J. Richardson, Trans Soc Rheol (1957-1977) **20**(4), 639 (1976)

[97] W. Wetzel, M. Chen, J. Glass, **248**, 163 (1996)

[98] A.H. Drelich. Fibrous structures and methods of making the same (1963). US Patent 3,087,833

[99] A. Chanachai, R. Jiraratananon, D. Uttapap, G. Moon, W. Anderson, R. Huang, J Membrane Sci **166**(2), 271 (2000)

[100] L. Hammarström, L. Heijl, S. Gestrelius, J Clin Periodontol **24**(9 Pt 2), 669 (1997)

[101] R. Anders, H.P. Merkle, Int J Pharm **49**(3), 231 (1989)

[102] T. Miyamoto, S.i. Takahashi, H. Ito, H. Inagaki, Y. Noishiki, J Biomed Mater Res **23**(1), 125 (1989)

[103] J. Meadows, P. Williams, J. Kennedy, Macromolecules **28**(8), 2683 (1995)

[104] A. Maestro, C. Gonzalez, J. Gutierrez, J Rheol **46**, 1445 (2002)

[105] T. Saito, S. Kimura, Y. Nishiyama, A. Isogai, Biomacromolecules **8**(8), 2485 (2007)

[106] D. Ishii, T. Saito, A. Isogai, Biomacromolecules **12**(3), 548 (2011)

[107] N. Arfin, H. Bohidar, Int J Biol Macromol **50**(3), 759 (2012)

[108] W. Cox, E. Merz, J Polym Sci **28**(118), 619 (1958)

[109] V. Shankar, M. Pasquali, D.C. Morse, J Rheol **46**, 1111 (2002)

[110] M. Doi, S. Edwards, J Chem Soc, Faraday Trans 2 **74**, 560 (1978)

[111] M. Doi, S.F. Edwards, J Chem Soc, Faraday Trans 2 **74**, 918 (1978)

[112] J.D. Ferry, *Viscoelastic properties of polymers*, vol. 3 (Wiley New York, 1980)

[113] H. Hoffmann, U. Kästner, R. Dönges, R. Ehrler, Polym Gels Netw **4**(5), 509 (1996)

[114] U. Kästner, H. Hoffmann, R. Dönges, R. Ehrler, Colloid Surface A **82**(3), 279 (1994)

[115] V. Shankar, M. Pasquali, D. Morse, J Rheol **46**(5), 1111 (2002). DOI 10.1122/1.1501927

[116] D. Morse, Macromolecules **31**(20), 7030 (1998). DOI 10.1021/ma9803032

[117] D. Morse, Macromolecules **31**(20), 7044 (1998). DOI 10.1021/ma980304u

[118] D. Morse, Macromolecules **32**(18), 5934 (1999). DOI 10.1021/ma970475j

[119] G. d'Avino, P.L. Maffettone, F. Greco, M. Hulsen, J Non-Newton Fluid **165**(9), 466 (2010)

[120] G. D'Avino, P. Maffettone, J Non-Newton Fluid (2014)

[121] D. Won, C. Kim, J Non-Newton Fluid **117**(2), 141 (2004)

[122] M.A. Alves, P.J. Oliveira, F.T. Pinho, J Non-Newton Fluid **110**(1), 45 (2003)

[123] J.Y. Kim, S.W. Ahn, S.S. Lee, J.M. Kim, Lab Chip **12**(16), 2807 (2012)

[124] K. Ishii, H. Hasimoto, J Phys Soc Japan **48**, 2144 (1980)

[125] E.J. Lim, T.J. Ober, J.F. Edd, S.P. Desai, D. Neal, K.W. Bong, P.S. Doyle, G.H. McKinley, M. Toner, Nat Comm **5**(4120) (2014)

[126] M. Trofa, M. Vocciante, G. D'Avino, M.A. Hulsen, F. Greco, P.L. Maffettone, Comput Fluids (2014)

[127] J. Zilz, C. Schäfer, C. Wagner, R.J. Poole, M.A. Alves, A. Lindner, Lab Chip **14**(2), 351 (2014)

[128] A. Lindner, J. Vermant, D. Bonn, Physica A **319**, 125 (2003)

[129] A. Zell, S. Gier, S. Rafai, C. Wagner, J Non-Newton Fluid **165**(19), 1265 (2010)

[130] J. Meissner, J. Hostettler, Rheol Acta **33**(1), 1 (1994)

[131] J.A. Pathak, S.D. Hudson, Macromolecules **39**(25), 8782 (2006)

[132] C.J. Pipe, G.H. McKinley, Mech Res Comm **36**(1), 110 (2009)

[133] N.T. Nguyen, Y.F. Yap, A. Sumargo, Meas Sci Technol **19**(8), 085405 (2008)

[134] A. Groisman, V. Steinberg, Nature **410**(6831), 905 (2001)

[135] H. Stone, J Fluid Mech **409**, 165 (2000)

[136] C.E. Brennen, *Fundamentals of multiphase flow* (Cambridge University Press, 2005)

[137] M. Hejazian, W. Li, N.T. Nguyen, Lab Chip p. Accepted Manuscript (2015)

[138] G. D'Avino, M. Hulsen, P. Maffettone, Comput Fluids **86**, 45 (2013)